



3D Plasma-sheath-lenses phenomenology and applications

Stamate, Eugen

Publication date:
2024

Document Version
Publisher's PDF, also known as Version of record

[Link back to DTU Orbit](#)

Citation (APA):
Stamate, E. (2024). *3D Plasma-sheath-lenses: phenomenology and applications*. DTU Nanotech.

General rights

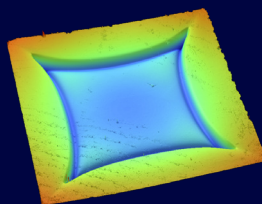
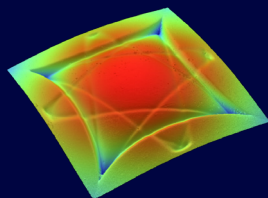
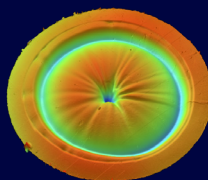
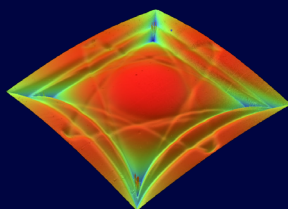
Copyright and moral rights for the publications made accessible in the public portal are retained by the authors and/or other copyright owners and it is a condition of accessing publications that users recognise and abide by the legal requirements associated with these rights.

- Users may download and print one copy of any publication from the public portal for the purpose of private study or research.
- You may not further distribute the material or use it for any profit-making activity or commercial gain
- You may freely distribute the URL identifying the publication in the public portal

If you believe that this document breaches copyright please contact us providing details, and we will remove access to the work immediately and investigate your claim.

3D Plasma-sheath-lenses: phenomenology and applications

Doctor Techniques dissertation by
Eugen Stamate



3D Plasma-sheath-lenses: phenomenology and applications

**Doctor Technices dissertation by
Eugen Stamate**

Cover image:

Modal and discrete ion focusing patterns on square and disk electrodes developed by etching on silicon in Ar/SF₆ plasma

Published by DTU,

National Centre for Nano Fabrication and Characterization

Ørsted's Plads – Building 347, DK-2800 Kongens Lyngby, Denmark

Printed 2024

ISBN 978-87-975214-0-3 (Printed version)

ISBN 978-87-975214-0-3 (Electronic version)



Denne afhandling er af Danmarks Tekniske Universitet antaget til forsvar for den tekniske doktorgrad. Antagelsen er sket efter bedømmelse af den foreliggende afhandling.

Kgs. Lyngby, den 7. februar 2024

A blue ink signature of Anders O. Bjarklev.

Anders O. Bjarklev
Rektor

A blue ink signature of Rasmus Larsen.

Rasmus Larsen
Prorektor

This thesis has been accepted by the Technical University of Denmark for public defence in fulfilment of the requirements for the degree of Doctor Technices. The acceptance is based on an evaluation of the present dissertation.

Kgs. Lyngby, 7 February 2024

A blue ink signature of Anders O. Bjarklev.

Anders O. Bjarklev
President

A blue ink signature of Rasmus Larsen.

Rasmus Larsen
Provost

Eugen Stamate doktordisputats, Titel: 3D Plasma-sheath-lenses:
phenomenology and applications

Forsvaret finder sted kl. 14.00, 04/04/2024 i lokale auditorium 1, Anker
Engelunds Vej 101, Danmarks Tekniske Universitet, 2800 Kongens Lyngby

The defence will take place at 14:00 on 4th of April 2024 at auditorium 1,
building 101, Anker Engelunds Vej 101, Technical University of Denmark,
2800 Kongens Lyngby

Preface

This dissertation is submitted for partial fulfillment of the requirements to obtain the Doctor Technicus degree from the Technical University of Denmark (DTU). The dissertation is following my scientific journey in discovering the modal and discrete ion focusing effects, introducing the pioneering concept of 3D plasma-sheath-lenses, developing several applications, and extending the concept to other relevant situations. It started with an intriguing observation of an extensively used planar probe surface and it took a few years to be able to explain by experiments and simulations that ion kinetics within a 3D potential distribution is exceedingly complex. The content of the dissertation, including most figures, is based on 17 journal papers, one granted patent (US) and one patent application (listed herein as ES1 to ES19) that have been authored and coauthored during my last two years at Nagoya University, Japan and eventually at Technical University of Denmark.

The scientific journey was affected by my relocation from Nagoya University, Japan, to DTU Risø Campus, Denmark, (in 2006) and then from DTU Risø Campus to DTU Lyngby Campus (in 2019).

I am pleased and deeply grateful to the management (Director Jörg Hübner, Deputy Director Anders Michael Jørgensen, Prof. Rafael Taboryski and Assoc. Prof. Flemming Jensen) and the staff at DTU Nanolab for providing the opportunity to materialize the research subject in this dissertation and for the support in transitioning to a new and exciting research project, Smart3D, funded by Innovation Fund Denmark (2081-00011B).

I am indebted to Prof. Hideo Sugai, from Nagoya University, for hosting and kindly supporting my initial research on this topic. I would also like to acknowledge the privilege of an enlightening scientific network on plasma physics connected to the “Plasma-Nano” Centre of Excellence led by Prof. Sugai, including Prof. H. Toyoda, Prof. K. Sasaki, Prof. M. Aramaki, Prof. T. Ishijima, Prof. A. Kono and Prof. M. Hori. Special thanks and appreciation to Prof. O. Takai for his support with my first attempts on surface characterization. It was a great pleasure working closely with Dr. S. Nakao and Dr. N. Holtzer, PhD students at that time. The loss of Assoc. Prof. M.

Yamaguchi who kindly supported this research during my stay as visiting professor at Venture Business Laboratory, Nagoya University in 2009, brought sadness and frustration.

I am also indebted to my former colleagues at DTU Risø campus who kindly supported my enthusiasm during the building up, from empty rooms, of the Plasma Processing Laboratory: Director Henrik Bindslev, Prof. Jens-Juul Rasmussen, Dr. Poul Mikkelsen, Dr. Søren Korsløm, Dr. Anders Nielsen, and Prof. Volker Naulin. Special thanks go to Dr. Mihai Draghici for his dedicated collaboration during the postdoctoral stay in plasma lab, research that resulted in the journal publications covering electronegative discharges. In 2012, I joined the newly formed Department of Energy Conversion and Storage (DTU Energy) where I had the chance to collaborate in my first Grand Solutions project with Dr. Kion Norrman and Prof. Poul Norby. I am also grateful to Prof. Peter Holtappels, Prof. Nini Pryds and Professor and Head of Department Søren Linderøth for their kind support during my affiliation at DTU Energy.

I would also like to acknowledge the contributions of Mihai-Andrei Petrea (Erasmus+) and Shadab Khan (master student) for their dedicated measurements that were included in two publications.

The research included in this dissertation was supported by Plasma-Nano Center of Excellence at Nagoya University, Japan, Marie Skłodowska Curie International Reintegration Grant, Start-up grant at Risø National Laboratory, GAP founding, DTU Discovery grant and Innovation Fund Denmark (SmartCoating, 6151-00011B). In this context, special thanks go to industrial collaborators Polyteknik A/S and Velux A/S for their participation in the SmartCoating project.

For their insightful and kind early-career guidance I am indebted to Prof. Gheorghe Popa from “Al. I. Cuza” University, Iasi, Romania and Prof. Kazuyuki Ohe, Nagoya Institute of Technology, Japan.

I am also grateful to the scientific community for the *Plasma Physics Innovation Prize* awarded in 2012 by the European Physical Society for the discovery of modal and discrete ion focusing effects.

I dedicate this dissertation to my parents Anisia and Neculai, my wife Yue, and my daughters Elisa and Amelia.

DTU, February 2024

Eugen Stamate

Dansk resumé

Plasmaer har et stort potentiale for forskellige behandlinger, eksempelvis af overflader idet de kan danne og indeholde en lang række af aktive komponenter (ioner, radikaler, klynger, nukleater m.fl.). Dette gør dem udbredte i mikro- og nanoelektronikindustrien til ætsning, forstøvning, aflejring, oxidation, passivering eller implantation, samt til at tilpasse de optiske, elektriske, magnetiske eller biologiske egenskaber af forskellige materialer. Derudover anvendes de ved syntese af komplekse nanosamlinger og nanostrukturer såsom nanorør, nanovægge eller nanodots. De fleste af disse processer er baseret på radikal-assisterede, ion-inducerede overflademodifikationer, hvor positive eller negative ladninger akkumulerer energi i det såkaldte "plasma-sheath" – overgangslaget mellem det homogene plasma og overfladen – og derefter rammer overfladen med en given energi og indfaldsvinkel. For at indstille og kontrollere egenskaberne af materialer, grænseflader, film og strukturer skal man være i stand til detaljeret at kontrollere et særdeles komplekst system dannet af plasma-presheath-sheath og den tilstødende overflade, nemlig plasma-presheath-sheath-overfladesystemet.

På trods af de betydelige fremskridt er vi endnu ikke i stand til nøjagtigt at beregne og dermed eksperimentelt bekræfte 3D-banen for en positiv ion fra plasma, der ender med at blive opsamlet af en negativt forspændt elektrode med en kvadratisk udstrækning. Dette bliver endnu mere kompliceret: i) for en elektrode med kompleks form, ii) for et plasma, der omfatter flere ionarter, negative ioner, og ladet støv, (iii) i nærværelse af et magnetfelt, iv) for en tidsafhængig bias og v) ved at inkludere overfladeprocesser.

I denne afhandling undersøges ladnings-fluxfordelingen på overfladen af forspændte elektroder med forskellige geometrier indsat i et plasma ved numeriske simuleringer og laboratorieeksperimenter. Det bliver demonstreret, at plasma-sheath'et, der omgiver elektroder, der grænser op til isolatorer, fungerer som en elektrostatiske linse, der styrer ladningerne til forskellige steder på elektrodeoverfladen afhængigt af indgangs-koordinaterne ved sheath-kanten. Det vil sige, at to fokuseringseffekter er identificeret. Den diskrete fokusering fører til dannelsen af en passiv

overflade uden ionpåvirkning nær kanten af elektroderne, der grænser op til isolatorer. Denne modale fokusering resulterer i dannelsen af visse "modale spots" og/eller "modale linjer".

De veldefinerede mønstre, som er resultatet af disse fokuseringseffekter, åbner nye muligheder inden for plasma- og sheath-diagnostik i direkte sammenhæng med ion-inducerede overflademodifikationer. Ved at tilpasse forskellige plasma-sheath-linsestrukturer er det muligt at eksperimentere med ionkinetik for at inducere en ønsket ionoptik. I kombination med et magnetfelt giver dette en stor fleksibilitet til forskellige applikationer, herunder fokuseret ionstråleekstraktion, massespektrometri, plasma-immersionsionimplantation og nye sensorer for negative ioner eller plasmametre. Der forventes nye udviklinger for en endnu bedre sammenhæng mellem simulering og eksperimenter, herunder tidsafhængige processer eller andre detaljer.

Det banebrydende koncept med 3D-plasma-sheath-linser udvides derefter yderligere ved at undersøge oxygenegative ioner, der fokuserer i kappen og aflejres på måloverfladen under tyndfilmaflejring ved magnetron-forstøvning. Det påvises, at de fokuserede ioner inducerer præferentiel Zn-forstøvning under væksten af aluminiumdoteret zinkoxid, en gennemsigtig ledende oxid med brede anvendelser i solceller, skærme og intelligente vinduer. Der foreslås en metode til at reducere deres skadelige rolle, herunder en afstemningselektrode.

Contents

1.	Introduction	-1-
1.1	Motivation and hypothesis	-3-
1.2	One dimensional plasma sheath	-3-
1.3	Multi ion species plasma sheath	-4-
1.4	Electronegative plasmas	-5-
1.5	Magnetized plasma sheath	-6-
1.6	Plasma sheath diagnostics	-7-
1.7	Plasma aided nanofabrication	-7-
2.	Three-dimensional plasma-sheath-lenses	-8-
2.1	Modal and discrete ion focusing effects.....	-9-
2.2	Negative ion focusing	-23-
2.3	Ion focusing by 3D magnetized plasma-sheath-lenses	-29-
3.	Applications of 3D plasma-sheath-lenses	-31-
3.1	Plasma immersion ion implantation	-31-
3.2	Plasma diagnostics	-36-
3.3	Ion beam extraction	-39-
3.4	Mass separation	-46-
4.	Negative ion focusing during magnetron sputtering	-49-
4.1	Metal oxide thin film growth assisted by energetic negative ions	-50-
4.2	Reducing the oxygen negative ion energy in RF discharges by controlling the dc self-bias	-57-
4.3	Preferential sputtering by 3D focused negative ions .	-60-
5.	Conclusion and outlook	-67-
5.1	Conclusion	-67-
5.2	Outlook	-69-
6.	Included publications	-71-
ES1	-71-
ES2	-72-
ES3	-73-

ES4	-74-
ES5	-75-
ES6	-76-
ES7	-77-
ES8	-78-
ES9	-79-
ES10	-80-
ES11	-81-
ES12	-82-
ES13	-83-
ES14	-84-
ES15	-85-
ES16	-86-
ES17	-87-
ES18	-88-
Es19	-89-
References	-90-

1. Introduction

Plasma-based processes such as dry etching, thin film deposition by physical or chemical vapor methods, and ion implantation have contributed tremendously to the progress of micro- and nanoelectronics device technologies over the last 40 years.¹⁻⁵ For example, the revolutionary transition from room-size computers to pocket-size smart phones would not have been possible without replacing wet isotropic etching with directional, ion-induced, and radical-assisted plasma (dry) etching.^{6,7} Consequently, the half-pitch of a memory cell (node) decreased from 10 μm in 1971 to 5 nm in 2020.⁸ However, in spite of these achievements, supported by an intense research activity, we are not yet able to accurately calculate the 3D trajectory of an ion originating from plasma that ends up collected by a biased electrode/substrate (e.g., silicon wafer). This is even more complicated: i) for an electrode of complex shape; ii) for a plasma including multi-species positive ions, negative ions or charged dust; (iii) in the presence of magnetic field; iv) for a time-dependent bias; and v) by including surface processes at the biased electrode. This limits the possibility to move from 1D and 2D to 3D micro and nano device architectures and prevents the ability to produce and manipulate ions relevant for development of 3D devices based on tailored advanced functional materials and interfaces.

The basic principle of plasma processing (for example silicon etch in Ar/SF_6 plasma)⁹ is based on a plasma source (able to create ions, electrons, reactive species, photons) where a biased electrode/substrate is exposed to plasma (see Figure 1 (a)). The negative bias reflects the negative charges (electrons and negative ions if present) and accelerates the positive ions. The positive space charge layer formed between plasma and the substrate is named sheath¹⁰ and it should be parallel to the surface to be treated (for 1D and 2D processing) for ensuring an ion-induced, radical-assisted process of high uniformity. The sheath evolves as an interface between plasma (through a pre-sheath) and the exposed substrate.¹¹⁻¹⁵ This is a common scenario not only for etching but also for other major plasma-assisted surface processes.¹⁶⁻¹⁸ A large number of devices and sensors are now moving towards 3D architectures (nanoelectronics,¹⁹⁻²¹ MEMS,²² 3D microbatteries,²³ 3D solar

cells,²⁴ Internet of Things²⁵) that require conformal processing. However, we currently have only qualitative understanding of the 3D plasma-presheath-sheath-structure even for a DC biased substrate in a single positive ion – electron plasma as presented in Fig 1 (b).

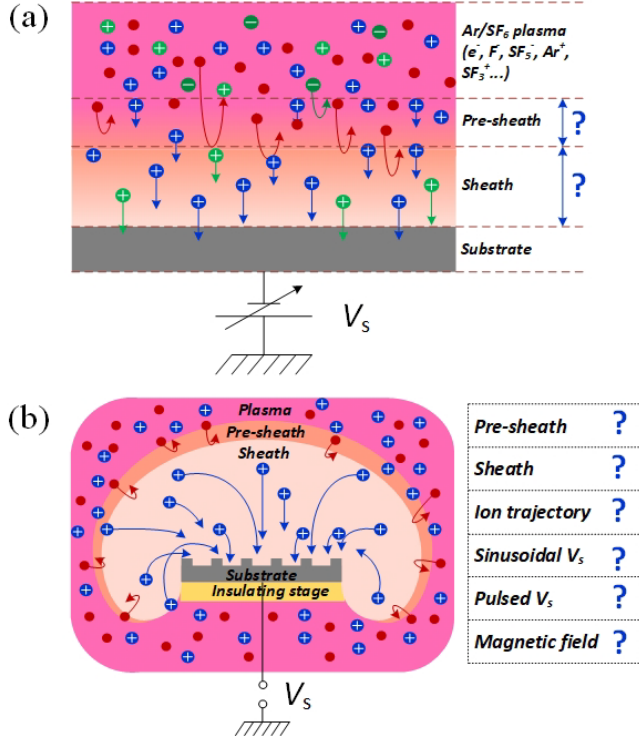


Fig. 1 Schematic visualization of plasma, pre-sheath, sheath, and substrate for: (a) 1D/2D Ar/SF₆ plasma including several species of positive and negative ions for a DC biased substrate; (b) single-ion electron plasma for a 3D biased-substrate (gray) placed on an insulated stage (yellow).

1.1 Motivation and hypothesis

The overall motivation of this dissertation is to understand the ion kinetics in 3D potential structures (space-charges or sheaths) evolving to complex electrodes immersed into plasma, with a twofold aim:

- answer fundamental questions of plasma physics, including sheath formation and its boundary, charge dynamics with and without magnetic fields and ion induced surface processes.
- increase our ability towards nanofabrication technology by gaining more understanding related to plasma-based, ion-induced processes such as sputtering, etching, ion implantation and ion beam extraction.

The hypothesis is that the scientific and technological development of plasma physics reached the need of addressing the 3D aspects of plasma-presheath-sheath-surface system. This requires the ability to predict with high accuracy the trajectory of a charge collected from neutral plasma until reaching a biased surface. The claim of this dissertation is that charge focusing within such 3D structures can provide valuable routes of investigation based on the very well defined and easily measurable patterns exhibited at the electrode surface via charge impacts.

1.2 One dimensional plasma sheath

Despite advanced diagnostics and characterization techniques available for plasmas and surfaces, the presheath–sheath structure remains one of the least understood aspects in plasma physics.^{10–15} For instance, there are no mathematical models able to describe the whole plasma–presheath-sheath system, even in one dimension, and there is no general agreement regarding the role, size, and location of the presheath, as the intermediate layer between the plasma and the sheath. The first difficulty comes from the complexity of reactive plasmas consisting of various charged and neutral species with unknown cross-sections and yields that need to be included in mathematical formulation. The second major difficulty is the lack of appropriate diagnostic methods able to measure low electric fields over distances usually below a few mm.^{26–28} Finally, one should also add the three-

dimensional (3D) structure of the sheath, molding on surfaces of various geometries, in a stationary or time dependent process.^{29–33} All these aspects result in the challenging task of being able to predict the ion flux density, ion energy and the impinging species on a substrate. As a result, most theoretical models reported so far neglect the higher dimensional aspects of the sheath by mainly considering infinite substrates while experimentalists try to avoid or limit the contribution of what is generically named the 'edge effect'.³³ For instance, in most recent one-dimensional (1D) treatments, the sheath exhibits an asymptotic potential distribution derived from sheath equations, which needs to be patched to a plasma solution through a presheath that can be as large as the entire plasma volume [16–18].^{13–15} Moreover, in the 1D approach the kinetics of the charged particles exhibit simple trajectories perpendicular to the surface, making it obviously easier to link the ion flux with potential surface modifications. Expecting that a finite substrate will only complicate the modelling by forcing the ion flux to a non-uniform distribution over the surface, it is clearly a demanding task to make advancements in this direction.

1.3 Multi ion species plasma sheath

Processing plasmas are produced by complex gas mixtures, so that more than one ion species (positive or negative) is passing through the sheath. This aspect raised the fundamental question: does each ion species attain its own Bohm velocity or do all ions enter the sheath with a similar velocity.^{34–37} A significant experimental effort was devoted to investigating the ion velocity distribution function, at the sheath front, by different methods, including emissive probes and 1D laser induced fluorescence (LIF).^{34,38–42} Numerical models have also been proposed, supporting both approaches.³⁷ For a sheath front parallel with the electrode surface, having the ions arriving at the surface (under normal incidence) with slightly different velocities is not a big issue. However, at oblique incidence (3D sheath), the electrostatic potential structure within the sheath is a kinetic energy analyzer, which means that ions gaining or losing energy in the presheath (by some collective interaction), will have different trajectories and consequently different impact locations. Experimental results, reported by LIF in Ar and He gas-mixture plasma,

concluded that Ar ions were traveling more than 75% faster than their individual Bohm speed.³⁴ However, this result needs to be confirmed by alternative methods and for other ions than Ar.

1.4 Electronegative plasmas

Most gases used for plasma etching (CF_4 , SF_6 , Cl_2) are electronegative, so that not only electrons but also negative ions are present.^{43–50} O_2 is also electronegative and is widely used to produce oxide thin films by sputtering, for photoresist ashing and to passivate the sidewalls during etching.^{6,7} Electron attachment mainly involves low-energy electrons that end replaced with heavy negative ions. The density ratio of negative ions to electrons is below 20 in O_2 plasma^{51–56} but can reach over 300 in Ar/ SF_6 .^{57,58} This drastic change in mobility affects plasma-presheath-sheath properties in a not yet understood way. Ion bombardment induces secondary electron emission that also influences the sheath structure. For example, during high-aspect-ratio trench etching, positive ions can accumulate at the trench bottom, building up a positive space charge that can deflect the incoming ions, eventually bowing the trench.^{6,7,59–62} Charge accumulation can also induce local electric fields that can produce damage during fabrication of memory devices. The secondary electron emission leaves the surface positive, so that the process needs to be pulsed-operated, allowing electrons from plasma to penetrate the trench and cancel the accumulated positive charge. Etching by negative ions will also generate secondary electrons but the negative ion charge accumulation is reduced by the positive surface.

This mechanism motivated extensive research on negative ion sources as a possible alternative for an etching process free of charge accumulation.^{62–70} Moreover, the negative ions can be neutralized, resulting in a completely charge-free etching process by neutral beam.^{71–74} It is expected that beams of negative ions or neutrals can be used in surface and interface science, and micro and nano-device fabrication [83]. Negative and neutral beams are also relevant for space thrusters where one needs to avoid the positive space charge built up by positive ions.^{75–79}

Of fundamental importance is to understand the basic properties of electronegative discharges.^{80–88} While a negative bias with respect to plasma potential generates a positive space charge of certain thickness it is also important to know if a positive bias can be sustained in an electronegative discharge without elevating the plasma potential or igniting a positive glow. If this is possible, then one could be able to produce a negative space charge that will accelerate the negative ions towards the biased electrode producing surface effects depending on ions energy and plasma properties.

1.5 Magnetized plasma sheath

Static or dynamic magnetic fields are often used to additionally control plasma properties by providing: confinement in a certain volume,^{89,90} resonance mechanisms for heating plasma electrons,⁹¹ reduced loss at chamber's walls,^{92,93} lower electron temperature,^{58,94} charge deflection⁹⁵ or local enhancement of plasma density.⁹⁶ Due to the large difference in mass between electrons and ions the magnetic-field-effect will depend on the aspect ratio between the gyration radiuses and other characteristic dimensions of the plasma source. Coupled with the magnetic field directionality, the charge kinetics ends up strongly anisotropic, requiring 3D techniques for simulations and experiments. This complexity affects the plasma-presheath-sheath system as well, including the sheath expansion, its shape and the Bohm criteria.^{97–100} While various theoretical investigations have been reported, including magnetized sheath in presence of negative ions,¹⁰¹ dust,^{102,103} multi-ion species,^{104–106} collisions,^{107,108} two-temperature electrons,^{109,110} for different magnetic field orientations with respect to the based electrode surface (perpendicular, tilted^{111,112}, parallel¹¹³), the experimental coverage is very limited due to the lack of appropriate diagnostics methods. Moreover, considering 2D or 3D electrodes or time dependence, further complicates both numerical investigations and experiments.¹¹⁴ Magnetized plasmas are intensively used for nanofabrication (see for example thin film deposition by magnetron sputtering) and for the synthesis of various functional materials (growth of nanotubes, nano-walls, etc) where the plasma-presheath-sheath system needs to be coupled with surface properties. This expected development motivates the need to know,

at quantitative level, the magnetic field effect on 2D and 3D biased electrodes.

1.6 Plasma sheath diagnostics

The main parameters for a 1D sheath are its thickness, h_s , and the potential distribution $V(z)$, where z is a coordinate perpendicular to the biased electrode, and Σ the sheath front or boundary. Plasma sources used for etching or thin film deposition have densities ranging from 10^{15} up to 10^{18} m^{-3} with negative biases reaching a few hundred volts. For such conditions, the sheath thickness is typically below 1 cm. Ion implantation requires energies above 500 eV leading to thicker sheaths when implantation is performed by plasma immersion.^{5,115} The sheath front can be detected by measuring the electric field with 2D laser induced fluorescence (LIF) dip spectroscopy,^{34,40,41,116–118} emissive probes^{38,39} or electrostatic probes.¹¹⁹ Since probes are invasive (size comparable with that of the aimed structures to be measured), their use raises high concern for reliability. Laser induced fluorescence diagnostics and other laser assisted diagnostics methods are now able to measure electric fields, and ion velocity distribution function in 2D structures with good spatial distribution (a few volts per cm).^{42,120–124} Time dependent LIF,^{125,126} oblique incidence measurements⁴² and the possibility to extract the electric field from ion velocity have been reported.^{116,117} Such measurements have been applied to metal-dielectric interfaces,¹²¹ biased probes,¹²⁰ sheath boundary in multi-ion species plasmas,³⁴ helicon discharges,⁴⁰ inductively coupled discharges,¹¹⁸ RF biased electrodes,¹²⁷ magnetron plasma sputtering¹²⁸ and ion thrusters,¹²⁴ just to mention low pressure applications. However, the main impediment of LIF remains the very limited gases that can be investigated and the poor applicability for 2D and 3D structures.

1.7 Plasma aided nanofabrication

Processing plasmas can generate an entire range of active species (ions, radicals, clusters, nucleates, etc) that make them widely used in the micro- and nanoelectronics industry for etching,^{6,7,65,129–132} sputtering, deposition,^{3,133–135} oxidation,^{136–138} passivation,^{139–141} or implantation,^{5,32,142} and in tailoring optical, electrical, catalytic, magnetic or biological properties of

various materials.^{143,144,153–155,145–152} Additionally, synthesis of complex nano assemblies and nanostructures such as nanotubes, nanowalls or nanodots is also realized assisted by reactive plasmas.^{156–162} Most of these processes are based on radical-assisted, ion-induced surface modifications where positive or negative charges accumulate energy within the plasma sheath then strike the surface with a certain energy and incidence angle. For tuning the properties of materials, interfaces, films, and structures one should be able to control in detail a very complex system formed by the plasma-presheath-sheath and the adjacent surface, namely the plasma-presheath-sheath-surface system. Silicon nanoelectronics technology is reaching its limits (transistors smaller than 7 nm will be affected by quantum tunnelling).^{6,7} However, the enormous development in this field could contribute with high impact to research areas where very dedicated functional materials, devices and interfaces are needed for energy conversion and storage,^{163,164} biomedical applications^{165,166} and sensors.^{167,168}

The tremendous effort on nanotechnology emphasizes the importance of being able to build small devices by having the capability to bring certain functional ions, clusters, radicals in the proximity of a complex structure embedded on a chip, most times below 1 cm^2 .^{169–171} Reactive ions (oxygen, nitrogen, sulphites, etc) of energies from a few eV up to hundreds eV are expected to play an essential role in the development of functional materials and interfaces.¹⁷² Energy devices have a stringent need for advanced functional materials.^{173,174} Small sensors and micro-batteries require 3D architecture to deliver the expected functionality or increase the power density.^{175,176} While in 2D manufacturing the ions are accelerated perpendicular towards the substrate, 3D architectures need ion deflection to be able to perform conformal processing (thin film deposition, surface passivation or oxidation). This emphasizes the need to be able to predict and control the ion kinetics in 3D potential structures.

2. Three-dimensional plasma-sheath-lenses

The first evidence of very well-defined patterns by ion focusing is a 3D sheath structure was revealed by the author when using planar Langmuir probes to measure the electron energy distribution function (EEDF) in reactive gases such as SF_6 and O_2 .^{177,178} At that time, the standard procedure was to clean

the probe surface using ion bombardment by having the probe at a significant negative bias with respect to plasma potential, a situation that generates a 3D, positive ion sheath. It was then stated that: “... *the elliptic-like sheath profile of a planar probe behaved as an electrostatic lens that focused the charged particles on distinct regions of the probe surface; an active one at the center, and a passive one at the edge*”.¹⁷⁷ Due to the difference in work function, it was also demonstrated that probe characteristics measured in such conditions will exhibit a double-hump structure. Since similar structures were associated with negative ions (under similar probe cleaning procedure) that finding was a direct questioning of negative ions detection by Langmuir probes. The only way to check the assumption of positive ion focusing was to perform 3D simulations for detecting the sheath structure and then to calculate the ion trajectories for revealing the impact locations. This endeavor started in 2003 and this chapter will present the main results describing the discovery of modal and discrete focusing effects associated with the pioneering concept of 3D plasma sheath lenses.

2.1 Modal and discrete ion focusing effects

ES1 and ES2 are the main publications introducing the focusing effects (supporting the need for separate nomination), and the definitions of passive surface, active surface, impact radius and modal lines. Additional results were included in ES3, that also reviews the main concepts, and ES4.

Let us consider a square electrode of 0.01 m in length, L , and insulated on the rear-side that is placed into a plasma of density, $n_0 = 10^{15} \text{ m}^{-3}$, electron temperature, $T_e = 2 \text{ eV}$, ion temperature $T_i = 0.2 \text{ eV}$ and biased at $V_0 = -300 \text{ V}$ with respect to plasma potential, V_{pl} , set at 0 V. Calculating self-consistently the 3D potential distribution in the plasma-presheath-sheath system is not yet mathematically possible and for this reason one can estimate the potential distribution in the sheath by solving Poisson's equation by finite element method, assuming Maxwellian distributions for electrons:

$$\nabla^2 V(x, y, z) = -\frac{e}{\epsilon_0} [n_i^*(V) - n_e^*(V)] , \quad \text{Eq. (2.1)}$$

where $n_i^*(V)$ and $n_e^*(V)$ are the positive ion and electron density distributions in the sheath, respectively. By assuming that an ion enters the sheath with Bohm velocity, $u_B=(kT_e/m_i)^{1/2}$, energy conservation, and taking into account momentum conservation in the sheath, without collisions, one can deduce:

$$n_i^*(V) = n_i \frac{\xi L^2}{S(V)} \left(1 - \frac{2eV}{kT_e}\right)^{-\frac{1}{2}}, \quad \text{Eq. (2.2)}$$

Where $\xi=S_{sh}/L^2$, S_{sh} is the area of the sheath edge and $S(V)$ the surface of the equipotential contour corresponding to V . For simplicity one can also approximate $S(V)=a+b\exp(\lambda V)$, with $S(V_{sh})=S_{sh}$ and $S(V_0)=L^2$. This gives [ES7]:

$$S(V) = L^2 \left[1 + \frac{(\xi-1)[\exp(\lambda V_0)-\exp(\lambda V)]}{\exp(\lambda V_{sh})-\exp(\lambda V_0)}\right] \quad \text{Eq. (2.3)}$$

where λ is a constant parameter. According to Bohm criteria $|V_{sh}|=kT_e/2e$, a value that is typically very small with respect to $|V_0|$ when dealing with thick sheath. Considering Boltzmann distribution for electrons and charge neutrality in plasma volume one can evaluate $n_e^*(V)$, with $n_e=n_i=n_0$, where n_e is the electron density and n_i the ion density. As boundary conditions one can assume a zero potential at the edge of the volume of integration (large enough to ensure solution convergence) and $V=V_0$ at the electrode surface. The solution of this calculation is presented as a cross section ($x=0$) in Fig 2.1 (a) and exhibits a mushroom-like shape, where the sheath edge is arbitrary selected to be $V_z=-10$ V. It is important to notice the sheath expansion in the $-z$ direction near the electrode's edge. Once knowing the 3D potential distribution within the sheath (space charge) it is possible to calculate individual trajectories (illustrated with black lines) of ions entering the sheath at locations uniformly distributed on the edge. Despite entering the sheath from its rear-side and very close to the electrode, the ions close to location (1) are reaching the electrode nearly at its center after curving their trajectories with more than 230 degrees. Ions entering between locations (2) and (4) are flying over the electrode's edge and reach a very narrow area at a certain location indicated with y_i . Ions from (4) to (5) are exhibiting only slightly curved trajectories. So far, the most noticeable two aspects are: 1) a large area of electrode surface near the edge is not reached by ions, and 2) a

high current density is expected at location y_1 . Trajectories of 400 ions entering the sheath edge at uniformly distributed locations are presented in Fig. 2.1 (b) in black for ions entering the sheath with $z>0$ (front-side) and in red for $z<0$ (rear-side). Once again is possible to see the non-uniform distribution over the surface, with a certain correlation with the rectangular shape of the electrode.

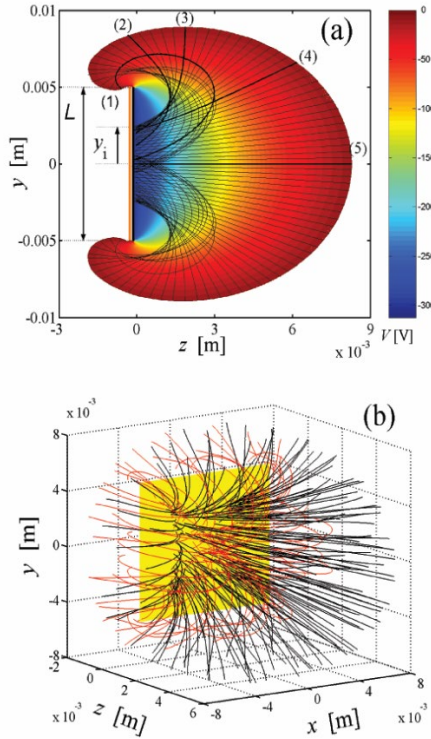


Fig. 2.1 Reproduced with permission from ES1 © 2005, the American Physical Society. (a) $V(x=0, y, z)$ for a square electrode insulated on the rear-side ($-z$ direction) including trajectories of several positive ions entering the sheath at equidistant locations, where $V_0=-300$ V, $n_0=10^{15}$ m $^{-3}$, $T_e=2$ eV and $T_i=0.2$ eV. The color bar indicates the sheath potential. (b) Trajectories of 400 ions passing through the sheath where the read lines correspond to rear-side ions ($z<0$) and black for frontal ions ($z>0$).

After being able to calculate the potential distribution within the sheath becomes possible to investigate in more detail the ion impact location on the electrode surface. For example, the impact locations of 2000 ions are represented in red for rear-side entry locations ($z < 0$) and in black for front-side ($z > 0$) in Fig. 2.2 (a), (b) and (c) for $V_0 = -100$ V, -200 V and -300 V, respectively. It is now evident that rear- and front-side ions exhibit very clear but different patterns. While the black dots are forming a star-like pattern correlated with electrode corners that reduces in size by decreasing V , the red dots form a start-like pattern, correlated with the median x and y axis of the square electrode that increases in size by decreasing V . Since the ion impact

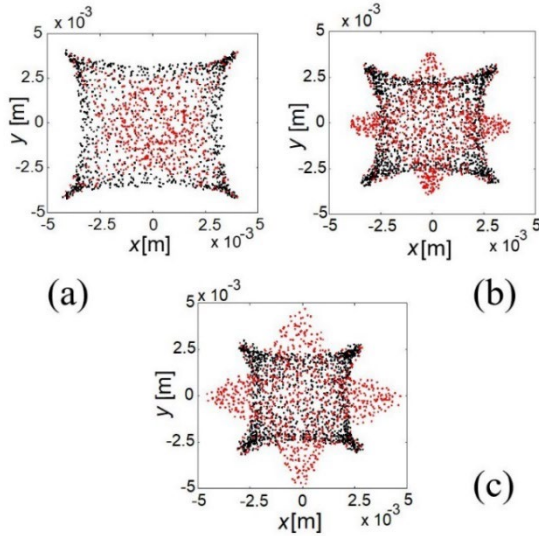


Fig. 2.2 Reproduced with permission from ES2 © 2005, the American Physical Society. The impact location of ions on the surface of square electrodes (10×10 mm²) for (a) $V_0 = -100$ V; (b) -200 V and (c) -300 V, where $n_0 = 10^{15}$ m⁻³ and $T_e = 1$ eV. The rear-side ions are represented with red dots and frontal ions with black dots.

pattern is electrode-shape dependent, additional information can be obtained by calculating the sheath structure and ion trajectories for disk electrodes. The impact locations of 2000 ions for a disk electrode of 5 mm in

radius and insulated on the rear-side are presented in Fig. 2.3 (a), (b) and (c) for similar parameters as in Fig. 2.2. A thinner sheath (Fig. 2.3 (a), $V_0=-100$ V) exhibited a very clear scattered-ring in black, corresponding to the focusing effect noticed for ions entering the sheath between locations (2) and (4). This ring was getting smaller in radius by increasing the sheath thickness. The rear-side ions (red dots) were confined within the black-ring and the focusing at the electrode center was enhanced by decreasing the bias towards -300 V (see Fig. 2.3 (c)). To verify the predicted ion kinetics, disk and square

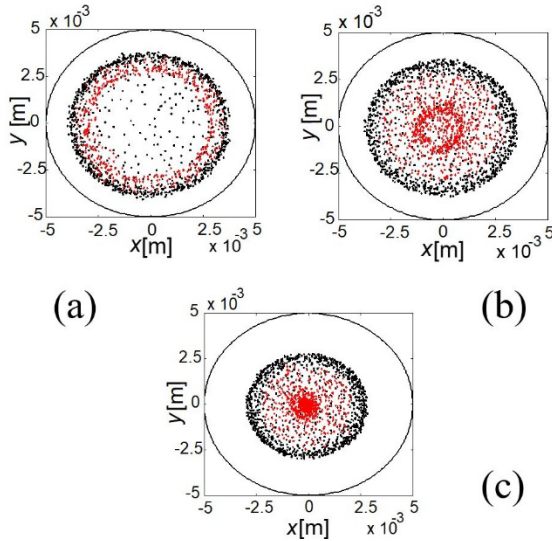


Fig. 2.3 Reproduced with permission from ES2 © 2005, the American Physical Society. The impact location of ions on the surface of disk electrodes (10 mm in diameter) for (a) $V_0=-100$ V; (b) -200 V and (c) -300 V, where $n_0=10^{15} \text{ m}^{-3}$ and $T_e=1 \text{ eV}$. The rear-side ions are represented with red dots and frontal ions with black dots.

electrodes, made of mirror polished gold plates (0.2 mm in thickness) and insulated on the rear-side, have been immersed into an Ar plasma of 10^{15} m^{-3} density and $T_e=1.7 \text{ eV}$ (parameters measured by Langmuir probe). Each electrode was biased for 3 min. The photographs after ion bombardment are

presented in Fig. 2.4 as follows: (a) and (d) for -100 V, (b) and (e) for -200 V, and (c) and (f) for -300 V, respectively. The mild ion sputtering was able to

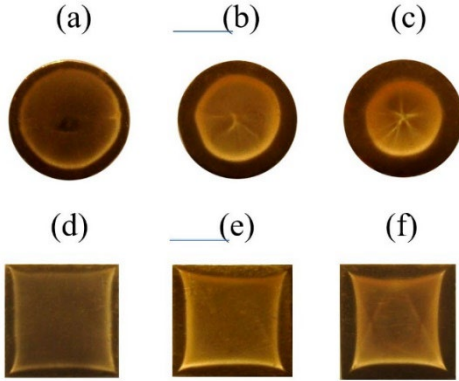


Fig. 2.4 Reproduced with permission from ES2 © 2005, the American Physical Society. Photographs of disk and square electrodes exposed to plasma for 3 min, $n_0 \approx 10^{15} \text{ m}^{-3}$, and $T_e = 1.7 \text{ eV}$ (a) and (d) for $V_0 = -100 \text{ V}$, (b) and (e) for $V_0 = -200 \text{ V}$, and (c) and (f) for $V_0 = -300 \text{ V}$, respectively.

reveal impact locations very well correlated with simulations presented in Fig. 2.2 and Fig. 2.3. Moreover, additional details could be noticed, including a set of radial lines converging to the spot at the center of sample (c) and several lines crossing the sample (f) and less visible for sample (e).

To increase the visibility of the resulted patterns by ion impact and to gain more information about the origin of the radial lines in Fig 2.2 (b) and (c), as well as to clarify if one could remove the red dots from Fig. 2.2 and

Fig. 2.3 by preventing the sheath expansion in the $-z$ direction (rear-side) a new experiment was designed. Disk, square and octagonal electrodes were made of brass (high etching rate) in two sets. The first set was with the electrodes insulated on the rear-side and the second set with electrodes surrounded with a flat-ceramic-surface following the same level as the conducting electrodes. The photographs after 60 min of Ar ion exposure are presented in Fig 2.5. Fig. 2.5 (a) exhibits a very well-defined spot at the center with a large number of irregularly distributed radial lines of different lengths. However, the spot and the lines are absent when the sheath was prevented for rear-side expansion as can be seen from Fig. 2.5 (d). Fig. 2.5 (b) and (c) reveal a set of two straight lines emerging from each corner for the square and octagonal electrodes, with a smaller angle between the lines of the octagonal electrode. The lines were not present for the electrodes without

rear-side sheath expansion as shown in Fig. 2.5 (e) and (f). However, all three electrodes (disk, square and octagonal) preserved the main pattern (shape-dependent) near the electrode edge. Since the radial lines in Fig. 2.5 (a) are very well defined it suggests the possibility of being the result of the fine molding of the sheath-rear by the irregularities of the electrode-edge to insulator interface. To verify this assumption a dodecagon electrode with insulated rear-side was exposed to ion bombardment for 60 min. The photograph is presented in Fig. 2.5 (g) and supports the initial assumption.

For supporting the results presented in Fig. 2.5 with simulations, the sheath structure and ion trajectories have been computed for an electrode insulated on the rear-side, with surrounding insulator and with both-sides conductive ($n_0=10^{15} \text{ m}^{-3}$, $T_e=1 \text{ eV}$, $V_0=-300 \text{ V}$). The simulations are presented in Fig. 2.6 and confirm that without rear-side expansion (see Fig. 2.6 (b)) the sheath is

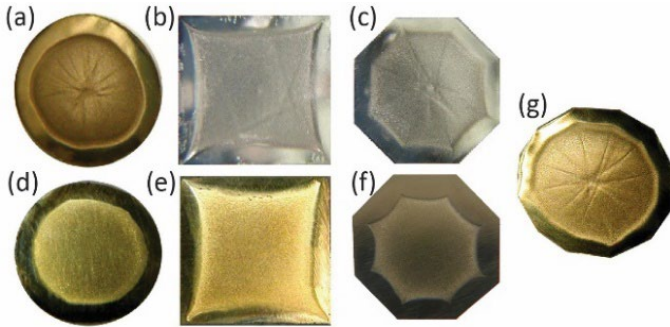


Fig. 2.5 Reproduced with permission from ES2 © 2005, the American Physical Society. Photographs of electrodes made of brass exposed to plasma for 60 min (a) one side-biased disk for, $V_0=-500 \text{ V}$ and $n_0=5 \times 10^{15} \text{ m}^{-3}$, (b) one-side electrode surrounded by insulator for $V_0=-300 \text{ V}$, $n_0=10^{15} \text{ m}^{-3}$, (c) one-side biased octagon for $V_0=-200 \text{ V}$, (d) one-side biased disk surrounded with insulator for $V_0=-300 \text{ V}$ and $n_0=10^{15} \text{ m}^{-3}$, (e) one-side biased square surrounded with insulator for $V_0=-300 \text{ V}$ and $n_0=10^{15} \text{ m}^{-3}$, (f) one-side biased octagon surrounded by insulator for $V_0=-300 \text{ V}$ and $n_0=10^{15} \text{ m}^{-3}$, and (g) one-side biased dodecagon for $V_0=-500 \text{ V}$ and $n_0=10^{15} \text{ m}^{-3}$.

not able to focus ions on the center of the electrode. Moreover, the electrode with both sides conductive (Fig. 2.6 (c)) does not exhibit a particular behavior. Based on such simulations it is possible to calculate the radial distribution of

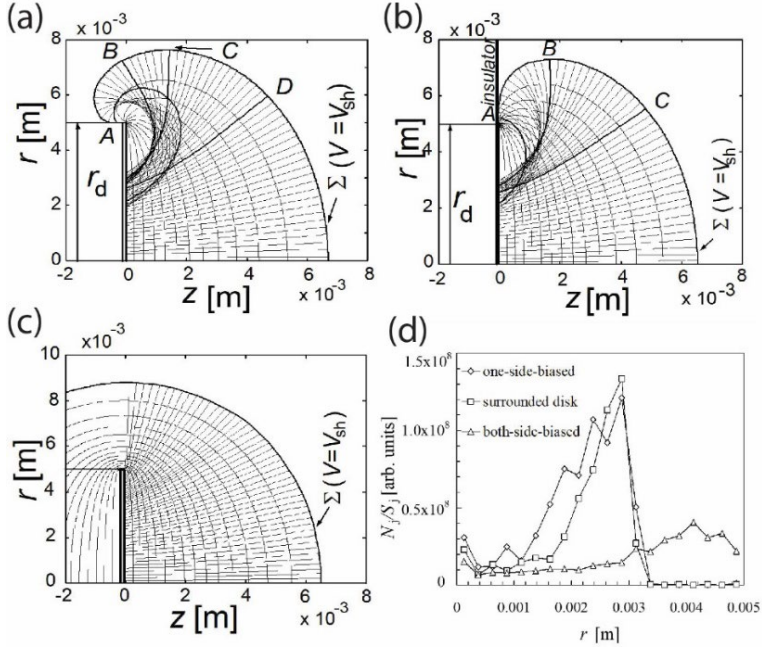


Fig. 2.6 Reproduced with permission from ES2 © 2005, the American Physical Society. Potential distribution, as equipotential contours, and ion trajectories starting from the sheath edge until reaching the surface, (a) for an one-side-biased disk; (b) a biased-disk extended on its plane by an insulator; (c) a both-side-biased disk ($V_0 = -150$ V, $n_i = 10^{15}$ m $^{-3}$ and $T_e = 1$ eV; (d) Current density as a function of r for calculations presented in (a), (b) and (c).

the current density. This result is presented in Fig. 2.6 (d) and shows that an electrode interfacing an insulator is very efficient to produce a sheath that significantly curves ion trajectories for exhibiting certain patterns.

Based on the presented information it is now possible to introduce the following definitions:

- *Passive surface*: the electrode surface not reached by ions.
- *Active surface*: the electrode surface reached by ions.
- *Impact radius*: the radius of the circle delineating the passive and active surfaces (see y_i in Fig. 2.1)
- *Discrete ion focusing*: the ions involved in the abrupt increase in current density at the interface between the passive and active surfaces (see Fig. 2.6 (d)).
- *Modal ion focusing*: ions entering the sheath from its rear-side and that form a sheath-shape-dependent pattern.
- *Modal spot*: the very high current density at the center of a disk electrode formed by the focusing of rear-side ions collected from a large solid angle (see Fig 2.5 (a))
- *Modal rays*: ion focusing of rear-side ions induced by sheath molding due to local non-uniformities at the electrode insulator interface.
- *Modal lines*: set of two lines associated with each corner of a polygonal electrode (see Fig 2.5 (b), (c) and (g)).

The experiments presented so far have been performed in purpose in single ion species plasma (Ar) in a multi-dipolar plasma source that provides a very steady operation at rather low plasma densities (10^{15} m^{-3}) than can produce thick sheaths for an electrode bias $|V_o| < 500 \text{ V}$. For this case, mirror polished gold and brass electrodes have been used to visualize the modal and discrete ion focusing effects.

To increase complexity, by considering multi ion species plasma, and improve the visibility of discrete focusing and modal lines, additional experiments have been performed in reactive gases such as Ar/SF₆ using an inductively coupled plasma (ICP) source, where plasma density could be raised at 10^{16} m^{-3} and $|V_o|$ at 1kV, while low-resistivity silicon squares ($10 \times 10 \text{ mm}^2$ and 0.5 mm in thickness) were used as electrodes. 3D depth profiles after etching were measured with a phase-shift-interferometry optical profilometer and are presented in Fig. 2.7 (b) for an electrode surrounded by an insulator (see schematic in Fig. 2.7 (a)) and (e) for an electrode insulated on the rear-side

(schematic in Fig. 2.7 (d)). The modal lines visibility is remarkable as well as the ability of the surrounding insulator to inhibit them and reveal only the discrete focusing. As simulation capability, the impact locations of 90156 frontal-ions exhibiting the discrete focusing are presented in Fig. 2.7 (c) and for 56545 rear-side ions exhibiting the modal lines are presented in Fig. 2.7 (f). While discrete focusing is easier to capture by simulations, the modal lines are not yet as well defined as visualized by experiments. The main difficulty lies in the ambiguity of deciding the proper sheath edge where the ions are to be injected and their velocity at that boundary.

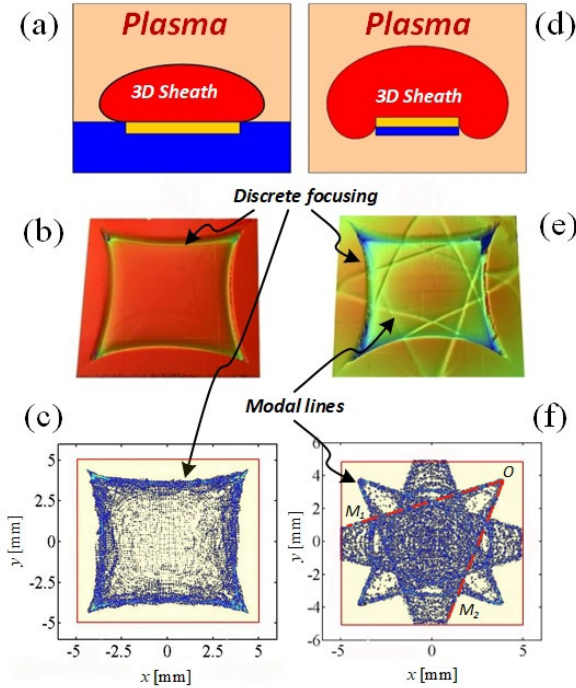


Fig. 2.7 Schematic of plasma and the 3D sheath for (a) an electrode surrounded with an insulator and (d) rear-side insulator; (b) discrete focusing effect on a silicon substrate surrounded with an insulator and (e) modal and discrete focusing effects; ion impact locations exhibiting the (c) discrete focusing effect by frontal ions and (f) modal lines exhibited by rear-side ions.

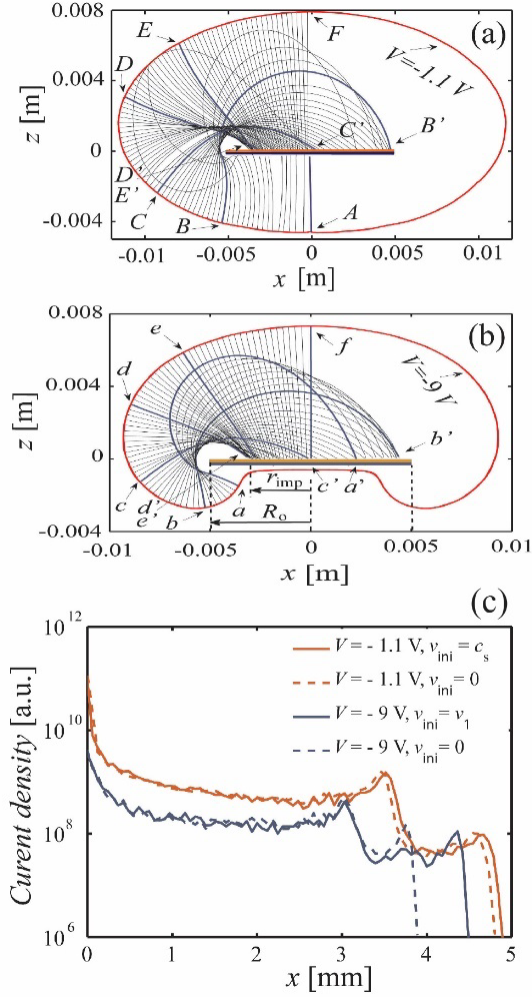


Fig. 2.8 Reproduced with permission from ES3 © 2012, the Institute of Physics Publishing Ltd. Ion trajectories entering the sheath edge at different locations for (a) $V_{sh} = -1.1$ V and (b) $V_{sh} = -9$ V, where $V_0 = -300$ V, $n_0 = 10^{15} \text{ m}^{-3}$, $T_e = 2.2$ eV, (c) Radial distribution of the current density of ions entering the sheath for $V_{sh} = -1.1$ V and $V_{sh} = -9$ V with continuous lines for ion trajectories that have been calculated assuming that ions are pre-accelerated and with dashed lines for $v_{ini} = 0$.

This aspect was investigated and is briefly presented in Fig 2.8 where ion

trajectories are calculated (a) for a sheath edge corresponding to Bohm criteria ($V=-1.1V$) and (b) for a sheath edge corresponding to $V=-9V$ for disk electrodes of 10 mm in diameter. For both sheath edge contours (illustrated in red in Fig 2.8 (a) and (b)) the radial distribution of the current density is calculated by assuming that ions enter the sheath with a velocity $v_{ini}=0$ (dashed lines) or Bohm velocity (see c_s) for $V=-1.1 V$ or the velocity v_1 given by the kinetic energy corresponding to the local potential of the chosen sheath boundary ($V=-9 V$) with respect to plasma potential (set to 0 V). From these simulations one can see that the rear-side ions are exhibiting an impact radius larger than that of discrete focusing (see also B' and b' in Fig 2.8 (a) and (b)). While the discrete focusing is less sensitive to v_{ini} but dependent on the chosen sheath edge, the rear-side ions are sensitive to both parameters.

This finding triggered a detailed investigation (see ES4) as to see if the rear-ions can exhibit an impact radius larger than that of discrete focusing. For this purpose, two disk electrodes have been exposed for 15 min in Ar/SF₆ plasma being biased at $-150 V$ and $-300 V$ respectively. The ion focusing patterns by etching are presented in Fig. 2.9 (a) for $-150 V$ and (b) for $-300 V$. The radial distribution of the depth was measured by an optical profilometer, and the resulted profiles are presented in black for $-150 V$ and in red for $-300 V$, respectively. Both samples exhibited the discrete ion focusing (D_1 and D_2) and the modal spot at the center (M_1 and M_2). However, one more ring could be identified for each sample: F_1 and F_2 , defined as modal ring. The possible explanation for the modal ring formation is presented in Fig. 2.9 (d) where a 2D potential distribution is presented together with ion trajectories entering the sheath with $V_{sh}=-5 V$ ($n_0=10^{15} m^{-3}$, $T_e=2.2 eV$, $V_0=-150 V$, $V_{pl}=0 V$). The main idea is that rear-side ions can reach not more than a certain location C' that depends on the sheath thickness and consequently on how much the sheath is expanding on the rear side. At that location, rear-ions are focused and reach the electrode surface under low incidence angles, a fact that promotes higher etching yields. The resulting ring can be described with a modal radius, r_m , that can be lower or larger than r_{imp} . Fig. 2.9 (e) presents the impact of 23470 rear-ions and 41108 frontal ions, representing all ions

entering the sheath edge for $V_0 = -300$ V. For this case $r_m > r_{\text{imp}}$, corresponding to the experimental situation presented in Fig 2.9 (b).

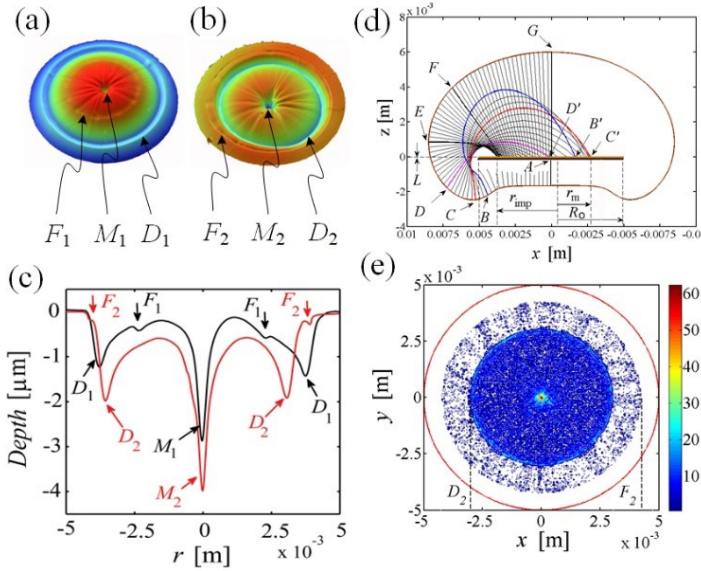


Fig. 2.9 Reproduced with permission from ES4 © 2015 American Institute of Physics Publishing LLC. (a) The surface profile after etching by impinging ions for (a) $V_0 = -150$ V and (b) -300 V in Ar/SF₆ at 3 mTorr, for a discharge current of 100 mA, discharge voltage of 70 V and 15 minutes exposure time. (c) 1D depth profiles for the two samples presented (a) and (b) where locations corresponding to discrete focusing are indicated with D_1 and D_2 , those of the modal spot with M_1 and M_2 and the additional rings with F_1 and F_2 . (d) Two-dimensional cross section of the potential distribution and individual ion trajectories for $n_0 = 10^{15} \text{ m}^{-3}$, $T_e = 2.2 \text{ eV}$, $V_0 = -150 \text{ V}$, $V_{\text{pl}} = 0$ and $V_{\text{sh}} = -5 \text{ V}$ and (e) Ion impact locations on the electrodes surface for $V_0 = -300 \text{ V}$ ($n_0 = 10^{15} \text{ m}^{-3}$, $T_e = 2.2 \text{ eV}$) with 23470 rear-side ions ($z < 0$) and 41108 frontal ions ($z \geq 0$), where F_2 corresponds to r_m and D_2 to r_{imp} .

When taking into consideration electrodes with corners the focusing pattern gets more complicated (see Fig. 2.7) so that the modal lines formation needs additional information. From Fig. 2.5 (b) and (c) we know that each corner generates two modal lines. In this regard, Fig. 2.10 shows in red the equipotential surface of sheath edge for a square electrode (in yellow,

insulated on the rear-side) only for the right up corner and negative z . The generated modal lines on the surface are illustrated as impact locations in blue and black. The same colors indicate the entrance location in the sheath for each trajectory (see lines OM_1 and OM_2 in Fig. 2.7 (f)). Now is easier to see that each modal line is the result of ion focusing on different directions, at the same time correlated with gradient changes on the sheath surface. This understanding further supports the idea of a very well-defined sheath boundary. For example, if ions have a large spread in energy at the sheath edge, equivalent with a shallow presheath-sheath transition, then the modal lines will be less defined than we can see. Moreover, it can be very easy to trace the difference between a collisions-less and collisional sheath by just monitoring the modal lines.

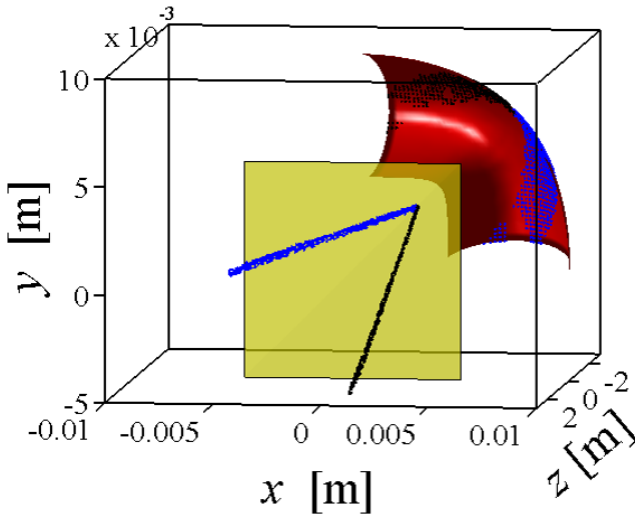


Fig. 2.10 The corresponding location on the sheath edge of ions forming two modal lines on the electrode surface. One quarter of the electrode surface is shown in yellow the quarter of the rear-side sheath edge is presented in red.

2.2 Negative ion focusing

Surface induced processes by positive ions implies a negative bias at the electrode. It accelerates ions at a desired energy but also repels the electrons, with a direct impact on the transported heat flux. When biasing positively an electrode with respect to plasma potential, V_{pl} , in an electropositive discharge (negative ion density, $n_{ni}=0$) one expects *i*) an increase of V_{pl} , *ii*) significant surface heating by electrons and *iii*) ignition of an anodic-glow-discharge due to the significant increase in the flux of secondary emitted electrons. In this scenario, one can get an electron sheath only for a very small positive bias with respect to V_{pl} . However, the negative ions presence (electronnegative discharges) is expected to significantly affect the plasma parameters. For

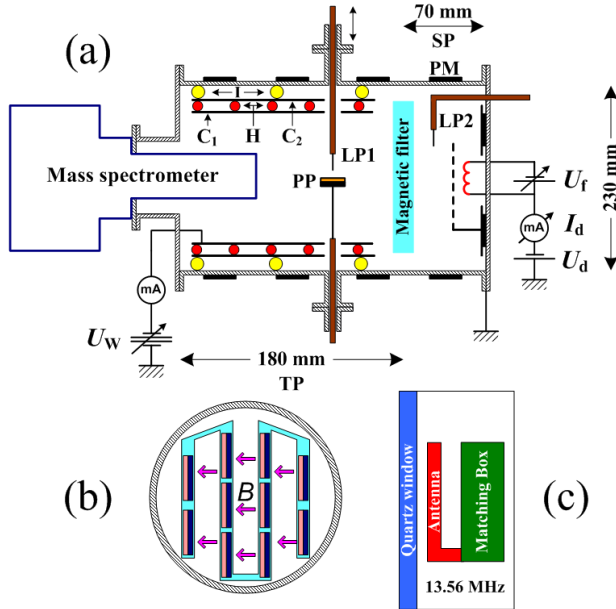


Fig. 2.11 Reproduced with permission from E55 © 2010 American Institute of Physics Publishing LLC. (a) The experimental setup: PM-permanent magnets; C_1 , C_2 -metallic cylinders; H-heater; PP-planar probe; LP1, LP2-Langmuir probes; I-insulators; SP-source plasma region; TP-target plasma region; (b) magnetic filter; (c) the ICP module.

example, if n_{ni}/n_e is the density ratio of electron to negative ion, one expects

a significant reduction of the heat flux and a possible inhibition of the anodic-glow-discharge because a significant number of electrons is replaced (by electron attachment) with negative ions for $n_{ni}/n_e > 10$. To answer these questions, the main properties of electronegative discharges in dc and ICP operation modes have been investigated as presented in ES5 and ES6. A special experimental setup was built as shown in Fig. 2.11. A cylindrical vacuum chamber of 300 mm in diameter and 300 mm in length (see Fig. 2.11 (a)) was divided into two regions (source plasma, SP, and target plasma, TP) using a magnetic filter presented in Fig. 2.11 (b). The filter could provide about 500 Gauss between two consecutive lines and its purpose was to promote negative ion formation by reducing T_e in the TP by increasing the collision rate. The wall losses were reduced with a magnetic-cusp configuration. Langmuir probes were placed in both SP and TP and a mass spectrometer with floating optics (able to detect negative ions) was placed at the end of the TP. A large

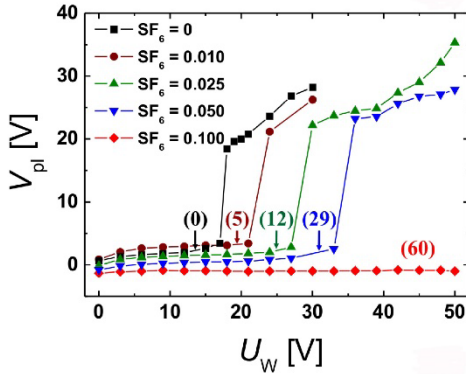


Fig. 2.12 Reproduced with permission from ES6 © 2010 Institute of Physics Publishing Ltd. Plasma potential as a function of U_w for different SF_6 flow rates.

cylindrical wall was placed inwards, concentric with TP at distance of 10 mm from it. The additional wall could be biased with a dc power supply, U_w , to investigate the influence on V_{pl} and it could also be heated to promote surface desorption. In dc configuration the plasma was produced with a hot and emitting filament by applying a discharge voltage, U_d , between the filament as cathode and the grounded anode, sustaining a discharge

current, I_d . This configuration was generating a low-density plasma, with very good stability (no mode jumps and very low level of fluctuations), perfectly suited for basic experiments. V_{pl} as a function of U_w is presented in Fig. 2.12 for different flows of SF_6 while keeping the Ar flow constant at 2 sccm. Values in parentheses correspond to n_{ni}/n_e . Noticeably, V_{pl} jumps with more than 20

V and keeps increasing for U_w higher than the ionization potential for Ar (15.7 V) as long as $n_{ni}/n_e < 30$. However, V_{pl} was not affected by U_w for $n_{ni}/n_e > 30$. A small disk-probe (10 mm in diameter) was used to test the anodic-glow-discharge ignition for different I_d . The disk-probe current, I_{pp} , as a function of the positive applied bias, V_{pp} , is presented in Fig. 2.13 (a) for different I_d in Ar

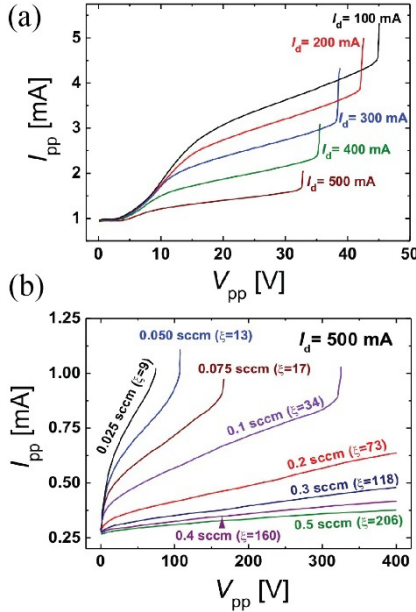


Fig. 2.13 Reproduced with permission from ES6 © 2010 Institute of Physics Publishing Ltd. Current-voltage characteristics (a) for different discharge currents in Ar plasma for a constant flow of 2 sccm ($SF_6 = 0$ sccm); (b) for different SF_6 flow rates at a constant Ar flow of 2 sccm and discharge current $I_d = 500$ mA.

plasma ($n_{ni}=0$), where from one can see the very sharp transitions to glow at V_{pp} potentials below 50 V. $I_{pp}(V_{pp})$ for different SF_6 flows is presented in Fig. 2.13 (b) where $\xi = n_{ni}/n_e$. Very importantly, one can apply $V_{pp} > 200$ V without igniting an anodic-glow-discharge for $n_{ni}/n_e > 20$. V_{pl} and n_{ni}/n_e as a function of the SF_6 flow are presented in Fig. 2.13 (c) for $V_{pp}=0$ V in black and $V_{pp}=200$ V in red. At this point, it is possible to conclude that in an dc electronegative discharge produced in Ar/ SF_6 gas one can bias positively small or large electrodes without elevating V_{pl} , igniting a glow-discharge or affecting plasma density as long as $n_{ni}/n_e > 20$. This also means that one can generate a negative sheath of a certain thickness, dominated by negative ions.

When operated in ICP mode the discharge exhibits two regimes of low- and high-density, with a sharp transition (between 500 and 600 W) as can be shown from Fig. 2.14 (a) where a set of Langmuir probe characteristics are presented for different discharge powers. With U_a defined as the positive bias exhibiting the transition from a

negative sheath to anodic-glow-discharge, (see Fig. 2.13 (a)) the U_a as a function of power for different Ar/SF₆ flows and constant discharge pressure

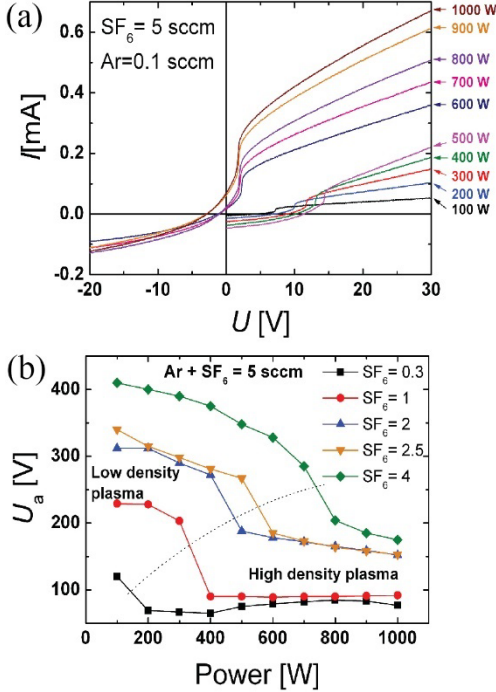


Fig 2. 14 Reproduced with permission from ES5 © 2010 American Institute of Physics Publishing LLC. (a) Probe characteristics for different discharge powers at 3 mTorr in Ar flow of 0.1 sccm and SF₆ flow of 5 sccm. (b) The potential corresponding to the transition negative sheath – anodic glow as function of power for different SF₆ flows when $p=3$ mTorr and a total gas flow of 5 sccm.

(3 mTorr) is presented in Fig. 2.14 (b). While $U_a > 200$ V could be possible, without ignition, for ICP powers below 800 V and SF₆ flows above 1 sccm, U_a was significantly lower in the high-density plasma regime due to a higher recombination rate of negative ions with electrons, and consequently lower n_{ni}/n_e .

SF₆ is a large molecule, and its dissociation depends on the electron energy distribution function which correlates with process parameters such as discharge pressure and power. It is therefore important to know what positive and negative ion species are expected to be produced. Typical mass spectra for the dc discharge in Ar/SF₆ are presented in Fig. 2.15 (a) for positive ions and (b) for negative ions (150 mA,

0.5 sccm Ar and 0.3 sccm SF₆). While more than 7 positive ion species can be identified, only F⁻, SF₅⁻ and SF₆⁻ are noted as negative ion species. It is important to mention that the cross section for F⁻ formation is centered around $T_e \sim 1$ eV while for SF₅⁻ and SF₆⁻ increase with T_e decreasing from below

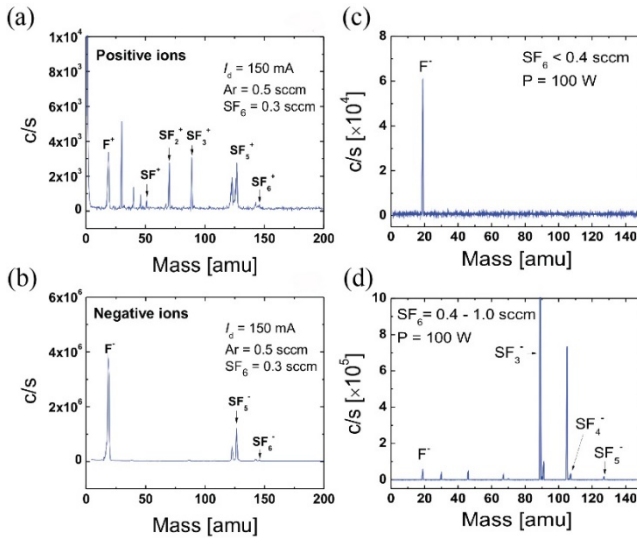


Fig. 2.15 Reproduced with permission from E55 © 2010 American Institute of Physics Publishing LLC. Typical mass spectra for (a) positive and (b) negative ions for a discharge current of 150 mA, Ar flow of 0.5 sccm and SF_6 flow of 0.3 sccm. Negative ion mass spectra measured for ICP mode (100 W) for SF_6 flows (c) lower than 0.4 sccm and (d) equal or larger than 0.4 sccm.

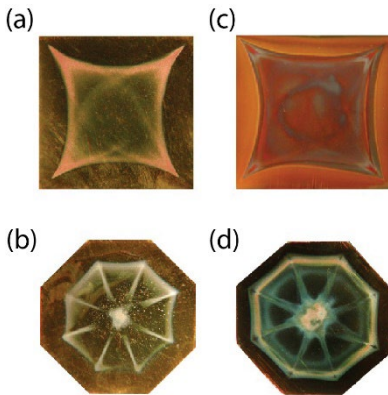


Fig. 2.16 Reproduced with permission from E51 © 2005, the American Physical Society. Photographs of square and octagonal electrodes exposed (a) and (b) to CF_4 plasma ($n_{ni}/n_e=4$), for 5 min with $V_0=300$ V; (c) and (d) in Ar/SF_6 plasma ($n_{ni}/n_e=17$) for 5 min with $V_0=200$ V.

0.7 eV. The negative ion species in ICP at 100 W for SF_6 flow below 0.4 sccm and SF_6 flow from 0.4 to 1 sccm are presented in Fig. 2.16 (c) and (d) respectively.

Now we can summarize some relevant electronegative plasma properties: it is possible to create a stable negative sheath dominated by negative ions by ensuring $n_{ni}/n_e > 10$. This condition will inhibit the anodic-glow formation and will prevent the rise of V_{pl} . Such context makes it possible to verify if the modal and discrete focusing effects are also manifesting for negative ions. This experiment is presented in Fig. 2.16 where square and octagonal electrodes

reveal the modal and discrete focusing effects of negative ions (a) and (b) in CF_4 plasma and (c) and (d) in Ar/SF_6 plasma. The electrodes are made of brass (insulated on back-side) with a thin layer of cooper on the surface to be able pattern visualization in very short time (2 min).

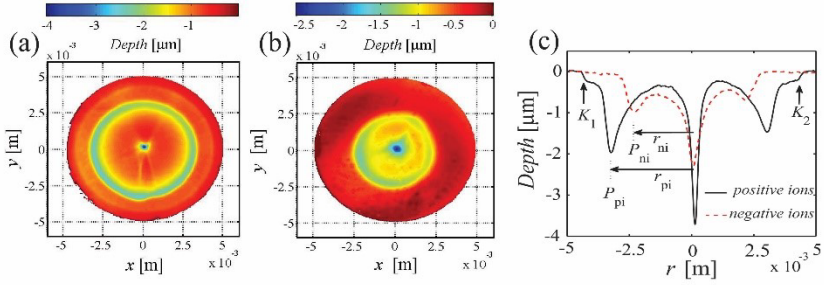


Fig. 2.17 Reproduced with permission from ES4 © 2015 American Institute of Physics Publishing LLC. The depth profiles for two disks exposed for 15 min to (a) -300 V and (b) 300 V where $V_{pi} = -11$ V, $n_o = 1.2 \times 10^{15} \text{ m}^{-3}$, $T_e = 1.7$ eV and $n_{ni}/n_e = 57$. The diagonal scans are presented in (c) with full line for positive ions and dashed line for negative ions.

Nevertheless, electrons are also reaching the electrode surface, but their mass is much smaller so that the focusing patterns are the result of negative ion impact. The potential structure of the presheath-sheath structure is an energy analyzer, in the sense that ions entering this system with different energies should reach the electrode surface at different locations. As more than one negative ion species is expected in both SF_6 and CF_4 plasmas, it is relevant to ask if different ion velocities at the sheath edge could result in separate patterns. So far, no obvious conclusion can be deduced from the four patterns presented in Fig. 2.16. Another relevant question concerns the thickness of positive and negative sheaths for a similar applied bias with respect to V_{pi} . Should one expect significant differences? To answer this, two disk-electrodes (10 mm in diameter) have been exposed for 15 min in Ar/SF_6 ($V_{pi} = -11$ V, $n_o = 1.2 \times 10^{15} \text{ m}^{-3}$, $T_e = 1.7$ eV and $n_{ni}/n_e = 57$). The first one was biased at -300 V with respect to V_{pi} while the second was biased at 300 V. The resulting patterns after developing the discrete and modal focusing effects are presented in Fig. 2.17 (a) and (b), respectively. The depth profiles crossing

the disk centers are presented in Fig. 2.17 (c). This result undoubtedly demonstrates that the negative sheath is thicker than the positive sheath. A possible explanation can be that the energetic electrons are reaching closer to the electrode for a positive ions sheath.

2.3 Ion focusing by 3D magnetized plasma-sheath-lenses

The Lorentz force is acting on charged particles forcing them to gyrate along the magnetic field lines. As presented in section 1.5, the magnetic field is often used in various plasma sources, and it is expected to also have a

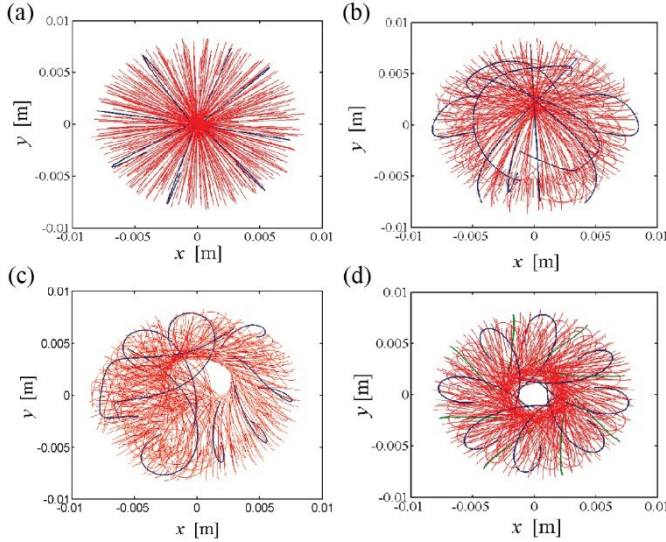


Fig. 2.18 Reproduced with permission from ES3 © 2012, the Institute of Physics Publishing Ltd. Ion trajectories (a) $B_{x,y,z}=0$ Gauss, (b) $B_{x,z}=0$ and $B_y=2000$ Gauss, (c) $B_x=0$, $B_{y,z}=2000$ Gauss, and (d) $B_{x,y}=0$ and $B_z=2000$ Gauss (where $n_0=10^{15} \text{ m}^{-3}$, $T_e=2.2 \text{ eV}$ and $V_0=-300 \text{ V}$).

significant influence on the discrete and modal ion-focusing-effects. A self-consistent approach for including the magnetic field in the 3D simulation model used so far is not possible. However, it is possible to work with a

simplified model by just adding a 3D magnetic field to the 3D potential structure and calculate the ion trajectories considering the Lorents force.

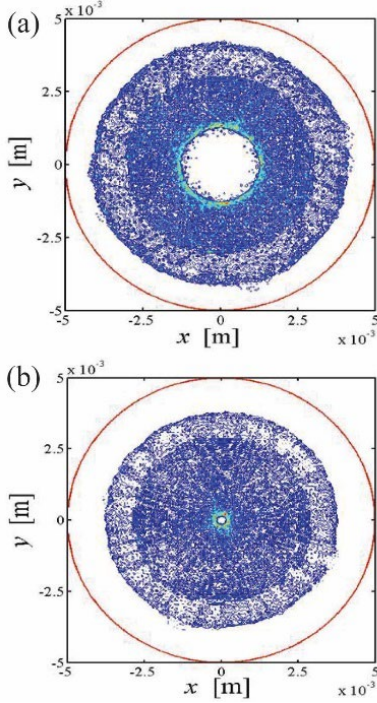


Fig. 2.19 Reproduced with permission from ES3 © 2012, the Institute of Physics Publishing Ltd. Impact location of 18820 rear ions for $B_x=B_y=0$ Gauss, $B_z=1000$ Gauss and (a) $m_i=1$ and (b) $m_i=40$.

Based on this simplification, trajectories of 457 hydrogen rear-side ions are presented for different magnetic field configurations in Fig. 2.18 as following: (a) $B_x=B_y=B_z=0$ Gauss, (b) $B_x=B_z=0$ and $B_y=2000$ Gauss, (c) $B_x=0$, $B_y=2000$ and $B_z=2000$ Gauss, and (d) $B_x=B_y=0$ and $B_z=2000$ Gauss (where $n_0=10^{15} \text{ m}^{-3}$, $T_e=2.2 \text{ eV}$ and $V_0=-300 \text{ V}$). For visibility, several ion trajectories are presented in blue. Without magnetic field the ion trajectories are preserving the symmetry being contained in a 2D plane perpendicular to the electrode surface. $B_y=2000$ Gauss (see Fig. 2.18 (b)) induces a strong anisotropy while the presence of B_y and B_z preserves a certain noticeable distribution (Fig. 2.18 (c)). Most relevant is the case presented in Fig. 2.18 (d), where the magnetic field is perpendicular to the electrode surface with an effect of uniform twisting of ion all trajectories that at the end forms a new passive surface

at the center of the electrode. A more detailed simulation is presented in Fig. 2.19 where the impact locations of 18820 rear ions are calculated for $B_z=1000$ Gauss and (a) hydrogen ions and (b) Ar ions.

3. Applications of 3D plasma-sheath-lenses

3.1 Plasma immersion ion implantation

Ions with energies above a few thousand eV can penetrate solid surfaces up to 100 nm. This process is named ion implantation and can be used to modify optic, electric, mechanical, or other surface properties.^{5,142} The conventional approach is to extract an ion beam from plasma, further modify it (acceleration, mass section, transport) and then expose the surface to be treated by controlling the ion dose and surface coverage. However, to compensate for difficulties encountered when aiming to uniformly treat complex 3D shapes with high throughput, a new approach was introduced. Instead of extracting the ions from plasma the object to be treated is immersed into plasma and biased negatively to form a positive sheath molding over the 3D object.^{5,33,142} The accelerated ions will impinge on the surface and perform the implantation all over the exposed surface. To avoid

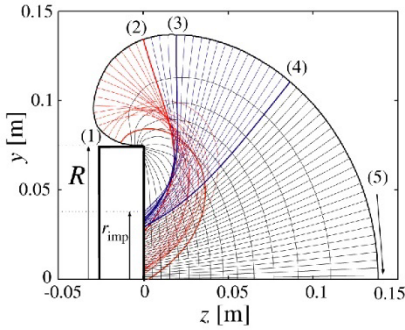


Fig. 3.1 Reproduced with permission from ES7 © 2005 American Institute of Physics Publishing LLC. Potential distribution in the sheath $V(x=0, y, z)$ represented by equipotential lines, together with several ion trajectories, where $V_0=-10$ kV, $R=75$ mm, $n_i=n_e=10^{15}$ m⁻³ and $T_e=3$ eV;

arcing and positive charge accumulation the bias is pulsed with a pulse duration that can allow the sheath to form (above 1 microsec). This method is named plasma immersion ion implantation (PIII) and has been successfully used for more than 3 decades for surface modification, including doping of silicon wafers.⁵ Despite this success, there are certain limitations mainly arising from non-uniform coverage. For example, Fan et al.¹⁷⁹ reported a stage induced dose non-uniformity that was associated with a charging effect

of the dielectric used to reduce contamination. That report triggered the interest of investigating if that observation is not caused by ion focusing

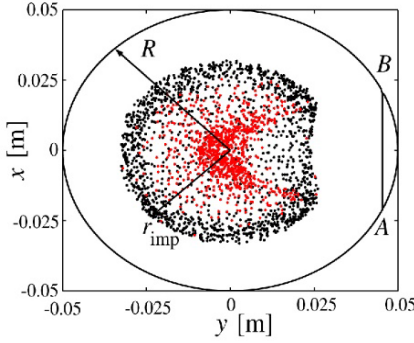


Fig. 3.2 Reproduced with permission from ES7 © 2005 American Institute of Physics Publishing LLC. Impact locations of 3500 ions, with red dots for ions with $z_0 < 0$ and black dots for ions with $z_0 > 0$, where $V_0 = -7$ kV, $R = 50$ mm, $n_i = 10^{15} \text{ m}^{-3}$ and $T_e = 3$ eV.

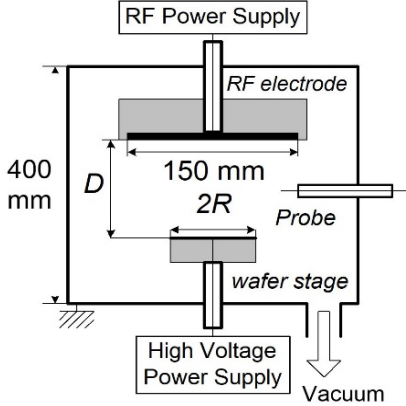


Fig. 3.3 Reproduced with permission from ES7 © 2005 American Institute of Physics Publishing LLC. Schematic diagram of the CCP reactor including the top electrode and the wafer stage.

within a 3D plasma sheath lens. It resulted in publications related to PIII presented in ES7, ES8 and ES9.

Using the simulation procedure described in 2.1 the 3D potential distribution to a wafer of 150 mm in diameter placed on a dielectric stage of 25 mm in height is presented in Fig. 3.1 ($V_0 = -10$ kV, $n_0 = 10^{15} \text{ m}^{-3}$ and $T_e = 3$ eV). The trajectories of rear-side ions ($-z$) are presented in red and follow the same behavior as presented in Fig. 2.6, with certain ions reaching the wafer center. The large number of ions entering the sheath between locations (2) and (4) (trajectories illustrated in blue) are forming the discrete ion focusing effect with an impact radius of 0.037 mm and a passive surface for $r_{\text{imp}} < y < R$, where R is the wafer radius (75 mm). The trajectories of other frontal ions are presented in black (locations from (4) to (5) and exhibit a mild curvature. This result is not surprising as Fig. 3.1 can be regarded just as an upscaling of what is presented in Fig. 2.6. To capture additional details, the impact locations of 3500 ions were calculated for a wafer of 100 mm in diameter that was placed on a

dielectric stage with the same diameter. The wafer cut was also considered in the wafer geometry, while the stage preserved the cylindrical shape. The results are presented in Fig. 3.2 with red dots for rear-side ions and black dots for frontal ions. Remarkably, the presence of the wafer cut (see line AB) influenced both the discrete focusing and the modal focusing effects. Since

the stage follows the rounded shape, it prevented the sheath expansion on the rear-side and consequently, there were fewer red dots towards the wafer center. Moreover, one can notice a parabolic like distribution facing the AB line.

To investigate experimentally the distribution predicted by simulations a dedicated setup was built as presented in Fig. 3.3. An RF electrode (150 mm in diameter) was used to generate capacitively coupled plasma (CCP) driven at 13.56 MHz in a vacuum chamber of 400 mm in length and 300 mm in diameter. A silicon wafer of 100 mm in diameter, with wafer cut, was placed on a cylindric dielectric-stage of same diameter. The plasma was generated in H_2 and the pulse power supply was connected

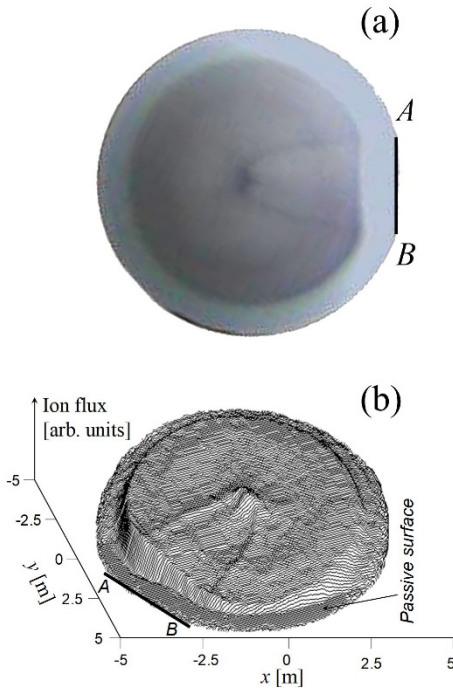


Fig. 3.4 Reproduced with permission from ES7 © 2005 American Institute of Physics Publishing LLC. (a) Photograph of a wafer exposed for 30 min to the pulsed bias where $V_0 = -9.7$ kV, $\delta t = 30$ μ s, $\nu = 33$ Hz, $n_e = 8 \times 10^{14}$ m $^{-3}$, $T_e = 3.7$ eV, $P = 50$ W and 15 mTorr gas pressure; (b) The surface analysis using the color pattern of the wafer shown in (a).

to the wafer. Plasma parameters were monitored by a Langmuir probe.

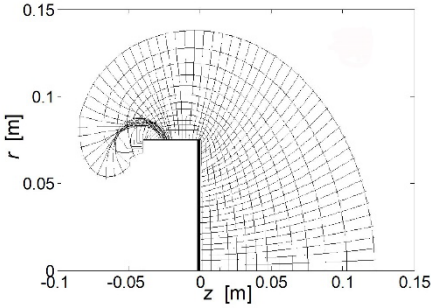


Fig. 3.5 Reproduced with permission from ES9 © 2006, Elsevier B. V. Wafer with a biased vertical ring where $V_0 = -15$ kV, $n_0 = 10^{15} \text{ m}^{-3}$ and $T_e = 3$ eV.

For example, a photograph of a silicon wafer (100 mm in diameter with a cut, AB , on the lateral side and placed on a disk stage with the same diameter) after been exposed for 30 min to a pulse bias of $V_0 = -5$ kV, 33 μsec pulse width and 33 Hz repetition rate is presented in Fig. 3.4 (a). For better visibility, the color pattern converted to a 3D profile is presented in Fig. 3.4 (b). By analogy with other results presented in 2.1, one can

recognize the passive surface and the discrete focusing. Remarkably, the parabola-like profile, near the flat, is very well visible and correlates extremely well with that predicted by simulations. It is now clear that the stage near the cut prevents the sheath from expanding in the rear side direction, creating a shadowing effect at the wafer center [46]. This very good but qualitative agreement between experiment and simulation made it possible to investigate adequate geometries that can improve the ion flux uniformity. Such an example is presented in Fig. 3.5 where the sheath profile and ion trajectories are presented for a wafer of 150 mm in diameter ($n_0 = 10^{15} \text{ m}^{-3}$, $T_e = 3$ eV and $V_0 = -15$ kV) that was placed on a cylindrical stage having the lateral side made of conducting material instead of a dielectric. Such an approach translated the discrete focusing effect on the lateral side and drastically improved the ion dose over the wafer surface.

It is now evident that insulating-conducting interfaces are promoting potential distributions with very high curvature for their equipotential lines, a fact that translates in curved ion trajectories, and manifestation of focusing effects. A relevant question would be to what extent this phenomenology could be used to control the ion dose during PIII?

Let us consider a conductive 3D object as presented in Fig. 3.6 (a) that needs to be uniformly implanted by PIII. The potential distribution and ion

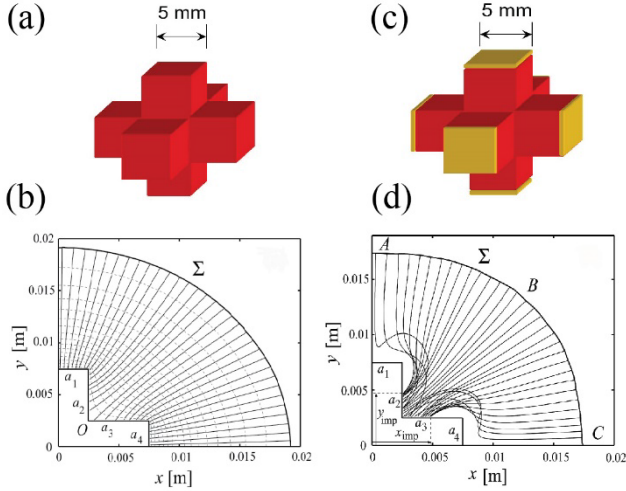


Fig. 3.6 Reproduced with permission from ES8 © 2006, Elsevier B. V. 3D conduction object, (a) all elements conducting (c) insulated elements in yellow, (b) Sheath edge and ion trajectories for all-conducting-faces object, (d) sheath edge and ion trajectories when the faces indicated in yellow are insulated.

trajectories are presented in Fig. 3.6 (b) and show a lower ion dose at the corner indicated with O . Let now assume that some surface elements (see α_1 and α_4) are converted (for example by coverage) to be insulating instead of conducting as presented in Fig. 3.5 (c) where the insulating elements are illustrated in yellow. The recalculated potential distribution is presented in Fig. 3.5 (d) and shows a considerable increase of the ion dose at the corner formed by α_2 and α_3 , plus the formation of passive surfaces indicated with x_{imp} and y_{imp} . This example emphasizes the possibility to customize conducting-insulating interfaces with the aim of reaching or avoiding certain locations of a 3D object to be surface treated by PIII.

3.2 Plasma diagnostics

Precise tuning of plasma aided processes such as etching, thin film deposition, ion beam extraction and PIII involves not only the control of general parameters such as discharge pressure and power but n_o , T_e , V_{pl} and the electron energy probability function (EEPF).^{180–182} Moreover, for processes

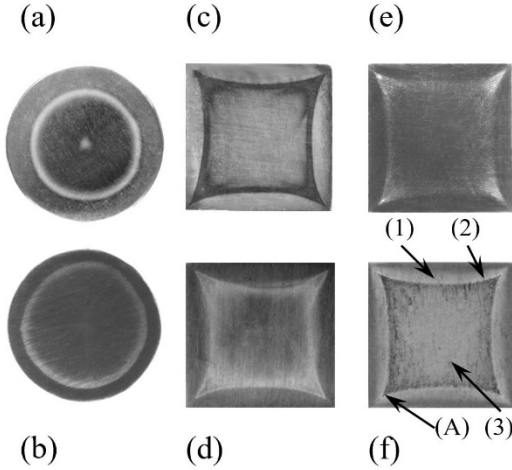


Fig. 3.7 Reproduced with permission from ES10 © 2004 American Institute of Physics Publishing LLC. (a) SLP made of gold, $r_p=5\text{mm}$, treated for 2 min in Ar/SF₆ plasma ($p=3$ mTorr, SF₆ 5%, $V_o=250$ V, $n_i=8.3\times 10^{15}\text{ m}^{-3}$ and $n_{ni}/n_e=46$); (b) SLP ($r_p=7.5$ mm) treated for 20 min in O₂ where $V_o=100$ V, $n_{ni}/n_e=7$, $n_i=7.9\times 10^{15}\text{ m}^{-3}$ and $p=5$ mTorr; (c) SLP made of gold ($l_p=10$ mm) treated for 30 sec in similar conditions as for the sample (a); (d) Cooled SLP treated in Ar/SF₆ for 15 min, $V_o=200$ V, $l_p=15$ mm, $p=0.5$ mTorr and $n_i=4.7\times 10^{15}\text{ m}^{-3}$; (e) Cooled SLP ($l_p=15$ mm) treated in O₂ plasma for 20 min, for $V_o=200$ V, $p=0.5$ mTorr and $n_i=3.6\times 10^{15}\text{ m}^{-3}$, (f) Clean surface of a SLP made of gold ($l_p=10$ mm) treated for 5 min in similar conditions as SLPs from (a) and (c) except for $V_o=300$ V;

with reach chemistry, as etching, it is also important to know the radicals and the ion species present in the discharge.¹³² As

presented in 1.4, most reactive gases are also electronegative (H₂, O₂, SF₆, CF₄, Cl₂) and the negative ions presence influence plasma properties and complicates the diagnostics methods.

For example, one needs a different procedure for interpreting the current-voltage characteristic, $I_p(V_p)$, of a Langmuir probe, where I_p and V_p are the probe current and probe bias, respectively.¹⁸³ For $V_p > V_{pl}$ the probe will

collect negative charges (the positive ion current decays very fast, within a couple of volts) and the electrons replacement with negative ions will result in an $I_p(V_{pl})$ reduction that scales will n_{ni}/n_e . This reduction is evident for

$n_{ni}/n_e > 10$ and it can be used as a proof for negative ion presence and to calculate n_{ni} . However, this is not the case for $n_{ni}/n_e < 10$ where additional diagnostics methods are needed to prove the negative ion presence. One possibility is laser induced photo-detachment where $I_p(V_{pi})$ is measured with and without laser irradiation.¹⁸⁴ However, additional ports for proper laser injection are not always available and the method is rather expensive. So alternative methods for negative ion detection are needed.

In this context, the results presented in Fig. 2.16 point at the possibility to use the etching patterns by discrete and modal focused ions on small and biased electrodes as sheath-lens probes for negative ion detection in reactive plasmas. This possibility was investigated in ES10. However, one should note that the understanding of the fine structure of the rear-side ion kinetics was not completely understood at that time (Figs. 2.8 and 2.9).

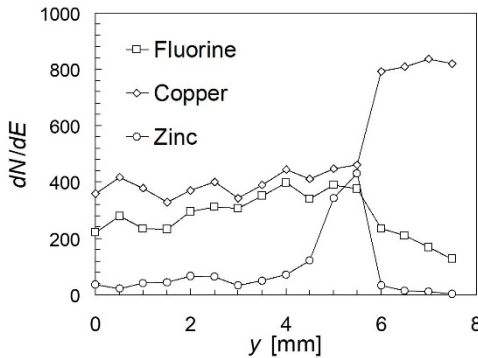


Fig. 3.8 Reproduced with permission from ES10 © 2004 American Institute of Physics Publishing LLC. Atomic composition in the median plane for the sample presented in Fig. 3.7 (d).

To prove the negative ion presence for $n_{ni}/n_e < 20$ by developing the discrete and modal focusing effects one needs to consider the large heat flux transported by electrons. The proposed solution was to provide water cooling to the surface exposed to plasma. Alternatively, one could aim to significantly reduce the exposure time. This approach was implemented by covering the surface with a conductive thin film that

could help to visualize the focusing patterns on a time interval below 5 min.

Fig. 3.7 presents disk and square electrodes with and without water cooling or a thin film of copper (below 30 nm) deposited on the surface exposed to plasma in the following conditions: (a) Ar/SF₆ plasma, $V_0=250$ V, $n_{ni}/n_e=46$, for

2 min, (b) O₂ plasma, $V_o=100$ V, $n_{ni}/n_e=7$, for 20 min, unknown n_{ni}/n_e , (c) Ar/SF₆ plasma, $V_o=250$ V, $n_{ni}/n_e=46$, for 15 min, (d) cooled surface, Ar/SF₆ plasma, $V_o=200$ V, $n_{ni}/n_e=46$, for 15 min, (e) cooled surface O₂ plasma, $V_o=200$ V, unknown n_{ni}/n_e for 20 min, (f) clean surface Ar/SF₆ plasma, $n_{ni}/n_e=46$, $V_o=300$ V for 5 min. The negative ion focusing is evident and expected in Fig. 3.7 (a) due to the large n_{ni}/n_e (>46). However, the electron flux is very large for the

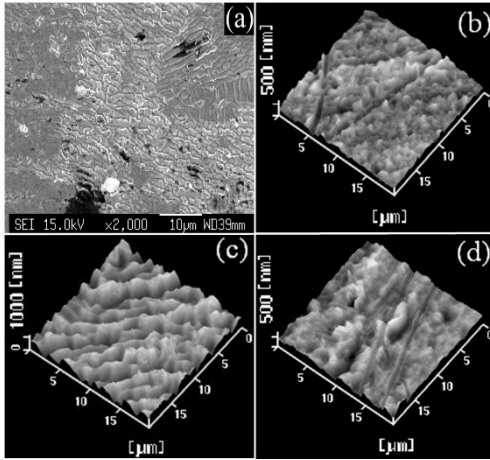


Fig. 3.9 Reproduced with permission from ES10 © 2004 American Institute of Physics Publishing LLC. (a) SEM and (b), (c) and (d) AFM images at locations (A), (1), (2) and (3), from Fig. 3.7, respectively

sample presented in Fig. 3.7 (b) and this could cause possible sheath distortion. Yet, the discrete focusing is very clear and this fact can be used to support the probe measurement from the point of view of negative ion detection. Fig. 3.7 (c) shows the ability to visualize the discrete focusing by negative ions in only 30 sec when having the Cu thin film deposited on the surface. The exposure time is too short to remove the thin film, but the location dependent ion dose changed the surface

color. In fig 3.7 (d) the Langmuir was not able measure n_{ni}/n_e , however, the cooled square electrode shows a clear pattern by discrete focusing of negative ions. This time, the 15 min exposure time was enough to modify the surface composition as presented in Fig. 3.8 where the median atomic composition is presented. Consequently, Cu is dominant on the passive surface while no F is detected since the F ions are not reaching that part of the electrode surface. The high current density at the location of discrete focusing reveals the presence of Zn as the result of local sputtering of the deposited thin film. Due to the very large difference in mass between negative ions and electrons it is expected that only negative ions will induce

sputtering on the electrode surface. This can further support the possibility to differentiate between electrons and negative ions. For this purpose, surface investigation was performed by SEM at location indicated with (A) in Fig. 3.7 (f) and with AFM at locations (1), (2) and (3), respectively. The results are presented in Fig. 3.9 and exhibit clear evidence of localized ion sputtering at the corner indicated with (A) and also location (2). Location (1) corresponds to the passive surface, with no impact and consequently no sputtering (Fig. 3.9 (b)). Since the gold surface was mirror-polished, one can see some polishing traces. While location (2) is intensively sputtered by discrete ion focusing, the polishing traces were removed by sputtering. However, location (3) corresponds to the active surface but with less sputtering, so that, one can see both surface roughness promoted by sputtering but also yet visible polishing traces.

So far, it has been shown that discrete focusing can be used to certify the negative ion presence for $n_{ni}/n_e < 20$. The next point of interest will be to evaluate n_{ni} . For this purpose, one needs to know the radial distribution of negative ion current density for a disk electrode, plasma density, the incidence angle, the sputtering yield as well as the ion and radical species. This complex information needs to be combined with the measured the depth profile.

3.3 Ion beam extraction

Ion extraction from plasma is one of the main approaches for ion source technology.^{185–187} While noble gases are widely used for generic applications such as ion beam sputtering or ion beam etching, reactive gases are opening a large range of new applications, including ion implantation, ion assisted nanofabrication and synthesis of advanced functional materials. By far, electropositive plasma discharges are employed for positive ions generation. However, recent concerns regarding surface charging and highly complex materials led to a significant interest in negative ion sources for direct applications or as an intermediary step for realizing neutral beam sources. For

example, Fig. 3.10 presents (a) the high-aspect-ratio reactive ion etching process and (b) the positive charge accumulation at the end of the trench that

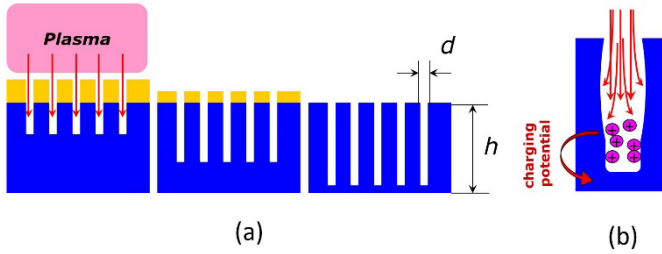


Fig. 3.10 (a) High aspect etching by positive ions and (b) positive charge accumulation at the end of the trench.

builds up a charging potential. This charge accumulation deflects the trajectories of incoming ions, affecting the etching profile and potentially inducing gate defects in memory devices.^{6,62,63} When negative ions impact the

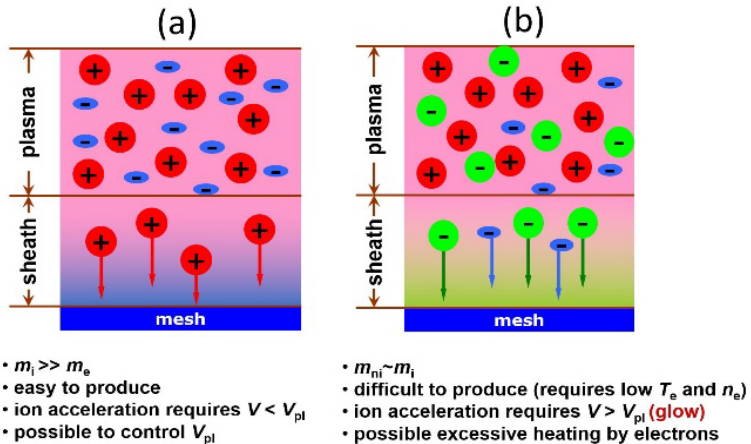


Fig. 3.11 (a) electropositive versus (b) electronegative plasma discharges.

wafer, the surface becomes positive due to electron emission, and consequently reduces the possible buildup of negative charge. However, there are additional demands on plasma sources when aiming at negative ion

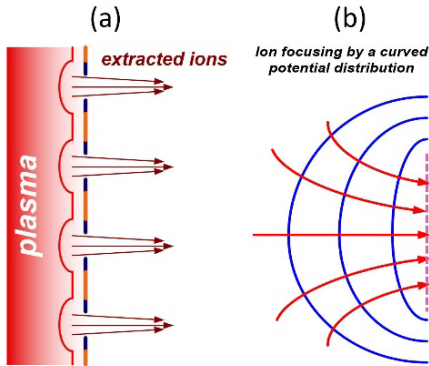


Fig. 3.12 (a) Ion extraction through a mesh or perforated electrode (b) ion beam focusing by a plasma-lens.

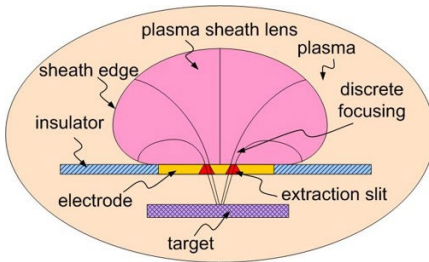


Fig. 3.13 Schematic of ion beam extraction by discrete focusing effect in a 3D plasma-sheath-lens.

extraction as illustrated in Fig. 3.11 where (a) electropositive and (b) electronegative discharges are presented with some key aspects. The large difference in mass between positive and negative charges has direct consequences on electropositive plasma properties. Such discharges are easier to produce and V_{pl} can be elevated to large voltages with respect to ground, thus providing significant energy gain for positive ions. By contrast, electronegative discharges require lower plasma densities (to prevent recombination) and a large fraction of low-energy electrons for negative ion formation. Moreover, as presented in section 2.2, it is not possible to elevate V_{pl} and the existence of a high fraction of electrons could ignite an anodic-glow-discharge. Once generated in plasma, the ions are typically

extracted with a system of meshes or perforated electrodes. To reduce plasma disturbance the first mesh, facing the plasma, is biased at V_{pl} or is kept at floating potential, V_f . Additional ion optics elements are then used to accelerate the beam and control the ion spread (angular distribution). This principle is illustrated in Fig. 3. 12 (a). It is important mentioning that curved

potential distributions, occurring over a large spatial distribution within a plasma discharge, can be used to influence (focus or defocus) high energy ion beams by a concept named plasma-lens. This principle is illustrated schematically in Fig. 3.12 (b).

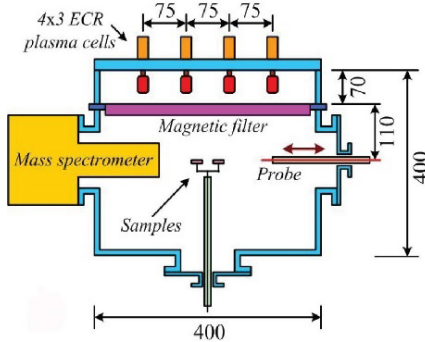


Fig. 3.14 Reproduced with permission from ES12 © 2012 American Institute of Physics Publishing LLC. Schematic of multi-dipolar ECR plasma source.

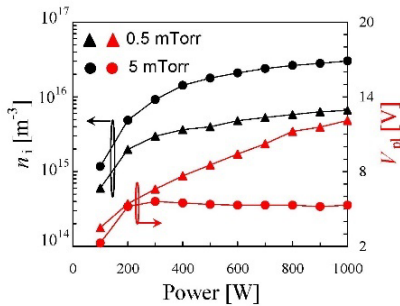


Fig. 3.15 Reproduced with permission from ES12 © 2012 American Institute of Physics Publishing LLC. Plasma density and plasma potential as function of discharge power.

In the presented context, a relevant question was if the discrete and modal focusing effects could provide new ways to extract positive or negative ion beams. The research conducted to answer this challenge is included in ES13, ES3 from the point of view of ion beam extraction and in ES12 concerning a suitable plasma source for generating both positive and negative ions.

The proposed concept for ion beam extraction by discrete ion focusing effect within a 3D plasma-sheath-lens is presented schematically in Fig. 3.13. An electrode-insulator interface is used to produce a curved potential distribution exhibiting discrete focusing. The ions collected from a large solid angle at the sheath edge are focused at a certain location by adjusting the plasma density and the electrode bias such as the ions are passing through a slit or mesh to reach the surface/target to be etched,

adjusting the plasma density and the electrode bias such as the ions are passing through a slit or mesh to reach the surface/target to be etched,

sputtered or implanted. This configuration is decoupling the plasma and the substrate, providing for example the possibility of tilting, or translating the

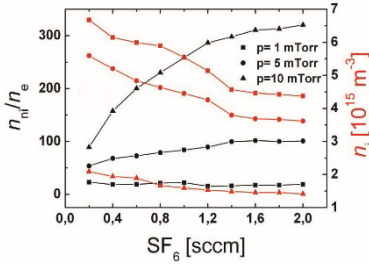


Fig. 3.16 Reproduced with permission from ES12 © 2012 American Institute of Physics Publishing LLC. Negative ion to electron density ratio and plasma density as a function of SF₆ flow at three different pressures.

substrate without affecting the 3D plasma-sheath-lens shape. Moreover, the substrate can be placed in the proximity of the extraction slit or at a large distance that can accommodate additional ion beam optics. To use this approach, one needs a plasma source having the following properties: i) stable operation at low pressure without mod jumps or large plasma potential variations; ii) tunable chemistry as to generate positive and/or negative ions; iii) easy scalable with a high degree of

uniformity.

The choice for this purpose was to use multi-dipolar electron-cyclotron-resonance (ECR) plasma cells driven in microwave at 2.45 GHz^{188–190} that were placed in a 3×4 matrix configuration at the top of a rectangular vacuum chamber as presented in Fig. 3.14. A magnetic filter was used to reduce T_e for promoting the formation of a large fraction of negative ions when operated in electronegative mode. Langmuir probes and mass spectrometry were used for plasma diagnostics.¹⁹¹ In Ar gas the discharge could be operated even at 0.5 mTorr, a pressure that ensures a large size collisionless 3D plasma-sheath-lens, without mode jumps in a power range up to 1000 W while reaching a plasma density above $3 \times 10^{15} \text{ m}^{-3}$ as presented in Fig. 3.15, where n_i and V_{pi} are presented as function of discharge power for 0.5 and 5 mTorr, respectively. At 5 mTorr, n_i reached above $2 \times 10^{16} \text{ m}^{-3}$ at 1000 W, making these conditions optimal for positive ion extraction. When operated in Ar/SF₆ gas mixture, the n_{ni}/n_e could reach 300 for 500 W power, 10 mTorr, 1 sccm Ar and 2 sccm SF₆ as presented in Fig. 3.16 where n_{ni}/n_e and n_i are presented for different SF₆ flows. One can also see that a higher T_e at 1 mTorr reduces n_{ni}/n_e

to less than 20 due to lower probability for electron attachment. The strong T_e dependence on pressure also affects plasma chemistry, with the possibility to extract more than one species of negative ions or in purpose to set the parameters for a preferential extraction of, for example, only F^- .

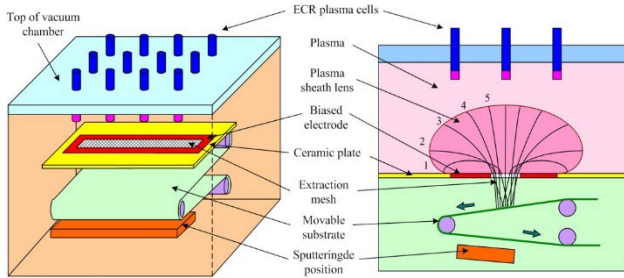


Fig. 3.17 Reproduced with permission from ES3 © 2012, the Institute of Physics Publishing Ltd. Ribbon-like extraction of ions by discrete ion focusing effect using a rectangular electrode with potential application for surface treatment in a roll-to-roll configuration.

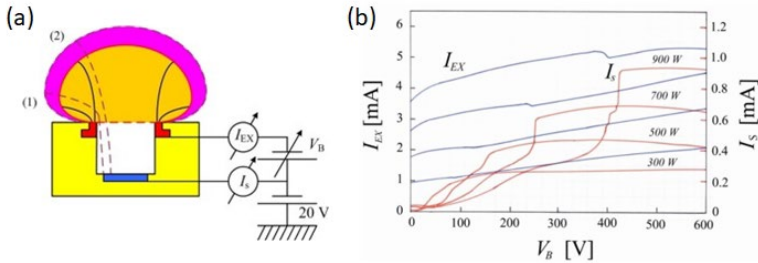


Fig. 3.18 (a) Schematic cross section of plasma-sheath-lens, extraction electrode, insulator, and the ion-collecting substrate. (b) The extraction electrode and substrate currents as a function of electrode bias for different discharge powers.

Once having the proper plasma source, the ion beam extraction including the surface exposure can be organized as presented in Fig. 3.17, that presents schematically a ribbon-like extraction for treating a moving substrate in a roll-to-roll configuration.

To test the operation principle, a 100 mm long extraction zone was created with a cross section as presented in Fig. 3.18 (a) where the electrode is presented in red and the ceramic insulator in yellow. The extraction region was a mesh. The sample was placed below at 10 mm distance. The thickness of the plasma-sheath-lens was controlled by the dc bias, V_B , while measuring the extraction electrode current, I_{EX} , and the substrate current, I_S . The $I_{EX}(V_B)$ and $I_S(V_B)$ for different discharge powers in Ar gas are presented in Fig. 3.18 (b). One can easily notice the decrease of I_{EX} and I_S increase at very correlated locations depending on V_B . For constant discharge power, at low V_B the sheath is thin, the discrete focusing is localized on the extraction electrode and I_S is small. The sheath expands by increasing V_B and consequently, the location of discrete focusing is moving inwards eventually reaching the mesh. At that location, I_S increase at the expense of I_{EX} decreasing. This transition needs higher V_B for higher discharge power as the sheath thickness decreases when increasing plasma density. The ability to use the extracted ion beam for sputtering, etching and ion implantation is under consideration as well as regarding negative ion beam extraction. The experimental setup available for

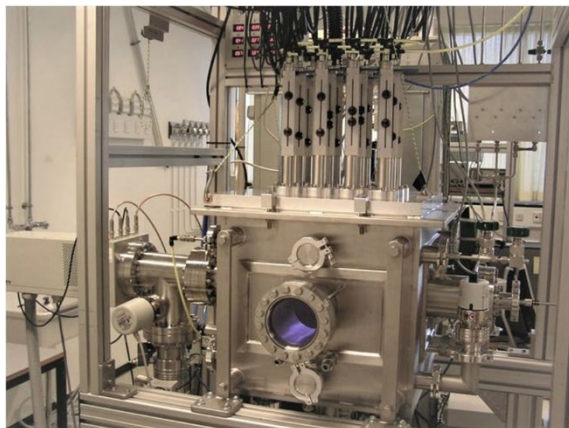


Fig. 3.19 Multi-dipolar plasma source with 12 ECR plasma cells, distributed in a matrix configuration of 3×4, driven at 2.45 GHz.

these investigations is presented in Fig. 3.19, where one can see the ECR

plasma cells with additional plasma diagnostics by mass spectrometry, optical emission spectroscopy and electrostatic probes.

3.4 Mass separation

Mass selection is essential in various methods for analytical characterization and instrumentation, surface induced processes, nanotechnology, and nuclear waste management.^{192–198} The theoretical possibility to use modal and discrete ion focusing effects for mass section was addressed in ES14. While the ion kinetics predicted in Fig. 2.19 was experimentally demonstrated, there are challenges related to magnetized plasma that need to be solved. Therefore, the effort to prove this possibility is ongoing. A 3D plasma-sheath-lens without magnetic field is a kinetic energy analyzer.

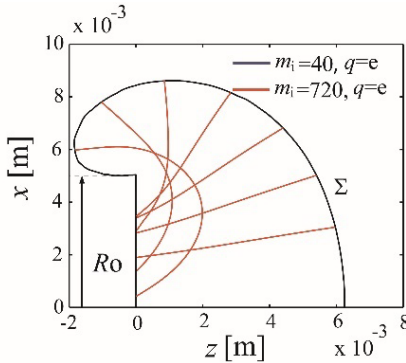


Fig. 3.20 Reproduced with permission from ES3 © 2012, the Institute of Physics Publishing Ltd. Trajectories of Ar and C₆₀ ions for a disk electrode of 5 mm in diameter ($V_0=-150$ V, $n_0=10^{15}$ m⁻³ and $T_e=1.5$ eV).

However, ions with different mass will exhibit similar trajectories but with different time of flight. This situation is presented in Fig. 3.20 where several trajectories are calculated for Ar ions in blue and C₆₀ ions in red ($R_0=5$ mm, $V_0=-150$ V, $n_0=10^{15}$ m⁻³ and $T_e=1.5$ eV). Despite the very large difference in mass the trajectories overlap. The presence of a magnetic field perpendicular to the surface twists the ion trajectories and forms an additional passive surface as presented in Figs.

2.18 (d) and 2.19 (a) and (b). The radius of this passive surface is mass dependent so that one should expect an overlap of several concentric circles for a multi-ion species plasma. For example, having the impact locations (see Fig. 2.19) for ions of different mass, one can calculate the radial distribution

of ion accumulation. This calculation is presented in Fig. 3.21 for a number of

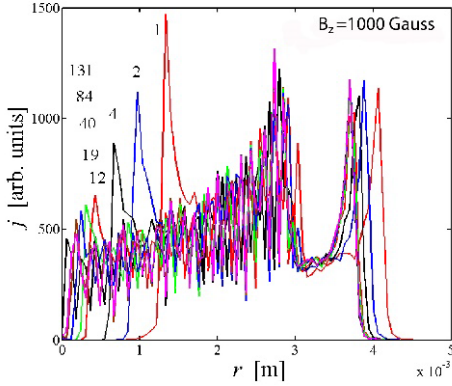


Fig. 3.21 Reproduced from ES14. Radial distribution of various ion accumulation for a disk electrode ($B_z=1000$ Gauss, $R_0=5$ mm, $V_0=-150$ V, $n_0=10^{15}$ m $^{-3}$ and $T_e=1.5$ eV).

relevant ions (H, H₂, He, C, F, Ar, Kr and Xe) for $B_z=1000$ Gauss, $R_0=5$ mm, $V_0=-150$ V, $n_0=10^{15}$ m $^{-3}$ and $T_e=1.5$ eV. Following the H⁺ distribution (in red) one can see the passive surface for $4.25 < r < 5$ mm, the high current density for $r=4.1$ mm corresponding to the discrete focusing, and a sharper peak for $r=1.45$ mm corresponding to the additional passive surface formation due to ion trajectory twisting by the

magnetic field. While the discrete focusing peaks are less mass sensitive (less

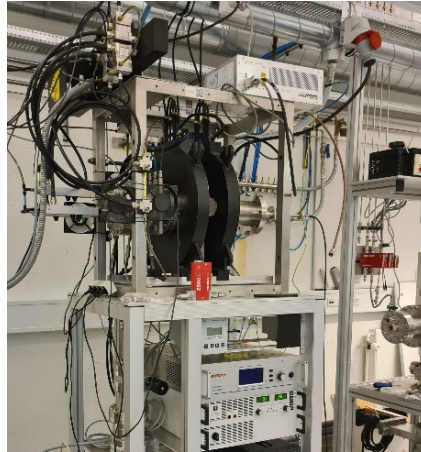


Fig. 3.22 Experimental setup for investigating 3D plasma-sheath-lenses including three ECR plasma cells and two magnetic coils able to produce a magnetic field of about 700 Gauss.

curved trajectories) the peaks formed by modal ions exhibit measurable locations. A dedicated plasma source was built (presented in Fig. 3.22) to investigate the possibility of mass selection in magnetized 3D plasma-sheath-lenses.

Experiments have been performed in various gas mixtures (He/Ar, Ar/SF₆, CF₄, Ar/Xe, O₂/Xe) and $B_z < 550$ Gauss with disk and square electrodes of different dimensions. However, the results were inconclusive regarding the possibility to identify with certitude concentric rings corresponding to ions of different mass.

4. Negative ion focusing during magnetron sputtering

The chapters above included scientific evidence supporting the discovered discrete and modal focusing effects, associated with the pioneered concept of 3D plasma-sheath-lenses. Having the definitions established and numerical simulations in very good qualitative agreement with experimental results one could ask if the concept of 3D plasma-sheath-lenses is also relevant in other plasma-based processes for nanofabrication. This chapter answers this question by presenting the case of negative ions focusing by a 3D plasma-sheath-lens in magnetron sputtering discharges. Physical vapor deposition is one of the main methods used for thin film deposition spanning from simple metallic films to advanced functional materials for various devices and sensors.^{133–135,199} The initial approach was to bias the target negatively so that a large flux of accelerated ions from plasma was removing the material to be deposited on the substrate. Later, to improve the rather low sputtering rate, permanent magnets were placed behind the target such as to form a high-density plasma in the proximity of target/cathode. For a disk target this dense plasma exhibits the shape of a torus. This configuration is named magnetron

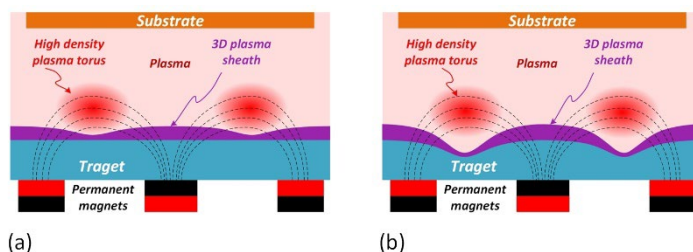


Fig. 4.1 (a) Schematic cross section for a new magnetron sputtering target including the nonuniform sheath structure, (b) eroded magnetron sputtering target.

sputtering and a schematical cross section is presented in Fig. 4.1 (a). The magnetic field increases the collision probability because electrons are forced to gyrate along the field lines. The negative bias applied to the target/cathode repels the electrons and forms a positive sheath adjacent to the surface. For a new sputtering target the surface is flat. However, due to the plasma torus, the sheath thickness will be lower at that location. The nonuniform ion flux

will erode the target preferentially, thus forming what is defined as the erosion track. A used sputtering target is presented in Fig. 4.1 (b) and shows the sheath molding over the surface with an accentuated 3D profile with respect to a new target. The positive ion focusing by this sheath structure is obvious. However, the effect on the substrate is limited since target tilting, substrate rotation and setting adequate target to substrate distances can be used to compensate this problem. Yet, there are situations where the 3D plasma-sheath-lens molding over a sputtering target has higher implications. This case was investigated in ES15, ES16, ES17, ES18 and ES 19 and the main results are summarized in this dedicated chapter.

4.1 Metal oxide thin film growth assisted by energetic negative ions

Metal oxide thin films exhibit semiconducting and optoelectronic properties making them suitable for thin film transistors,^{200–205} transparent conducting electrodes,^{206,207} and various sensors.^{208,209} Metal doping can further tune their properties, as example ZnO, that becomes conductive by doping with Al.²¹⁰ Moreover, additional film properties tuning can be achieved by operating the magnetron discharge in different modes (dc, pulsed, medium-frequency, radiofrequency, or high-power impulse).¹³⁴ For all these modes, oxygen gas needs to be present in the target, the gas mixture or both. Since oxygen is an electronegative gas, it will form oxygen negative ions in the presence of low-energy electrons. A schematical cross section for a magnetron discharge using an aluminum doped zinc oxide (AZO) target is presented in Fig. 4.2, where the 3D plasma-sheath is presented in purple and the plasma torus in red. Positive ions accelerated in the sheath strike the surface and remove target material at atomic level. Moreover, the positive ion bombardment is also releasing secondary electrons at the target surface. This creates favorable conditions for oxygen atoms to attach low-energy electrons and consequently form negative ions that will see an accelerating bias towards the substrate.^{211–213} The accelerating bias depends on the operation mode and can be a couple of hundred volts for dc and typically lower for radiofrequency (RF) discharges for the same power density applied on the target. Oxygen negative ions can also be formed in plasma volume.

However, their energy gain is limited. This implies that the thin film growth will be assisted by energetic negative ions. For the given structure of the magnetron discharge, including the plasma torus, the erosion track, and the 3D structure of the plasma-sheath, it is expected that the negative ion flux

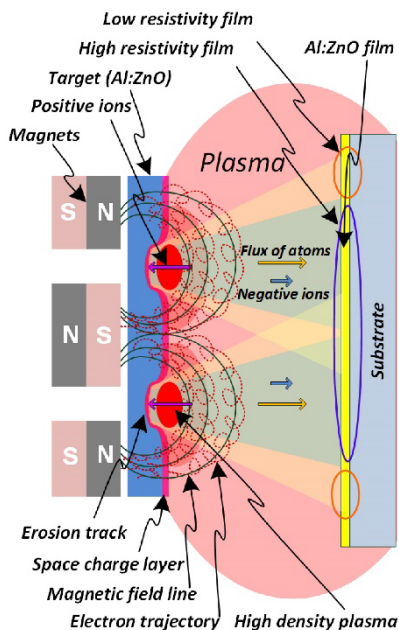


Fig. 4.2 Reprinted with permission from ES19 © 2022, The Royal Society of Chemistry. Schematic illustration of magnetron sputtering including the negative ion flux assisting the thin film growth.

will be focused to certain locations on the substrate, mirroring the erosion track. At the same time, the substrate edge is less exposed to energetic negative ions. AZO thin films have been investigated since 80's with the aim of replacing Indium Tin Oxide (ITO), one of the most used transparent conducting oxide (TCO).^{202,214,215} ITO has very good opto-electronic properties, however, Indium is an expensive and resource limited material. The figure of merit for TCO thin films depends on transmittance and resistivity. While the transmittance of AZO is above 85%, the resistivity was reported to exhibit a spatial distribution over the substrate correlated with the erosion

track.²¹⁶ The O^- formation have been reported by several groups,^{211,212} and Ellmer and his collaborators measured the O^- energy distribution for dc, RF at 13.56 MHz and RF at 27.12 MHz and also the O^- radial distribution over the sample substrate and find a very good correlation with AZO thin film resistivity.^{217,218} Dc magnetron exhibited O^- energies reaching 500 eV and much lower energies were measured for 13.56 MHz and 27.12 MHz respectively. While the relation between the erosion track, the O^- formation

and the resistivity profile over the sample was supported with convincing experimental results, the effective role of O^- during the films growth was not known.

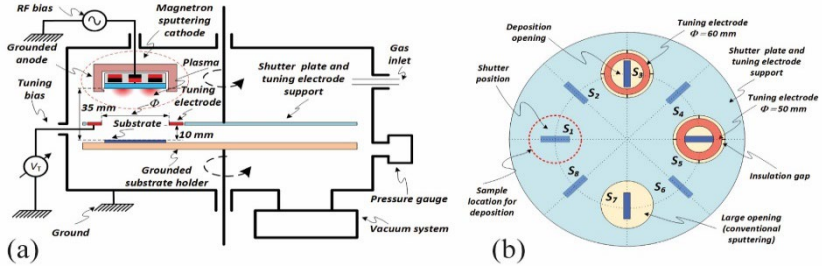


Fig. 4.3 Reprinted with permission from ES17 © 2020, Elsevier B.V. (a) Schematic of magnetron sputtering system including the sputtering head and the substrate, (b) details of the multipurpose rotatable shutter.

To answer this question, a set of experiments were performed using the setup presented in Fig. 4.3, where in (a) the sputtering cathode/target is placed in vacuum chamber with a rotatable substrate stage allowing 8 samples to be deposited at finely tuned deposition conditions. A multipurpose shutter (presented in Fig. 4.3 (b)) was used to prevent thin film deposition during the tuning. Soda lime glass samples of 50 mm in length, 5 mm in width and 0.5 mm in thickness have been used as substrates. The target was 2 inch in diameter and made of ZnO/Al_2O_3 , 98/2 wt% (Kurt Lesker, USA). The sheet resistance, film thickness and transmittance were measured over the sample with a spatial resolution of 2 mm. The film resistivity was calculated from sheet resistance and film thickness, and the transmittance spectra were used to measure the averaged transmittance (400 nm to 700 nm) and band gap. The spatial distribution of (a) sheet resistance, (b) film thickness, (c) averaged transmittance and (d) band gap for different pressures are presented in Fig. 4.4 (20 W RF power and 35 mm target to substrate distance). Despite of very small changes in pressure, the sheet resistance profiles exhibit very different profiles, with a central peak at 1.4 mTorr that vanishes at 3 mTorr, followed by the emergence of two new peaks for 6 and 9 mTorr that are correlated with the erosion track. Moreover, the sheet resistance shows very large variations within a short span on the sample surface, for example, a decay of more than two orders of magnitude from $r=10$ mm to $r=20$ mm at 9 mTorr. The film

thickness presents a central decrease only at 1.4 mTorr, and typical parabolic profiles for higher pressures, with visible shoulders at 6 and 9 mTorr correlated with the erosion track. The averaged transmittance (see Fig. 4.4 (c)) presents a clear correlation with the erosion track only at 3 mTorr. However, all values are above 87%. Larger variations, also correlated with the

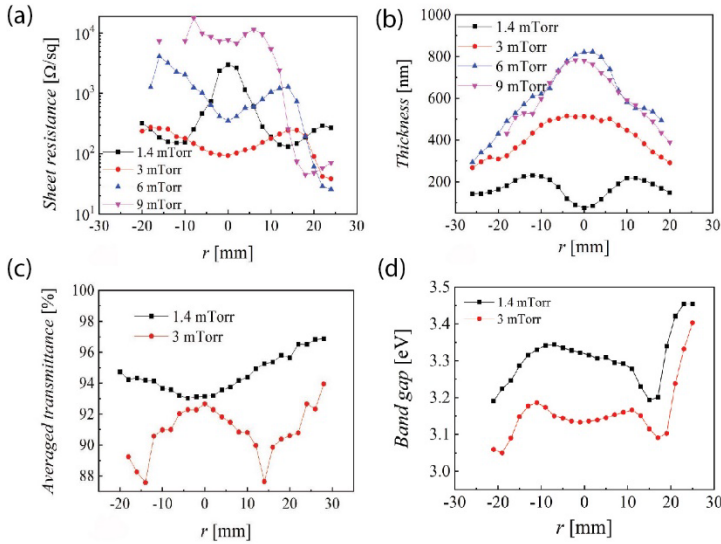


Fig. 4.4 Reprinted with permission from ES15 © 2020, MDPI. (a) Sheet resistance, (b) thickness, (c) averaged transmittance and (g) band gap for AZO thin films deposited at 20 RF power and 35 mm target to substrate distance.

erosion track, are measured for band gap, with a significant increase at the sample edge ($r > 20$ mm).

To understand the measurements presented in Fig. 4.4 a detailed investigation of plasma parameters was performed in ES16 with the aim of understanding if the peaks correlated with the erosion track are the result of plasma density profile, as well as to understand the central peak at 1.4 mTorr that vanishes so fast at 3 mTorr.

Diagnostics of plasma parameters during magnetron sputtering with conventional Langmuir probes is complicated due to surface contamination issues and spatially resolved optical methods are extremely complex.^{177,181} In this context, our choice was to use a dual thermal-electrostatic probe as presented in Fig. 4.5. Having a metal electrode/probe inserted into plasma

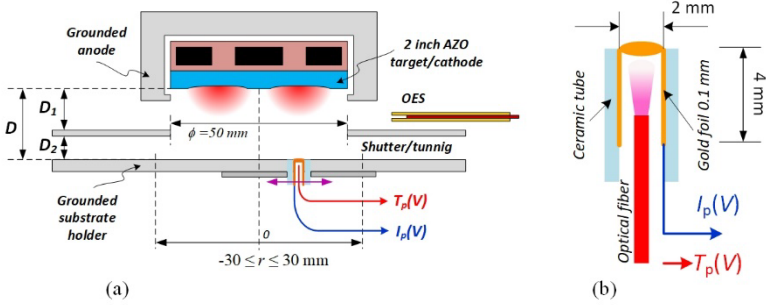


Fig. 4.5 Reprinted with permission from ES16 © 2021, IOP Publishing Ltd. (a) Schematic representation of the dual probe diagnostics including the sputtering cathode and the grounded substrate holder, (b) technical details of the dual probe.

one can measure the probe current, I_p , as a function of probe bias, V . For $V \ll V_{pi}$ the probe collects only positive ions and under certain assumptions (orbital or radial motion of ions) it is possible to obtain n_i from $I_i(V)$, where I_i is the collected ion current. For $V < V_{pi}$ the probe collects both ions and electrons, and for $V > V_{pi}$ almost only electrons since $I_i(V > V_{pi}) \rightarrow 0$ within a couple of volts. Of particular interest is the region of $I_p(V)$ for $V \sim V_{pi}$ that allows one to measure V_{pi} as the maximum value of $I_p'(V)$, where I_p' is the first derivative of $I_p(V)$ (see ES11 for details). Since probe contamination significantly affects $I_p(V_{pi})$, special precautions are needed to ensure a correct measurement. At the same time, for a fixed V , the charges reaching the probes establish a thermal equilibrium, resulting in a probe temperature T_p .^{180,219,220} It means that by swiping V one can also measure $T_p(V)$ with the same probe or even at the same time with $I_p(V)$. The experimental arrangement is presented in Fig. 4.5 (a) including the sputtering cathode, the shutter, and the movable stage, translating the dual probe at the same level

with the substrate holder. The technical details of the dual probe are presented in Fig. 4.5 (b). A gold foil (0.1 mm in thickness) was rounded to form a cylinder of 2 mm in diameter, the tip was then melted to form a hemisphere that was finally polished to a flat surface. The cylinder was electrically connected to measure $I_p(V)$ while an optical fiber, placed inside of the cylinder, was used to measure $T_p(V)$ based on the decay of the fluorescence

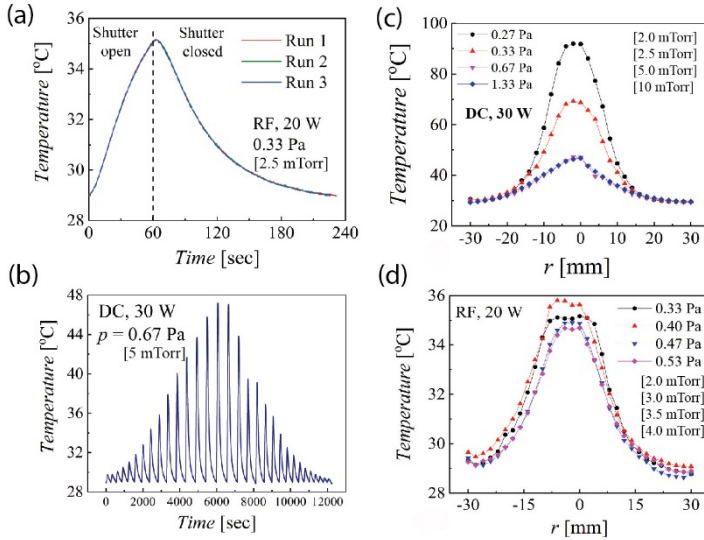


Fig. 4.6 Reprinted with permission from ES16 © 2021, IOP Publishing Ltd. (a) Three runs of shutter open-closed in RF at 20 W and 2.5 mTorr; (b) Spatial distributed profile in DC at 30 W and 5 mTorr; (c) Spatial distribution of temperature peaks for different pressures in DC at 30 W; (d) Spatial distribution of temperature peaks for different pressures in RF at 20 W.

signal after pulse excitation with violet radiation. The principle of operation as thermal probe is presented in Fig. 4.6 (a). The probe is kept at -200 V all time, to ensure positive ion collection at high enough energy as to remove by sputtering possible AZO deposition. The discharge is ignited (RF, 20 W, 2.5 mTorr) and the probe records 29°C with shutter, the shutter is then removed and T_p increases over a 60 sec exposure time, exhibiting a saturation tendency. By closing the shutter, T_p decays, and needs 180 sec to reach again the initial $T_p \sim 29^{\circ}\text{C}$. To test the reliability, three runs were repeated with a

delay of 10 min and almost identical profiles were obtained. This succession (shutter open-closed) was repeated by translating the probe in steps of 2 mm

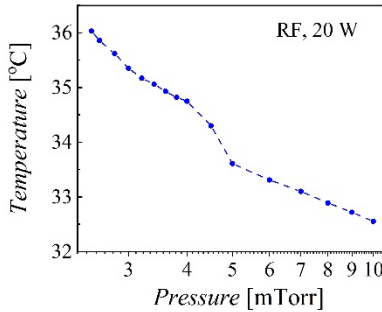


Fig. 4.7 Adapted with permission from ES16 © 2021, IOP Publishing Ltd. T_p as a function of pressure in RF discharge at 20 W.

with a step motor. A measured spatial profile is presented in Fig. 4.6 (b) for 30 W in DC operation mode and 5 mTorr discharge pressure. One can notice that the time interval between each step ensured T_p relaxation to the same value of about 29°C. Moreover, the peaks profile is symmetric, a fact that rules out the possibility of accumulated probe contamination over the rather long measurement time (12000 sec). The T_p peaks spatial

distribution is presented in Fig. 4.6 (c) for different pressures in DC at 30 W. T_p reached more than 90°C for $r=0$ mm at 2 mTorr with a steep decrease at the same location by increasing the pressure to 5 mTorr. However, a further pressure increase, to 10 mTorr, produced similar profiles. T_p profiles in RF are presented in Fig. 4.6 (d) and show significantly lower values for $r=0$ mm. Remarkably, all T_p profiles, in both DC and RF discharges are parabolic, with no correlation with the erosion track as observed for opto-electronic properties. The T_p as function of pressure in RF at 20 W and $r=0$ mm is presented in Fig. 4.7, and one can see a transition region at around 4 mTorr. For pressures below this value the plasma is in a plume-like mode, with a high re-sputtering rate at the center of the sample that reduces the film thickness as can be seen in Fig. 4.4 (b) at 1.4 mTorr. For higher pressures the discharge runs in the conventional magnetron mode with a parabolic profile for the film thickness.

4.2 Reducing the oxygen negative ion energy in RF discharges by controlling the dc self-bias

The results presented above sustain the assumption of a detrimental role of energetic oxygen negative ions focused by the 3D plasma-sheath structure on the optoelectronic properties of AZO thin films. This understanding suggests that one can lower the AZO thin film resistivity and improve uniformity by reducing the oxygen negative ions energy. Since the negative ions energy is controlled in an RF discharge by the dc self-bias, the point of action should be to reduce the self-bias, for example by improving the RF coupling. This approach was introduced in ES17 and is presented below.

To improve the RF coupling, a tuning electrode was placed in the space

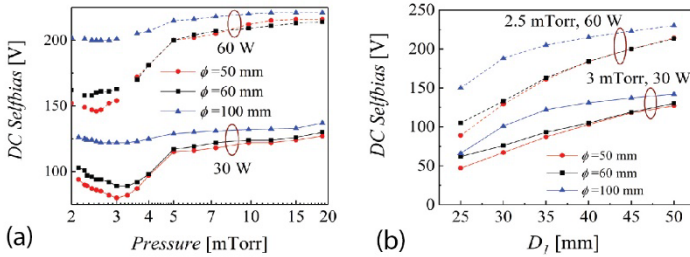


Fig. 4.8 Reprinted with permission from ES17 © 2020, Elsevier B.V. (a) DC selfbias as a function of pressure at 30 W and 60 W discharge power, for $\phi=50$, 60 and 100 mm, respectively. (b) DC selfbias as a function of D_1 for $\phi=50$, 60 and 100 mm and 2.5 mTorr and 60 W and 3 mTorr and 30 W.

between target/cathode and the grounded substrate holder as presented in red for S_3 and S_5 in Fig. 4.3 (b). The two circular rings, both with an outer diameter of 100 mm in diameter, and inner openings, ϕ , of 50 and 60 mm in diameter, respectively, were mounted on the large shutter plate. An additional opening of 100 mm in diameter was used as reference for the case without tuning. The rings could also be biased with a dc power supply at potential V_T . The main idea was to bring an additional surface close to the cathode/target while minimizing the interference with the sputtered material. Further tuning can be attained by adjusting D_2 (tuning electrode to

substrate distance) for a given D_1 (target to substrate distance). The DC selfbias as a function of pressure at 30 W and 60 W, respectively, is presented in Fig. 4.8 (a) for different ϕ , while the dependence on D_1 at 30 W and 3 mTorr

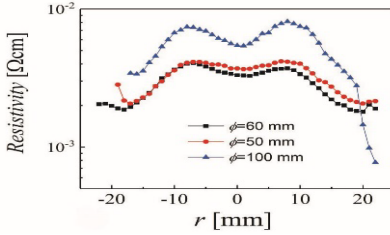


Fig. 4.9 Reprinted with permission from ES17 © 2020, Elsevier B.V. Resistivity profile for different ϕ , where $D_1=35$ mm, $D_2=10$ mm and 30

and 60 W and 2.5 mTorr, respectively, is presented in Fig. 4.8 (b). Remarkably, the 50 mm and 60 mm opening tuning electrodes were able to lower the dc selfbias with 50 V at 3 mTorr for both powers. It is also evident that lower power and short target to substrate distance are beneficial for keeping the selfbias below 75 V.

This result is consistent with a large number of reports suggesting low power, short target to substrate and moderate power as the most beneficial parameters for a high figure of merit (transmittance above 85% and resistivity below $5 \times 10^{-3} \Omega\text{cm}$) AZO thin films.^{217,221} It is also remarkable to see the role of tuning electrode in exhibiting a valley profile for DC selfbias variation with pressure, with minimum values around 3 mTorr as this region was identified

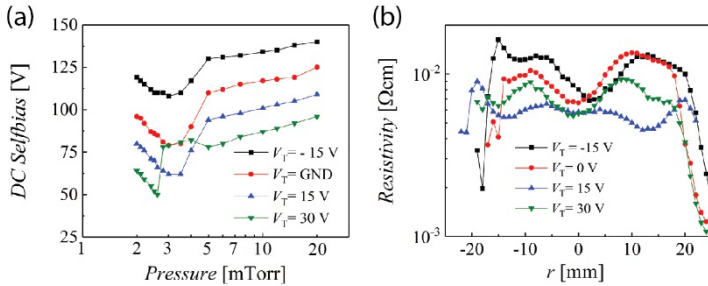


Fig. 4.10 Reprinted with permission from ES17 © 2020, Elsevier B.V. (a) DC selfbias as function of pressure for different V_t , (b) Resistivity profiles for different V_t .

to correspond to a transition from plume-like discharge to magnetron discharge (see Fig. 4.7). To verify the tuning electrode effectiveness to lower the AZO thin films resistivity, three samples have been deposited at 3 mTorr,

the pressure exhibiting the lowest DC selfbias, one for each of the openings: 50, 60 and 100 mm, respectively ($D_1=35$ mm, $D_2=10$ mm, and 30 W RF power). The measured resistivity is presented in Fig. 4.9 and shows a decreasing with a factor of 2 for both $\phi=50$ and 60 mm. As mentioned above, an additional tuning element is to change the V_T bias. The DC selfbias as a function of pressure for different V_T is presented in Fig. 4.10 (a) for 30 W RF power, $D_1=35$ mm, $D_2=10$ mm and $\phi=50$ mm. A negative $V_T(-15$ V) led to a larger selfbias, while $V_T=15$ V reduced it by about 15 V. Further increasing V_T to 30 V distorted the plasma, so that it was not an option. The impact of V_T on thin film resistivity is presented in Fig. 4.10 (b) where the spatial distribution is presented for five samples deposited at 3 mTorr discharge pressure and same parameters as for measurements presented in Fig. 4.10 (a). While $V_T=-15$ V and $V_T=0$ V resulted in almost similar profiles (note the slight shift of about 5 mm that is caused by samples misalignment), $V_T=15$ V produced the lowest and most uniform resistivity profile.

To test if the tuning electrode can be effective for other metal oxides than AZO, the DC selfbias as a function of pressure was also measured for gallium doped zinc oxide (GZO) and ITO (ES 18). The DC selfbias as function of pressure for AZO, GZO and ITO is presented in Fig. 4.11 (a) for 30 W, $D_1=35$

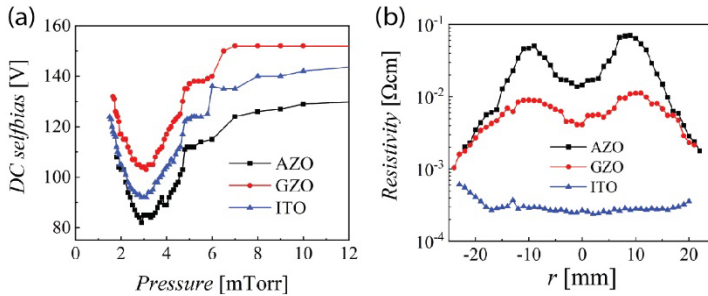


Fig. 4.11 Adapted with permission from ES18 © 2022, MDPI. (a) DC selfbias as function of pressure for AZO, GZO and ITO; (b) Resistivity as function of pressure for AZO, GAZO and ITO.

mm, $D_2=10$ mm and $\phi=50$ mm and shows that the tuning electrode has a similar effect for all three metal oxides. However, the resistivity profiles of

three samples measured for the same discharge parameters show very large differences between each material as presented in Fig. 4.11 (b). While AZO and GZO show higher resistivities correlated with the erosion track, the ITO profile is flat and exhibits most values below $3 \times 10^{-4} \Omega\text{cm}$.

4.3 Preferential sputtering by 3D focused negative ions

The above included results demonstrated the ability to reduce the detrimental role of oxygen negative ions by reducing their energy using a biased tuning electrode that can reduce the accelerating bias, namely the DC selfbias. However, the direct influence of energetic oxygen negative ions during the film growth is not known. To answer this question, a detailed analytical characterization of the deposited AZO thin films was needed. This investigation was covered in ES19 and the main findings are presented below.

Fig. 4.12 Presents, (a) the sheath resistance, (b) film thickness and (c) resistivity of a set of samples deposited at different pressures, for 30 W RF power and 35 mm target to substrate distance and grounded tuning electrode. The results are very close to those presented in Fig. 4.4 and have been deposited in purpose to be also used for analytical characterization. In brief, the sheet resistance at 2 mTorr exhibits a variation of almost two orders of magnitude, reaching nearly $10^4 \Omega/\text{sq}$ for $r=0$. This region corresponds to a significant reduction in film thickness, caused by re-sputtering. This behavior was associated with the plume-like discharge mode. By increasing the pressure to only 3 mTorr one can see a significant change in sheet resistance that decays from $10^4 \Omega/\text{sq}$ to $200 \Omega/\text{sq}$. The only parameter that changes significantly in this narrow pressure range is the DC selfbias that decreases steeply with almost 30 V as presented in Fig. 4.11 (a). The film thickness still shows lower values at the sample center, confirming a certain rate of resputtering. Further increasing the pressure to 4 mTorr reverses the sheet resistance profile (see red and blue profiles in Fig. 4.12 (a)), with lower values for $r=0$ mm, and also significant changes in the film thickness profile that now shows higher values for $r=0$ mm. For Fig. 4.11 (a) one can see that the DC selfbias now has an increasing trend after reaching the minimum value at 3

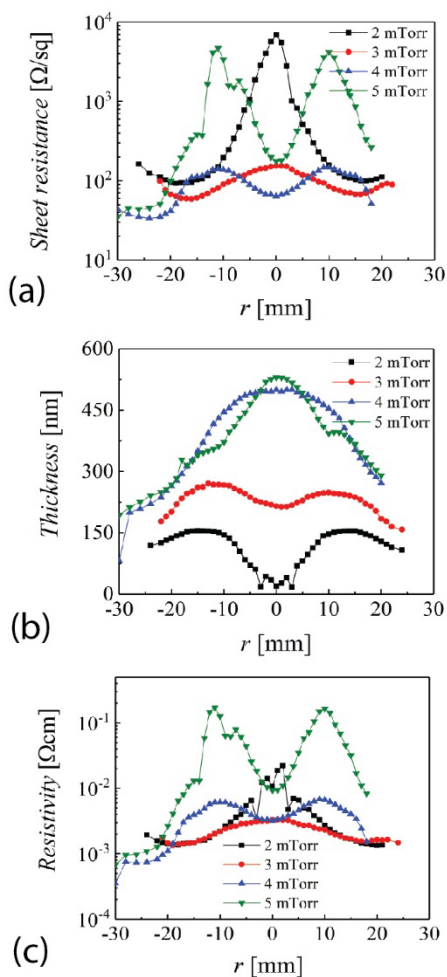


Fig. 4.12 Adapted with permission from ES19 © 2022, The Royal Society of Chemistry. Spatial distribution of (a) sheath resistance, (b) film thickness and (c) resistivity of AZO thin films deposited at 30 W RF power.

mTorr. The next step of pressure-increase to 5 mTorr exhibits a drastic change in sheath resistance with two peaks correlated with the erosion track and very low values for $r=0$ mm and even lower for $r < -20$ mm. Moreover, two shoulders are visible in the film thickness profile also correlated with the erosion track where the resistivity is with one order of magnitude higher than at the sample center or with respect to resistivity values at 4 mTorr for same location, $|r| \sim 12$ mm. One important observation is that the resistivity reached the $10^{-4} \Omega\text{cm}$ range only for $r < -20$ mm for 4 and 5 mTorr. The reach information included in Fig. 4.12, with very large variations for different pressures and spatial distributions exhibiting one order of magnitude changes within 10 mm span on the sample surface, offers an excellent context for analytical characterization. So far, various techniques

have been used to investigate AZO thin film properties, including x-ray diffraction (XRD),^{222–225} x-ray photoelectron spectroscopy (XPS),^{221,226,227} Raman spectroscopy,^{221,223} energy dispersive spectroscopy (EDS), scanning electron microscopy (SEM), and transmission electron microscopy (TEM). However, most of reported results are limited to certain regions on the

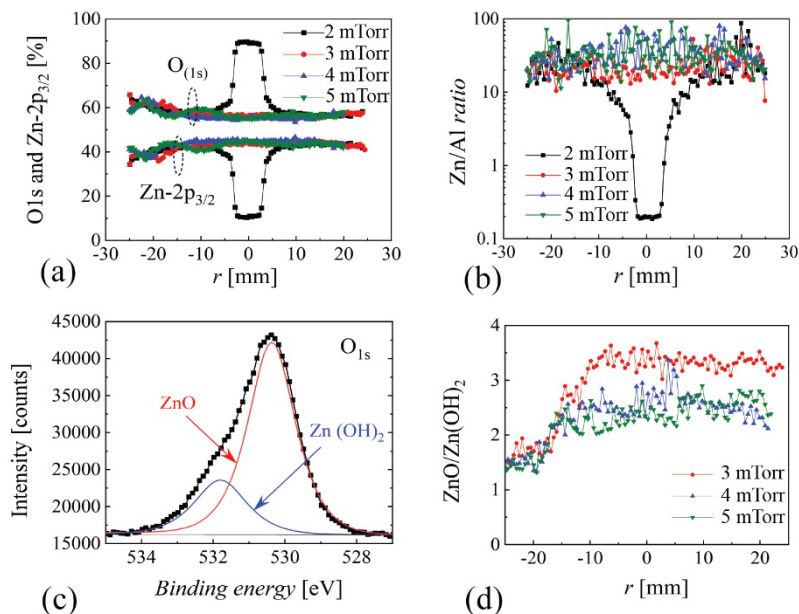


Fig. 4.13 Reproduced with permission from ES19 © 2022, The Royal Society of Chemistry. Spatial distributions of (a) O_{1s} and $Zn-2p_{3/2}$, (b) Zn/Al ratio for different pressures. (c) Deconvolution of O_{1s} peak in ZnO and $Zn(OH)_2$ contributions. (d) Spatial distribution of $ZnO/Zn(OH)_2$ at 3, 4 and 5 mTorr, respectively.

substrate, without taking advantage of high-spatial resolution for samples deposited at short target to substrate distances.

To address this issue, the same samples investigated in Fig. 4.12 have been used for XPS, XRD and time of flight secondary ion mass spectrometry (TOF-SIMS). Fig. 4.13 presents (a) the spatial distribution of O_{1s} and $Zn-2p_{3/2}$ peaks

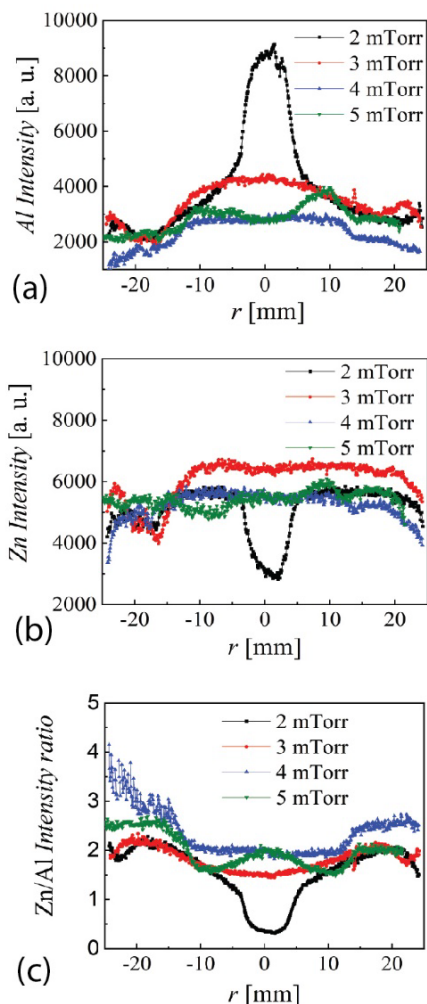


Fig. 4.14 Reproduced with permission from ES19 © 2022, The Royal Society of Chemistry. Spatial distribution of Al, Zn and Zn/Al ratio for different discharge pressures.

and Zn/Al intensity ratio for different pressures that exhibit a significant Zn depletion only at 2 mTorr, for the region corresponding to the high resputtering zone (see the film thickness profile at 2 mTorr in Fig. 4.12 (b) for $|r| < 5$ mm). However, all other profiles are quite flat, with no correlation with any of the profiles shown in Fig. 4.12 for 3, 4 and 5 mTorr. The deconvolution of the O_{1s} in three peaks corresponding to energies 530.15 ± 15 eV, $531.25 \text{ eV} \pm 0.25$ eV and 532.40 ± 0.15 eV was also unable to reveal additional information regarding the samples deposited at 3, 4 and 5 mTorr. Consequently, the O_{1s} peak was also deconvoluted on ZnO and $Zn(OH)_2$ as presented in Fig. 4.13 (c). The ZnO/ $Zn(OH)_2$ ratio is presented in Fig. 4.13 (d) and shows values below 2 at 4 and 5 mTorr where the lowest resistivity values have been measured with no particular distribution for $r > -10$ mm.

The spatial distributions of Al and Zn intensities by TOF-SIMS at different pressures for the same samples used to generate the data from Fig. 4.12 are presented in Fig. 4.14 (a) and (b), respectively, and the Zn/Al intensity ratio in Fig. 4.14 (c). Both Al and Zn profiles are showing certain spatial distributions, but no conclusive correlation can be made with resistivity except for 2 mTorr where one can see the same Zn depletion noted by XPS for $|r| < 5$ mm. However, The Zn/Al intensity ratio exhibits a remarkable correlation with the resistivity profile, with highest values (above 2.5) at locations corresponding to resistivity values below $10^{-3} \Omega\text{cm}$. To understand this result, one should consider the sputtering yields of Al and Zn by oxygen ions.²²⁸ It is presented

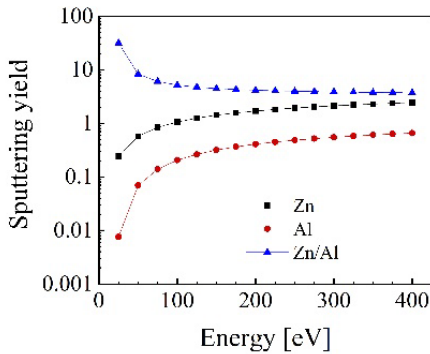


Fig. 4.15 Sputtering yield as a function of energy for Al, Zn and Zn/Al ratio by oxygen ions.

in Fig. 4.15 and reveals that Zn is preferentially sputtered against Al, with a factor larger than 6. Based on this fact, the strong decrease of Zn/Al ratio to below 1 for $|r| < 5$ mm and 2 mTorr corresponds to a strong depletion of Zn due to the collimated (plume-like discharge) and energetic oxygen negative ions, that are reaching the center of the sample. For 3 and 4 mTorr,

the DC selfbias decreases and consequently the negative ion energy decreases as well. This is reflected in more uniform Zn/Al profiles, with values around 2 for $|r| < 15$ and higher than 2 near to the edge of the substrate. At 5 mTorr, the DC selfbias rises again and the discharge is in magnetron sputtering mode with a high-density plasma torus providing a large flux of ions impinging on the target. It releases low-energy secondary electrons and atomic oxygen that forms a large flux of oxygen negative ions to be then accelerated by the 3D potential in the sheath to regions of the substrate correlated with the erosion track. This large flux of energetic oxygen negative

ions preferentially resputter Zn at locations corresponding to the erosion track, thus decreasing the Zn/Al ratio below 2 as presented in Fig. 4.14 (c).

To understand the influence of Zn depletion on the structural properties of the thin films four samples of 50×50 mm² were deposited at 3.5, 4, 4.5 and 5 mTorr respectively, for the same RF power and target to substrate distance as for samples presented in Fig. 4.12 (30 W and 35 mm). The 2D-XRD patterns for (100), (110) and (002) orientations are presented in Fig. 4.16 for a) 3.5 mTorr, b) 4 mTorr, c) 4.5 mTorr and d) 5 mTorr, respectively, where one can

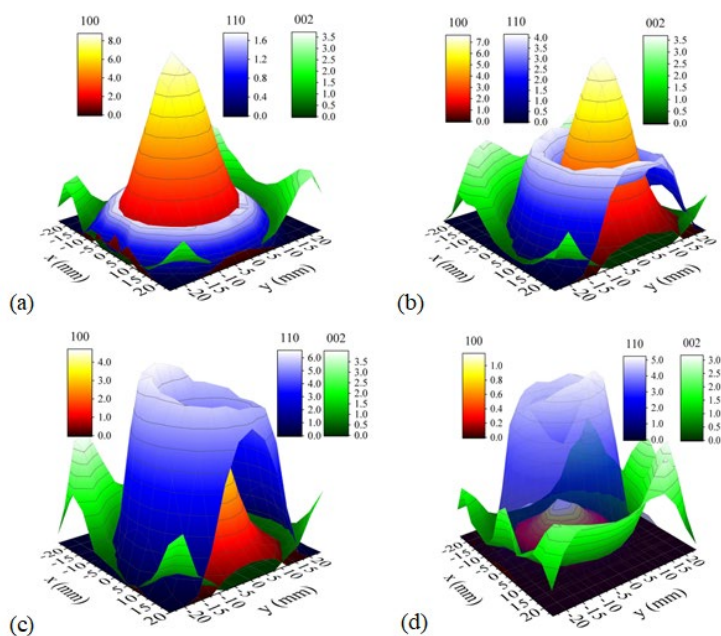


Fig. 4.16 Reproduced with permission from ES19 © 2022, The Royal Society of Chemistry. 2D-XRD patterns for (100), (110) and (002) orientations at (a) 3.5 mTorr, (b) 4 mTorr, (c) 4.5 mTorr, and (d) 5 mTorr, respectively.

see a remarkable correlation with results from Figs. 4. 12 and 4.14. At 3.5 mTorr it is still possible to see the influence of the plume-like discharge with a dominant (100) orientation at the center of the sample and a shallow (110)

contribution resampling the erosion track. A very slight increase in pressure (3.5 mTorr) reduces the selfbias, the plume-like mode is less accentuated with a rising contribution of the magnetron sputtering mode that enhances the 110 orientation. The further increase in pressure establishes the dominance of the magnetron sputtering mode with an accentuated (110) orientation. For all pressures the desired (002) orientation is dominant only at the edge of the substrate, region that is not reached by focused energetic oxygen negative ions. Despite very large spatial variations in resistivity, composition, and crystalline orientation, the AZO thin films exhibited averaged transmittance profiles above 85%. Obviously, one can improve the thin film uniformity by increasing the target to substrate distance or by rotating the substrate. However, all reach information included in Figs. 4.12, 4.14 and 4.16 will be lost, making extremely difficult to draw any relevant conclusions about the growth mechanism.

5. Conclusion and outlook

5.1 Conclusion

Two focusing effects have been discovered in relation to biased electrode-insulator interfaces immersed into plasma, namely the modal and discrete ion focusing effects. It was demonstrated that the focusing effects can manifest separately, depending on the shape of the electrode and the shape of the space charge surrounding the electrode-insulator interface. The concept of 3D plasma-sheath-lens was pioneered to define the possibility of tuning the plasma-presheath-sheath-electrode system for controlling in purpose the focusing effects. New definitions have been introduced to describe the focusing effects including passive surface, active surface, impact radius, modal lines, modal ring, modal spot and modal rays. A 3D simulation model was developed to predict the plasma-sheath-lens structure, calculate ion trajectories and ion impact locations on the electrode surface with a very good qualitative correlation with experimental results.

It was demonstrated that the modal and discrete ion focusing effects are also manifesting for negative sheaths dominated by negative ions. For this purpose, detailed investigations have been performed to understand basic properties of electronegative discharges, including the realization of an electron cyclotron resonance plasma source able to produce a stable electronegative discharge with a negative ion to electron density ratio above 300, where an electrode could be biased to hundreds of volts above plasma potential without igniting an anodic-glow discharge. Also, it was possible to demonstrate that a negative sheath is thicker than a positive sheath for similar plasma parameters and applied bias.

The magnetic field effect on ions kinetics with the 3D plasma-sheath-lenses was investigated by simulations. It predicted the formation of an additional passive surface at the center of disk electrodes due to twisting of ion trajectories. Additional results on this topic are available for publication.

Several applications exploiting the focusing effects have been introduced, including negative ion detection, controlling of ion flux and dose in plasma immersion ion implantation, extraction of positive and negative ion beams and mass separation. The concept of a ribbon-like ion beam source was introduced, and the extraction capability was tested. The ion beam extraction by discrete focusing presents several important advantages with respect to existing technologies. The substrate to be treated is decoupled from plasma. By controlling plasma chemistry, it is possible to tune the extracted ion species. The substrate can be placed in the proximity of the extraction zone and can be tilted or translated without affecting the ion beam. It was predicted that ion mass separation is feasible for a disk electrode of only 10 mm in diameter and 1000 Gauss magnetic field, applied perpendicular to the surface.

The 3D plasma-sheath-lens concept was extended by including the magnetron sputtering discharges for metal oxide thin film deposition where the 3D plasma-sheath formed adjacent to the sputtering target is focusing oxygen negative ions to a region on the substrate surface correlated with the erosion track. The effect of these energetic oxygen negative ions on structural properties of aluminum doped zinc oxide thin films was investigated and a method to reduce their detrimental role was proposed by using a tuning electrode. This context was then used to answer a question lasting for three decades related to the role of oxygen negative ions during the growth of aluminum doped zinc oxide thin films. Using high spatial resolution measurements for plasma properties, optoelectronic parameters, and analytical characterization it was possible to demonstrate that preferential Zn sputtering by focused energetic oxygen negative ions is the main reason causing high resistivity for AZO thin films at location on the substrate correlated with the erosion track.

5.2 Outlook

The very well-defined patterns revealed by modal and discrete ion focusing on disk and square biased electrodes are an excellent platform for investigating the 3D ion kinetics in plasma-presheath-sheath systems with the goal of being able to predict with high accuracy the impact location of an ion collected from plasma when reaching the surface. This should include the contribution of multi-ion species and presence of external magnetic fields on defining the plasma-sheath boundary. Moreover, the plasma-presheath-sheath system can be extended by including surface processes. In this way, the pattern resulted on the electrode surface (for example by etching) can be regarded as a fingerprint of the entire plasma-sheath-surface system. This endeavor requires significant progress in 3D plasma-sheath simulations. Nowadays, extensive work is devoted to simulating 3D magnetized discharges such as ion thrusters and magnetron sputtering discharges using particles in cell codes. However, it is difficult to extract parameters that can be easily compared with experiments in a quantitative way. In this context, magnetized 3D plasma-sheath-lenses, exhibiting modal and discrete focusing effects can be used to verify the simulation-codes accuracy by comparison with the easily measurable patterns on electrode surface. Once simulations will be able to predict with reasonable accuracy the ion kinetics, various customized 3D plasma-sheath-lenses can be designed to address charge manipulation, including time-dependent processes.

Modal and discrete focusing effects also open very exciting possibilities for plasma diagnostics, including weak electric field measurements in sheath structures with volumes below 1 cm^3 . It will have a significant impact on various low-pressure plasma-based processes (etching, ion implantation, sputtering) that need accurate monitoring. For example, the impact radius correlates directly with plasma density for a given electrode shape and applied bias.

Mass selected ion beams, controlled to reach precise locations and induce dedicated surface processes are of high importance for nanofabrication and in situ monitoring of micro- and nano device functionality. This can be easily achieved with magnetized 3D plasma-sheath-lenses and our effort to produce

experimental evidence of mass separation with small size electrodes is ongoing.

High current density ions sources with ribbon distribution are expected to have a significant impact on etching, sputtering and ion implantation processes used for nanofabrication of advance functional materials for nanoelectronics technology, energy devices and various sensors needed for internet of things devices for substrates exceeding 200 mm in diameter. While discrete ion focusing can be used to direct a significantly large ion flux to an extraction slit, there are many open questions concerning the stability, performance, and possible electrode erosion challenges that an ion source based on this principle may face.

As presented, the 3D plasma-sheath-lens concept is broader and can include not only configurations manifesting modal and discrete ion focusing effects. 3D sheath aspects are already important in plasma processes for nanofabrication. Sometimes, due to uniformity issues, such effects should be avoided. However, a more detailed understanding of 3D sheath can help to develop new processes or use in purpose the observed non-uniformities to reveal desired information.

6. Included publications

The scientific content included in chapters 2 to 4 is based on 17 journal publications and 2 patents authored or coauthored by the author of this dissertation. The authors, titles, references, and abstracts are listed below.

ES1

E. Stamate and H. Sugai

Modal focusing effect of positive and negative ions by a three-dimensional plasma-sheath lens

Phys. Rev. Lett. (2005) 94, 125004-125007

Abstract

A complex focusing effect of positive and negative ions caused by the sheath forming to biased electrodes that interface insulators has been found by solving in three dimensions the potential distribution and ion kinetics within the sheath. Thus, intrinsically correlated with the sheath shape, certain electrical charges are focused on the surface, forming well defined patterns named modal lines and modal spots. Their superposition to the previously reported discrete focusing leads to a total flux that represents a "fingerprint" of the entire sheath on the electrode surface. The ion flux pattern is developed experimentally on the surface of square and octagonal electrodes exposed to Ar/SF₆ and CF₄ plasmas. Present results are of high potential importance for fundamental studies concerning sheath formation and charge kinetics and also in a wide range of plasma applications.

Reproduced from DOI: 10.1103/PhysRevLett.94.125004 with permission of the American Physical Society.

ES2

E. Stamate and H. Sugai

Discrete focusing effect of positive ions by a plasmas-sheath lens

Phys. Rev. E. (2005) 72, 036407-036414

Abstract

We demonstrate that the sheath created adjacent to the surface of a negatively biased electrode that interfaces an insulator acts as a lens that focuses the positive ions to distinct regions on the surface. Thus, the positive ion flux is discrete, leading to the formation of a passive surface, of no ion impact, near the edge and an active surface at the center. Trajectories of positive ions within the sheath are obtained by solving in three dimensions the Poisson equation for electrodes of different geometry. Simulations are confirmed by developing the ion flux profile on the electrode surface as the sputtering pattern produced by ion impact. Measurements are performed in a dc plasma produced in Ar gas.

Reproduced from DOI: 10.1103/PhysRevE.72.036407 with permission of the American Physical Society.

ES3

E. Stamate

Discrete and Modal focusing effects – principles and applications

Plasma Phys. Contr. Fusion. 54 (2012) 124048 11 p.

Abstract

Charge flux distribution on the surface of biased electrodes of different geometries immersed in plasma is investigated by three-dimensional simulations and experiments. It is demonstrated that the sheath surrounding the electrodes that interface insulators act as an electrostatic lens, focusing the charges to distinct locations on the electrode surface depending on the entrance coordinates at the sheath edge. Two focusing effects are identified. Discrete focusing leads to the formation of a passive surface of no ion impact, near the edge of the electrodes interfacing insulators. Modal focusing results in the formation of certain 'modal spots' and/or 'modal lines'. Several phenomenological aspects and potential applications are reviewed and further discussed, including charge focusing by a three-dimensional plasma-sheath-lens, ion dose uniformity during plasma immersion ion implantation, mass spectrometry and plasma monitoring.

Reproduced from DOI: 10.1088/0741-3335/54/12/124048 with permission of the Institute of Physics Publishing Ltd.

ES4

E. Stamate, H. Yamaguchi

Fine structure of modal focusing effect in a three-dimensional plasma-sheath-lens formed by disk electrodes

Appl. Phys. Lett. 107 (2015) 094106.

Abstract

Modal and discrete focusing effects associated with three-dimensional plasma-sheath-lenses show promising potential for applications in ion beam extraction, mass spectrometry, plasma diagnostics and for basic studies of plasma sheath. The ion focusing properties can be adjusted by controlling the geometrical structure of the plasma-sheath-lens and plasma parameters. The positive and negative ion kinetics within the plasma-sheath-lens are investigated both experimentally and theoretically and a modal focusing ring is identified on the surface of disk electrodes. The focusing ring is very sensitive to the sheath thickness and can be used to monitor very small changes in plasma parameters. Three dimensional simulations are found to be in very good agreement with experiments.

Reproduced from DOI: 10.1063/1.4930063 with permission of the American Institute of Physics.

ES5

M. Draghici and E. Stamate

Properties and etching rates of negative ions in inductively coupled plasmas and dc discharges produced in Ar/SF₆

J. Appl. Phys. 107 (2010) 123304 (9 pp)

Abstract

Negative ion production is investigated in a chamber with transversal magnetic filter operated in dc or inductively coupled plasma (ICP) modes in Ar/SF₆ gas mixtures. Plasma parameters are evaluated by mass spectrometry and Langmuir probe for different discharge conditions. The density ratio of negative ion to electron exceeded 300 in dc mode while it was below 100 in the ICP mode. The possibility to apply a large positive bias to an electrode without affecting the plasma potential and the transition from a negative sheath to anodic glow are also investigated. The etching rates by positive and negative ions are evaluated on silicon substrate for different Ar/SF₆ gas ratios. The etching rate by negative ions was less than 5% smaller than that by positive ions.

Reproduced from DOI:10.1063/1.3452357 with permission of the American Institute of Physics.

ES6

M. Draghici and E. Stamate

Properties of highly electronegative plasmas produced in a multipolar magnetic-confined device with a transversal magnetic filter

J. Phys. D: Appl. Phys. 43 (2010) 155205

Abstract

Highly electronegative plasmas were produced in Ar/SF₆ gas mixtures in a dc discharge with multipolar magnetic confinement and transversal magnetic filter. Langmuir probe and mass spectrometry were used for plasma diagnostics. Plasma potential drift, the influence of small or large area biased electrodes on plasma parameters, the formation of the negative ion sheath and etching rates by positive and negative ions have been investigated for different experimental conditions. When the electron temperature was reduced below 1 eV the density ratio of negative ion to electron exceeded 100 even for very low amounts of SF₆ gas. The plasma potential drift could be controlled by proper wall conditioning. A large electrode biased positively had no effect on plasma potential for density ratios of negative ions to electrons larger than 50. For similar electronegativities or higher a negative ion sheath could be formed by applying a positive bias of a few hundred volts.

Reproduced from DOI:10.1088/0022-3727/43/15/155205 with permission of the Institute of Physics Publishing Ltd.

ES7

E. Stamate, Holtzer N. and H. Sugai

Complex ion-focusing effect by the sheath above the wafer in plasma immersion ion implantation

Appl. Phys. Lett. (2005) 86, 261501-261504

Abstract

The ion flux on the wafer surface during plasma immersion ion implantation is investigated by three-dimensional simulations and experiments. Due to the finite size of the wafer and its stage, the evolving sheath acts as a lens that focuses the positive ions to distinct regions on the wafer surface. Depending on the sheath profile, two focusing effects are identified. Discrete focusing involves ions entering the sheath from its frontal side and leads to the formation of a passive surface near the wafer edge, while the modal focusing affects ions entering the sheath from the lateral side of the stage and are eventually directed to the wafer center.

Reproduced from DOI: 10.1063/1.1951045 with permission of the American Institute of Physics.

ES8

E. Stamate and H. Sugai

Controlling the ion flux on substrates of different geometry by sheath-lens focusing effect

Thin Solid Films, 515 (2007) 4853-4859.

Abstract

It is shown that a three-dimensional plasma sheath lens that forms on biased electrodes interfacing insulators exhibits novel characteristics such as ion focusing on desired locations, controllability of ion flux uniformity, formation of passive surfaces and applicability to plasma diagnostics. The ion flux profile on substrates of different geometry is obtained by three dimensional simulations of potential distribution and ion trajectory, while experiments are realized in electropositive and electronegative DC and ICP discharges.

Reproduced from DOI: 10.1016/j.tsf.2006.10.071 with permission of the Elsevier B.V.

ES9

E. Stamate, N. Holtzer and H. Sugai,
Improvement of the Dose Uniformity in Plasma Immersed Ion Implantation
by Introducing a Vertical Biased Ring
Thin Solid Films, (2006) 506-507, 571-574

Abstract

It is shown that the sheath evolving to a negatively biased wafer during the plasma immersed ion implantation focuses the positive ions to distinct regions on the surface resulting in a poor uniformity of the ion dose. The focusing mechanism is investigated and solutions to improve the ion dose uniformity are proposed based on three-dimensional calculations of the potential distribution and ion trajectories within the sheath structure. Simulations are confirmed at lower scale in a DC Ar plasma which allows an easier visualization of the focusing phenomenon simultaneously with the measurement of the involved currents. (c) 2005 Elsevier B.V. All rights reserved.

Reproduced from DOI: 10.1016/j.tsf.2005.08.055 with permission of the Elsevier B.V.

ES10

E. Stamate, H. Sugai, O. Takai and K. Ohe

Sheath lens probe for negative ion detection in reactive plasma

J. Appl. Phys. (2004) 95, 830-833

Abstract

A method that allows easy and inexpensive detection of negative ions is introduced. The method is based upon the electrostatic lens effect of the sheath layer evolving to a positively biased planar probe that focuses the negative charges to distinct regions on the surface. Trajectories of negative ions inside the sheath are obtained after computing the potential and electric field distribution by solving in three dimensions the nonlinear Poisson equation. The negative ions' flux to square and disk probes is developed in Ar/SF₆ and O₂ plasmas. The method allows negative ion detection with sensitivity higher than that of Langmuir probes. (C) 2004 American Institute of Physics.

Reproduced from DOI:10.1063/1.1619225 with permission of the American Institute of Physics.

ES11

E. Stamate

Status and challenges in electrical diagnostics of processing plasmas
Surf. Coat. Technol. 260 (2014) 401-410

Abstract

Dry processing based on reactive plasmas was the main driving force for micro- and recently nano-electronic industry. Once with the increase in plasma complexity new diagnostics methods have been developed to ensure a proper process control during etching, thin film deposition, ion implantation or other steps in device fabrication. This work reviews some of the unconventional methods developed in the last two decays to measure the parameters of reactive plasmas including the test function method, thermal probes, and plasma-sheath-lens probes. Negative ion detection and surface contamination in plasmas with a high degree of contamination are also addressed. (C) 2014 Elsevier B.V. All rights reserved.

Reproduced from DOI: 10.1016/j.surfcoat.2014.09.070 with permission of the Elsevier B.V.

ES12

E. Stamate and M. Draghici

High electronegativity multi-dipolar electron cyclotron resonance plasma source for etching with negative ions

J. Appl. Phys. 111 (2012) 083383, 6 pp.

Abstract

A large area plasma source based on 12 multi-dipolar ECR plasma cells arranged in a 3 x 4 matrix configuration was built and optimized for silicon etching by negative ions. The density ratio of negative ions to electrons exceeded 300 in Ar/SF₆ gas mixture when a magnetic filter was used to reduce the electron temperature to about 1.2 eV. Mass spectrometry and electrostatic probe were used for plasma diagnostics. The new source is free of density jumps and instabilities and shows a very good stability for plasma potential, and the dominant negative ion species is F⁻. The magnetic field in plasma volume is negligible and there is no contamination by filaments. The etching rate by negative ions measured in Ar/SF₆/O₂ mixtures was almost similar with that by positive ions reaching 700 nm/min. (C) 2012 American Institute of Physics.

Reproduced from DOI: 10.1063/1.4704696 with permission of the American Institute of Physics.

ES13

E. Stamate

Ion beam extraction by discrete ion focusing

Patent No.: US 9,318,297 B2

Abstract

An apparatus and methods are disclosed for ion beam extraction. In an implementation, the apparatus includes a plasma source (or plasma) and an ion extractor. The plasma source is adapted to generate ions and the ion extractor is immersed in the plasma source to extract a fraction of the generated ions. The ion extractor is surrounded by a space charge formed at least in part by the extracted ions. The ion extractor includes a biased electrode forming an interface with an insulator. The interface is customized to form a strongly curved potential distribution in the space-charge surrounding the ion extractor. The strongly curved potential distribution focuses the extracted ions towards an opening on a surface of the biased electrode thereby resulting in an ion beam.

ES14

E. Stamate

Ion mass determination

WO 2010/094605 A1

World Intellectual Property Organization

Abstract

An apparatus is described for determining the mass of ions, the apparatus configured to hold a plasma having a plasma potential. The apparatus comprises an electrode having a surface extending in a surface plane and an insulator interfacing with the electrode. An electric potential provider is configured to provide an electric potential different than the potential of the plasma to the electrode, thereby forming a curved potential distribution in the plasma surrounding the electrode. A magnetic field source is configured to provide a magnetic field across at least part of the curved potential distribution in the plasma surrounding the electrode. An ion impact detector is configured to detect impacts of ions arriving at the electrode, the detecting comprising detecting of locations of the impacts, and a processing unit configured to interpret the detected impact locations in terms of the mass of the impacting ions.

ES15

E. Stamate

Spatially resolved optoelectronic properties of Al-doped zinc oxide films deposited by radio-frequency magnetron plasma sputtering without substrate heating

Nanomaterials 10 (2020) 14

Abstract

Transparent and conducting thin films were deposited on soda lime glass by RF magnetron sputtering without intentional substrate heating using an aluminum doped zinc oxide target of 2 inch in diameter. The sheet resistance, film thickness, resistivity, averaged transmittance, and energy band gaps were measured with 2 mm spatial resolution for different target-to-substrate distances, discharge pressures and powers. Hall mobility, carrier concentration, SEM and XRD were performed with a 3 mm spatial resolution. The results reveal a very narrow range of parameters that can lead to reasonable resistivity values while the transmittance is much less sensitive and less correlated with the already well-documented negative effects caused by a higher concentration of oxygen negative ions and atomic oxygen at the erosion tracks. A possible route to improve the thin film properties requires the need to reduce the oxygen negative ion energy and investigate the growth mechanism in correlation with spatial distribution of thin film properties and plasma parameters.

Reproduced from DOI: 10.3390/nano10010014 with permission of the MDPI.

ES16

M.A. Petrea and E. Stamate

Spatial distribution of plasma parameters by a dual thermal-electrostatic probe in RF and DC magnetron sputtering discharges during deposition of aluminum doped zinc oxide thin films,
Plasma Sources. Sci. Technol. 30 (2021) 045002.

Abstract

Aluminum doped zinc oxide thin films deposited by magnetron plasma sputtering are essential for various optoelectronic applications. So far, the oxygen negative ions and the atomic oxygen are regarded as responsible for the poor spatial uniformity of thin film resistivity. While various methods are available for thin film characterization, understanding the growth mechanism requires spatial-resolved measurements of plasma parameters. This work uses a dual thermal-electrostatic probe that can reveal the spatial distribution of plasma density, electron temperature and plasma potential. The results exhibit a parabolic profile for plasma density and flat profiles for electron temperature and plasma potential, with no correlation with the strong distribution of thin film resistivity that mirrors the erosion track on the target surface.

Reproduced from DOI:10.1088/1361-6595/abec25 with permission of the Institute of Physics Publishing Ltd.

ES17

E. Stamate

Lowering the resistivity of aluminum doped zinc oxide thin films by controlling the self-bias during RF magnetron sputtering
Surf. Coat. Technol. 402 (2020) 126306.

Abstract

Transparent conducting thin films based on aluminum-doped zinc oxide are regarded as a viable alternative for low-cost and large-area applications such as solar cells and smart windows. Despite intensive research, the thin film growth mechanism by magnetron sputtering is under debate concerning the role of energetic oxygen negative ions and the spatial distribution of atomic oxygen during the deposition. As the negative ions energy is directly related to the self-bias during RF driven magnetron sputtering, this work demonstrates a method to lower the thin film resistivity with a factor above 2 by including a tuning electrode between the target and the substrate. The electrode increases the RF coupling, reduces the dc self-bias, and improves the electronic properties uniformity over the substrate. Consequently, resistivity below $3 \times 10^{-3} \Omega \text{ cm}$ is obtained over a substrate area comparable with the target surface for an averaged transmittance above 90% without intentional substrate heating.

Reproduced from DOI: 10.1016/j.surfcoat.2020.126306 with permission of the Elsevier B.V.

ES18

S. Khan and E. Stamate

Comparative study of aluminium-doped zinc oxide, gallium doped zinc oxide and indium doped tin oxide thin films deposited by radio frequency magnetron sputtering
Nanomaterials, 12 (2022) 1593

Abstract

A timely replacement of the rather expensive indium-doped tin oxide with aluminum-doped zinc oxide is hindered by the poor uniformity of electronic properties when deposited by magnetron sputtering. Recent results demonstrated the ability to improve the uniformity and to decrease the resistivity of aluminum-doped zinc oxide thin films by decreasing the energy of the oxygen-negative ions assisting in thin film growth by using a tuning electrode. In this context, a comparative study was designed to elucidate if the same phenomenology holds for gallium-doped zinc oxide and indium-doped tin oxide as well. The metal oxide thin films have been deposited in the same setup for similar discharge parameters, and their properties were measured with high spatial resolution and correlated with the erosion track on the target's surface. Furthermore, the films were also subject to post annealing and degradation tests by wet etching. While the tuning electrode was able to reduce the self-bias for all three materials, only the doped zinc oxide films exhibited properties correlating with the erosion track.

Reproduced from DOI: 10.3390/nano12091539 with permission of the MDPI.

ES19

K. Norrman, P. Norby, E. Stamate

Preferential zinc sputtering during the growth of aluminum doped zinc oxide thin films by radio frequency magnetron sputtering

J. Mater. Chem. C. 10 (2022) 14444-14452

Abstract

Aluminum doped ZnO is one of the main candidates to replace indium tin oxide used as a transparent conducting oxide. Despite intensive research, the mechanism behind the poor thin-film-resistivity uniformity over the sample deposited by magnetron sputtering is not completely understood. Several independent reports correlate the mirroring of an erosion track on the substrate with energetic negative oxygen ions. However, their role in assisting the thin film growth is not known. In this work, the physical and chemical properties of aluminum doped ZnO are measured with a high spatial resolution at different thin film deposition pressures. The results show that Zn depletion by energetic negative oxygen ion re-sputtering is the main factor correlating with the resistivity and the band gap energy profiles of the deposited films.

Reproduced from DOI: 10.1039/d2tc02180c with permission of the Royal Society of Chemistry.

7. References

1. Samukawa, S. *et al.* The 2012 plasma roadmap. *J. Phys. D. Appl. Phys.* **45**, (2012).
2. Adamovich, I. *et al.* The 2017 Plasma Roadmap: Low temperature plasma science and technology. *J. Phys. D. Appl. Phys.* **50**, (2017).
3. Helmersson, U., Lattemann, M., Bohlmark, J., Ehasarian, A. P. & Gudmundsson, J. T. Ionized physical vapor deposition (IPVD): A review of technology and applications. *Thin Solid Films* **513**, 1–24 (2006).
4. Anders, A. A structure zone diagram including plasma-based deposition and ion etching. *Thin Solid Films* **518**, 4087–4090 (2010).
5. Pelletier, J. & Anders, A. Plasma-based ion implantation and deposition: A review of physics, technology, and applications. *IEEE Trans. Plasma Sci.* **33**, 1944–1959 (2005).
6. Abe, H., Yoneda, M. & Fujiwara, N. Developments of plasma etching technology for fabricating semiconductor devices. *Jpn. J. Appl. Phys.* **47**, 1435–1455 (2008).
7. Donnelly, V. M. & Kornblit, A. Plasma etching: Yesterday, today, and tomorrow. *J. Vac. Sci. Technol. A Vacuum, Surfaces, Film.* **31**, 050825 (2013).
8. Ifuku, T. *et al.* Nanoimprint performance improvements for high volume semiconductor device manufacturing. 13 (2022) doi:10.1117/12.2643212.
9. Tachi, S. Impact of plasma processing on integrated circuit technology migration: From 1 μm to 100 nm and beyond. *J. Vac. Sci. Technol. A Vacuum, Surfaces, Film.* **21**, S131–S138 (2003).
10. Hershkovitz, N. Sheaths: More complicated than think. *Phys. Plasmas* **12**, 1–11 (2005).
11. Jelić, N. *et al.* Fluid and kinetic parameters near the plasma-sheath boundary for finite Debye lengths. *Phys. Plasmas* **14**, (2007).

12. Tsankov, T. V. & Czarnetzki, U. Reply to ‘Comment on “Information hidden in the velocity distribution of ions and the exact kinetic Bohm criterion”’. *Plasma Sources Sci. Technol.* **28**, (2019).
13. Riemann, K. U. Plasma and sheath. *Plasma Sources Sci. Technol.* **18**, (2009).
14. Sternberg, N. & Godyak, V. The Bohm plasma-sheath model and the bohm criterion revisited. *IEEE Trans. Plasma Sci.* **35**, 1341–1349 (2007).
15. Franklin, R. N. The quest to find the plasma edge and discover a collisionally modified Bohm criterion. *J. Plasma Phys.* **79**, 453–455 (2013).
16. Iwase, T. *et al.* Progress and perspectives in dry processes for leading-edge manufacturing of devices: Toward intelligent processes and virtual product development. *Jpn. J. Appl. Phys.* **58**, (2019).
17. Xiao, S. Q., Xu, S. & Ostrikov, K. Low-temperature plasma processing for Si photovoltaics. *Mater. Sci. Eng. R Reports* **78**, 1–29 (2014).
18. Hegemann, D. & Gaiser, S. Plasma surface engineering for manmade soft materials: A review. *J. Phys. D. Appl. Phys.* **55**, (2022).
19. Sealy, C. & Sealy, C. 3D nanoelectronics ease computing bottleneck. *Nano Today* **16**, 1–2 (2017).
20. Osada, M. & Sasaki, T. Two-dimensional dielectric nanosheets: Novel nanoelectronics from nanocrystal building blocks. *Adv. Mater.* **24**, 210–228 (2012).
21. Akinwande, D., Petrone, N. & Hone, J. Two-dimensional flexible nanoelectronics. *Nat. Commun.* **5**, (2014).
22. Fischer, A. C. *et al.* Integrating MEMS and ICs. *Microsystems Nanoeng.* **1**, 1–16 (2015).
23. Ferrari, S. *et al.* Latest advances in the manufacturing of 3D rechargeable lithium microbatteries. *J. Power Sources* **286**, 25–46 (2015).

24. Jang, Y. W. *et al.* Intact 2D/3D halide junction perovskite solar cells via solid-phase in-plane growth. *Nat. Energy* **6**, 63–71 (2021).
25. Lethien, C., Le Bideau, J. & Brousse, T. Challenges and prospects of 3D micro-supercapacitors for powering the internet of things. *Energy Environ. Sci.* **12**, 96–115 (2019).
26. Takizawa, K., Kono, A. & Sasaki, K. Distribution of electric field in the sheath of an electronegative plasma. *Appl. Phys. Lett.* **90**, 2006–2008 (2007).
27. Czarnetzki, U., Luggenhölscher, D. & Döbele, H. F. Space and time resolved electric field measurements in helium and hydrogen RF-discharges. *Plasma Sources Sci. Technol.* **8**, 230–248 (1999).
28. Czarnetzki, U., Luggenhölscher, D. & Döbele, H. F. Sensitive electric field measurement by fluorescence-dip spectroscopy of rydberg states of atomic hydrogen. *Phys. Rev. Lett.* **81**, 4592–4595 (1998).
29. Yang, Y. & Kushner, M. J. Graded conductivity electrodes as a means to improve plasma uniformity in dual frequency capacitively coupled plasma sources. *J. Phys. D. Appl. Phys.* **43**, (2010).
30. Malik, S. M., Fetherston, R. P., Sridharan, K. & Conrad, J. R. Sheath dynamics and dose analysis for planar targets in plasma source ion implantation. *Plasma Sources Sci. Technol.* **2**, 81–85 (1993).
31. Tian, X. B. *et al.* Two-dimensional numerical simulation of non-uniform plasma immersion ion implantation. *Surf. Coatings Technol.* **186**, 47–52 (2004).
32. Sheridan, T. E. Calculation of two-dimensional plasma sheath with application to radial dust oscillations. *J. Appl. Phys.* **98**, 1–6 (2005).
33. Sheridan, T. E. Ion focusing by an expanding, two-dimensional plasma sheath. *Appl. Phys. Lett.* **68**, 1918–1920 (1996).
34. Lee, D., Hershkowitz, N. & Severn, G. D. Measurements of Ar⁺ and Xe⁺ velocities near the sheath boundary of Ar-Xe plasma using two diode lasers. *Appl. Phys. Lett.* **91**, 2005–2008 (2007).

35. Hatami, M. M. An analytic expression for the sheath criterion in magnetized plasmas with multi-charged ion species. *Phys. Plasmas* **22**, (2015).
36. Shaw, A. K., Kar, S. & Goswami, K. S. The positive ion temperature effect in magnetized electronegative plasma sheath with two species of positive ions. *Phys. Plasmas* **19**, (2012).
37. Gudmundsson, J. T. & Lieberman, M. A. Ar⁺ and Xe⁺ velocities near the presheath-sheath boundary in an Ar/Xe discharge. *Phys. Rev. Lett.* **107**, 1–4 (2011).
38. Oksuz, L. & Hershkowitz, N. First Experimental Measurements of the Plasma Potential throughout the Presheath and Sheath at a Boundary in a Weakly Collisional Plasma. *Phys. Rev. Lett.* **89**, 2–4 (2002).
39. Sheehan, J. P. & Hershkowitz, N. Emissive probes. *Plasma Sources Sci. Technol.* **20**, (2011).
40. Biloiu, C. *et al.* Evolution of the parallel and perpendicular ion velocity distribution functions in pulsed helicon plasma sources obtained by time resolved laser induced fluorescence. *Plasma Sources Sci. Technol.* **14**, 766–776 (2005).
41. Scime, E. *et al.* Laser induced fluorescence in a pulsed argon plasma. *Rev. Sci. Instrum.* **76**, 2003–2006 (2005).
42. Biloiu, I. A., Scime, E. E. & Biloiu, C. One- and two-dimensional laser induced fluorescence at oblique incidence. *Plasma Sources Sci. Technol.* **18**, (2009).
43. Racka-Szmidt, K., Stonio, B., Żelazko, J., Filipiak, M. & Sochacki, M. A review: Inductively coupled plasma reactive ion etching of silicon carbide. *Materials (Basel)*. **15**, (2022).
44. Dussart, R., Tillocher, T., Lefauchaux, P. & Boufnichel, M. Plasma cryogenic etching of silicon: From the early days to today's advanced technologies. *J. Phys. D. Appl. Phys.* **47**, (2014).
45. Jansen, H. V., De Boer, M. J., Unnikrishnan, S., Louwerse, M. C. &

- Elwenspoek, M. C. Black silicon method X: A review on high speed and selective plasma etching of silicon with profile control: An in-depth comparison between Bosch and cryostat DRIE processes as a roadmap to next generation equipment. *J. Micromechanics Microengineering* **19**, (2009).
46. Donnelly, V. M. Review Article: Reactions of fluorine atoms with silicon, revisited, again. *J. Vac. Sci. Technol. A Vacuum, Surfaces, Film.* **35**, 05C202 (2017).
 47. Fukumoto, H., Fujikake, I., Takao, Y., Eriguchi, K. & Ono, K. Plasma chemical behaviour of reactants and reaction products during inductively coupled CF₄ plasma etching of SiO₂. *Plasma Sources Sci. Technol.* **18**, (2009).
 48. Kersten, H., Deutsch, H., Steffen, H., Kroesen, G. M. W. & Hippler, R. The energy balance at substrate surfaces during plasma processing. *Vacuum* **63**, 385–431 (2001).
 49. Constantine, C., Barratt, C., Pearton, S. J., Ren, F. & Lothian, J. R. Smooth, low-bias plasma etching of InP in microwave Cl₂/CH₄/H₂ mixtures. *Appl. Phys. Lett.* **61**, 2899–2901 (1992).
 50. Eddy, C. R. *et al.* Characterization of high density CH₄/H₂/Ar plasmas for compound semiconductor etching. *J. Vac. Sci. Technol. A Vacuum, Surfaces, Film.* **17**, 780–792 (1999).
 51. Wagner, J. A. & Katsch, H. M. Negative oxygen ions in a pulsed RF-discharge with inductive coupling in mixtures of noble gases and oxygen. *Plasma Sources Sci. Technol.* **15**, 156–169 (2006).
 52. Katsch, H. M., Manthey, C., Wagner, J. A. & Döbele, H. F. Negative ions in argon - Oxygen discharges. *Surf. Coatings Technol.* **200**, 831–834 (2005).
 53. Fujii, T., Aoyagi, H., Kusaba, K., Horiike, Y. & Shindo, H. Enhancement of negative-ion-assisted silicon oxidation by radio-frequency bias. *Japanese J. Appl. Physics, Part 2 Lett.* **38**, 2–5 (1999).
 54. Sharma, N., Chakraborty, M., Neog, N. K. & Bandyopadhyay, M.

- Influence of magnetic filter and magnetic cage in negative ion production in helicon oxygen plasma. *Phys. Plasmas* **25**, (2018).
55. Morales Crespo, R., Munoz-Serrano, E., Tejero-Del-Caz, A. & Casado, E. Three-fluid model of the plasma-sheath region for a planar probe immersed in an active oxygen discharge. Validity of the Boltzmann relation. *Plasma Sources Sci. Technol.* **30**, (2021).
 56. Scribbins, S., Bowes, M. & Bradley, J. W. The spatial distribution of negative oxygen ion densities in a dc reactive magnetron discharge. *J. Phys. D. Appl. Phys.* **46**, (2013).
 57. Stamate, E. & Ohe, K. Determination of negative-ion and electron parameters in an Ar/SF₆ plasma. *J. Appl. Phys.* **84**, (1998).
 58. Stamate, E. & Ohe, K. Probe diagnostics of electronegative plasmas with bi-Maxwellian electrons. *J. Appl. Phys.* **89**, (2001).
 59. Samukawa, S. Ultimate top-down etching processes for future nanoscale devices: Advanced neutral-beam etching. *Japanese J. Appl. Physics, Part 1 Regul. Pap. Short Notes Rev. Pap.* **45**, 2395–2407 (2006).
 60. Matsui, J., Nakano, N., Petrović, Z. L. & Makabe, T. The effect of topographical local charging on the etching of deep-submicron structures in SiO₂ as a function of aspect ratio. *Appl. Phys. Lett.* **78**, 883–885 (2001).
 61. Sekine, M. Dielectric film etching in semiconductor device manufacturing. *Appl. Surf. Sci.* **192**, 270–298 (2002).
 62. Kanakasabapathy, S. K., Overzet, L. J., Midha, V. & Economou, D. Alternating fluxes of positive and negative ions from an ion-ion plasma. *Appl. Phys. Lett.* **78**, 22–24 (2001).
 63. Ohtake, H. & Samukawa, S. Charge-free etching process using positive and negative ions in pulse-time modulated electron cyclotron resonance plasma with low-frequency bias. *Appl. Phys. Lett.* **68**, 2416 (1995).
 64. Banna, S. *et al.* Pulsed high-density plasmas for advanced dry

- etching processes. *J. Vac. Sci. Technol. A Vacuum, Surfaces, Film.* **30**, 040801 (2012).
65. Economou, D. J. Pulsed plasma etching for semiconductor manufacturing. *J. Phys. D. Appl. Phys.* **47**, (2014).
 66. Ohmori, T., Goto, T. K., Kitajima, T. & Makabe, T. Negative charge injection to a positively charged SiO₂ hole exposed to plasma etching in a pulsed two-frequency capacitively coupled plasma in CF₄/Ar. *Appl. Phys. Lett.* **83**, 4637–4639 (2003).
 67. Lafleur, T., Rafalskyi, D. & Aanesland, A. Alternate extraction and acceleration of positive and negative ions from a gridded plasma source. *Plasma Sources Sci. Technol.* **24**, (2015).
 68. Kanakasabapathy, S. K., Khater, M. H. & Overzet, L. J. Comparison of negative-ion and positive-ion-assisted etching of silicon. *Appl. Phys. Lett.* **79**, 1769–1771 (2001).
 69. Ishikawa, J. Negative-ion source applications (invited). *Rev. Sci. Instrum.* **79**, 1–5 (2008).
 70. Ishikawa, J. Applications of heavy-negative-ion sources for materials science (invited). *Rev. Sci. Instrum.* **71**, 1036–1041 (2000).
 71. Vozniy, O. V. & Yeom, G. Y. High-energy negative ion beam obtained from pulsed inductively coupled plasma for charge-free etching process. *Appl. Phys. Lett.* **94**, 3–5 (2009).
 72. Kubota, T. *et al.* 200-Mm-Diameter Neutral Beam Source Based on Inductively Coupled Plasma Etcher and Silicon Etching. *J. Vac. Sci. Technol. A Vacuum, Surfaces, Film.* **28**, 1169–1174 (2010).
 73. Ichiki, K. & Hatakeyama, M. Characterization of neutral beam source using dc cold cathode discharge and its application processes. *J. Phys. D. Appl. Phys.* **41**, (2008).
 74. Kubota, T. *et al.* Study of neutral-beam etching conditions for the fabrication of 7-nm-diameter nanocolumn structures using ferritin iron-core masks. *J. Vac. Sci. Technol. B Microelectron. Nanom. Struct.* **23**, 534 (2005).

75. Mazouffre, S. Electric propulsion for satellites and spacecraft: Established technologies and novel approaches. *Plasma Sources Sci. Technol.* **25**, (2016).
76. Rafalskyi, D. & Aanesland, A. Brief review on plasma propulsion with neutralizer-free systems. *Plasma Sources Sci. Technol.* **25**, (2016).
77. Smirnov, A., Raites, Y. & Fisch, N. J. Maximizing ion current by space-charge neutralization using negative ions and dust particles. *Phys. Plasmas* **12**, 1–8 (2005).
78. Taccogna, F., Schneider, R., Longo, S. & Capitelli, M. Modeling of surface-dominated plasmas: From electric thruster to negative ion source. *Rev. Sci. Instrum.* **79**, (2008).
79. Spädtke, P. Model for the description of ion beam extraction from electron cyclotron resonance ion sources. *Rev. Sci. Instrum.* **81**, 25–28 (2010).
80. Chutjian, A., Garscadden, A. & Wadehra, J. M. Electron attachment to molecules at low electron energies. *Phys. Rep.* **264**, 393–470 (1996).
81. Makabe, T. Current status and nature of high-frequency electronegative plasmas: Basis for material processing in device manufacturing. *Jpn. J. Appl. Phys.* **58**, (2019).
82. Lichtenberg, A. J., Vahedi, V., Lieberman, M. A. & Rognlien, T. Modeling electronegative plasma discharges. *J. Appl. Phys.* **75**, 2339–2347 (1994).
83. Schulze, J. *et al.* Ionization by drift and ambipolar electric fields in electronegative capacitive radio frequency plasmas. *Phys. Rev. Lett.* **107**, 1–5 (2011).
84. Kim, S., Lieberman, M. A., Lichtenberg, A. J. & Gudmundsson, J. T. Improved volume-averaged model for steady and pulsed-power electronegative discharges. *J. Vac. Sci. Technol. A Vacuum, Surfaces, Film.* **24**, 2025–2040 (2006).
85. Chabert, P., Lichtenberg, A. J., Lieberman, M. A. & Marakhtanov, A.

- M. Instabilities in low-pressure electronegative inductive discharges. *Plasma Sources Sci. Technol.* **10**, 478–489 (2001).
86. Franklin, R. N. Electronegative plasmas - Why are they so different? *Plasma Sources Sci. Technol.* **11**, (2002).
 87. Economou, D. J. Fundamentals and applications of ion-ion plasmas. *Appl. Surf. Sci.* **253**, 6672–6680 (2007).
 88. Kouznetsov, I. G., Lichtenberg, A. J. & Lieberman, M. A. Internal sheaths in electronegative discharges. *J. Appl. Phys.* **86**, 4142–4153 (1999).
 89. Ferrell, J. Drift. *Routledge Companion to Criminol. Theory Concepts* **71**, 168–171 (2017).
 90. Helander, P. Theory of plasma confinement in non-axisymmetric magnetic fields. *Reports Prog. Phys.* **77**, (2014).
 91. Asmussen, J., Grotjohn, T. A., Mak, P. & Perrin, M. A. Cyclotron Resonance Discharges. **25**, 1196–1221 (1997).
 92. Sengupta, A. Magnetic confinement in a ring-cusp ion thruster discharge plasma. *J. Appl. Phys.* **105**, (2009).
 93. Stenzel, R. L., Urrutia, J. M., Teodorescu-Soare, C. T., Ionita, C. & Schrittwieser, R. Magnetic dipole discharges. I. Basic properties. *Phys. Plasmas* **20**, 083503 (2013).
 94. Oudini, N., Taccogna, F., Minelli, P., Aanesland, A. & Raimbault, J. L. Negative ion extraction from hydrogen plasma bulk. *Phys. Plasmas* **20**, (2013).
 95. Cavenago, M. & Veltri, P. Deflection compensation for multiaperture negative ion beam extraction: Analytical and numerical investigations. *Plasma Sources Sci. Technol.* **23**, (2014).
 96. Liang, J. *et al.* Magnetron sputtering enabled sustainable synthesis of nanomaterials for energy electrocatalysis. *Green Chem.* **23**, 2834–2867 (2021).

97. Hatami, M. M. & Shokri, B. Bohm's criterion in a collisional magnetized plasma with thermal ions. *Phys. Plasmas* **19**, (2012).
98. Chalise, R. & Khanal, R. A kinetic trajectory simulation model for magnetized plasma sheath. *Plasma Phys. Control. Fusion* **54**, (2012).
99. Zhang, Y., Charles, C. & Boswell, R. W. Density measurements in low pressure, weakly magnetized, RF plasmas: Experimental verification of the sheath expansion effect. *Front. Phys.* **5**, 1–6 (2017).
100. Ji, Y., Zou, X., Liu, H. & Qiu, M. Bohm criterion in a magnetized plasma sheath. *Plasma Sci. Technol.* **13**, 519–522 (2011).
101. Paul, R., Adhikari, S., Moulick, R., Kausik, S. S. & Saikia, B. K. Magnetized plasma sheath in the presence of negative ions. *Phys. Plasmas* **27**, (2020).
102. Pandey, B. P., Samarian, A. & Vladimirov, S. V. Dust in the magnetized sheath. *Phys. Plasmas* **14**, (2007).
103. Puttscher, M. *et al.* Vertical oscillations of dust particles in a strongly magnetized plasma sheath induced by horizontal laser manipulation. *Phys. Plasmas* **24**, (2017).
104. Hatami, M. M., Shokri, B. & Niknam, A. R. Collisional effects in magnetized plasma sheath with two species of positive ions. *J. Phys. D. Appl. Phys.* **42**, (2009).
105. Hatami, M. M. Sheath properties in active magnetized multi-component plasmas. *Sci. Rep.* **11**, 22–24 (2021).
106. Sharma, D. & Kaw, P. K. Valid flow combinations for stable sheath in a magnetized multiple ion species plasma. *Phys. Plasmas* **19**, (2012).
107. Moulick, R., Adhikari, S. & Goswami, K. S. Sheath formation in collisional, low pressure, and magnetized plasma. *Phys. Plasmas* **26**, (2019).
108. Yasserian, K., Aslaninejad, M., Ghoranneviss, M. & Aghamir, F. M. Sheath formation in a collisional electronegative magnetized discharge. *J. Phys. D. Appl. Phys.* **41**, (2008).

109. Basnet, S., Patel, A. & Khanal, R. Electronegative magnetized plasma sheath properties in the presence of non-Maxwellian electrons with a homogeneous ion source. *Plasma Phys. Control. Fusion* **62**, (2020).
110. Driouch, I., Chatei, H. & El Bojaddaini, M. Numerical study of the sheath in magnetized dusty plasma with two-temperature electrons. *J. Plasma Phys.* **96**, (2014).
111. Liu, J. Y. *et al.* RF plasma sheath in an oblique magnetic field. *Vacuum* **80**, 1206–1210 (2006).
112. Ewart, R. J., I Parra, F. & Geraldini, A. Sheath collapse at critical shallow angle due to kinetic effects. *Plasma Phys. Control. Fusion* **64**, (2022).
113. Li, D. & Wang, S. Particle simulation of a magnetized plasma sheath with the magnetic field parallel to the wall. *Phys. Plasmas* **25**, (2018).
114. Hatami, M. M. Dynamics of magnetized plasma sheaths around a trench. *Phys. Plasmas* **23**, (2016).
115. Chu, P. K. Applications of plasma-based technology to microelectronics and biomedical engineering. *Surf. Coatings Technol.* **203**, 2793–2798 (2009).
116. Spektor, R. Computation of two-dimensional electric field from the ion laser induced fluorescence measurements. *Phys. Plasmas* **17**, (2010).
117. Pérez-Luna, J., Hagelaar, G. J. M., Garrigues, L. & Boeuf, J. P. Method to obtain the electric field and the ionization frequency from laser induced fluorescence measurements. *Plasma Sources Sci. Technol.* **18**, (2009).
118. Zimmerman, D. C., McWilliams, R. & Edrich, D. A. Two-dimensional ion velocity distribution functions in inductively coupled argon plasma. *Plasma Sources Sci. Technol.* **14**, 581–588 (2005).
119. Stamate, E. & Sugai, H. Discrete focusing effect of positive ions by a plasma-sheath lens. *Phys. Rev. E - Stat. Nonlinear, Soft Matter Phys.* **72**, (2005).

120. Barnat, E. V. Multi-dimensional optical and laser-based diagnostics of low-temperature ionized plasma discharges. *Plasma Sources Sci. Technol.* **20**, (2011).
121. Barnat, E. V. & Hebner, G. A. Electric fields in a sheath near a metal-dielectric interface. *Appl. Phys. Lett.* **85**, 3393–3395 (2004).
122. McWilliams, R., Boehmer, H., Edrich, D., Zhao, L. & Zimmerman, D. Laser-induced fluorescence measurements for plasma processing. *Thin Solid Films* **506–507**, 665–668 (2006).
123. Takizawa, K., Sasaki, K. & Kono, A. Sensitive measurements of electric field distributions in low-pressure Ar plasmas by laser-induced fluorescence-dip spectroscopy. *Appl. Phys. Lett.* **84**, 185–187 (2004).
124. Mazouffre, S. Laser-induced fluorescence diagnostics of the cross-field discharge of Hall thrusters. *Plasma Sources Sci. Technol.* **22**, (2013).
125. Lucca Fabris, A., Young, C. V. & Cappelli, M. A. Time-resolved laser-induced fluorescence measurement of ion and neutral dynamics in a Hall thruster during ionization oscillations. *J. Appl. Phys.* **118**, (2015).
126. Durot, C. J., Gallimore, A. D. & Smith, T. B. Validation and evaluation of a novel time-resolved laser-induced fluorescence technique. *Rev. Sci. Instrum.* **85**, (2014).
127. Weatherford, B. R., Barnat, E. V. & Foster, J. E. Two-dimensional laser collision-induced fluorescence measurements of plasma properties near an RF plasma cathode extraction aperture. *Plasma Sources Sci. Technol.* **21**, (2012).
128. Nafarizal, N. *et al.* Two-dimensional distributions of Ti and Ti⁺ densities in high-pressure magnetron sputtering discharges. *Japanese J. Appl. Physics, Part 2 Lett.* **44**, 28–31 (2005).
129. Stamate, E. & Yeom, G. Y. *Dry etching. Handbook of Visual Display Technology* vol. 2 (2012).
130. Marchack, N. & Chang, J. P. Perspectives in nanoscale plasma

- etching: What are the ultimate limits? *J. Phys. D. Appl. Phys.* **44**, (2011).
131. Ding, J. C. *et al.* Low-temperature deposition of nanocrystalline Al₂O₃ films by ion source-assisted magnetron sputtering. *Vacuum* **149**, 284–290 (2018).
 132. Altieri, N. D., Chen, J. K.-C., Minardi, L. & Chang, J. P. Review Article: Plasma–surface interactions at the atomic scale for patterning metals. *J. Vac. Sci. Technol. A Vacuum, Surfaces, Film.* **35**, 05C203 (2017).
 133. Anders, A. Plasma and ion sources in large area coating: A review. *Surf. Coatings Technol.* **200**, 1893–1906 (2005).
 134. Gudmundsson, J. T. Physics and technology of magnetron sputtering discharges. *Plasma Sources Sci. Technol.* **29**, 113001 (2020).
 135. Han, J. G. Recent progress in thin film processing by magnetron sputtering with plasma diagnostics. *J. Phys. D. Appl. Phys.* **42**, (2009).
 136. Friedel, P. & Gourrier, S. Review of oxidation processes in plasmas†. *J. Phys. Chem. Solids* **44**, 353–364 (1983).
 137. Gavahian, M., Chu, Y. H., Mousavi Khaneghah, A., Barba, F. J. & Misra, N. N. A critical analysis of the cold plasma induced lipid oxidation in foods. *Trends Food Sci. Technol.* **77**, 32–41 (2018).
 138. Barati Darband, G., Aliofkhazraei, M., Hamghalam, P. & Valizade, N. Plasma electrolytic oxidation of magnesium and its alloys: Mechanism, properties and applications. *J. Magnes. Alloy.* **5**, 74–132 (2017).
 139. Mews, M., Schulze, T. F., Mingirulli, N. & Korte, L. Hydrogen plasma treatments for passivation of amorphous-crystalline silicon-heterojunctions on surfaces promoting epitaxy. *Appl. Phys. Lett.* **102**, (2013).
 140. Park, J. *et al.* High-performance amorphous gallium indium zinc oxide thin-film transistors through N₂O plasma passivation. *Appl. Phys. Lett.* **93**, 2–5 (2008).

141. Xiao, S. Q. *et al.* Chemically active plasmas for surface passivation of Si photovoltaics. *Catal. Today* **252**, 201–210 (2015).
142. Chu, P. K. Progress in direct-current plasma immersion ion implantation and recent applications of plasma immersion ion implantation and deposition. *Surf. Coatings Technol.* **229**, 2–11 (2013).
143. Ouitzau, M., Wolter, M. & Kersten, H. Plasma treatment of polyethylene powder particles in a hollow cathode glow discharge. *Plasma Process. Polym.* **6**, 392–396 (2009).
144. Hinz, A. M., Von Wahl, E., Faupel, F., Strunskus, T. & Kersten, H. Versatile particle collection concept for correlation of particle growth and discharge parameters in dusty plasmas. *J. Phys. D: Appl. Phys.* **48**, (2015).
145. Smets, A. H. M., Kessels, W. M. M. & Van de Sanden, M. C. M. Vacancies and voids in hydrogenated amorphous silicon. *Appl. Phys. Lett.* **82**, 1547–1549 (2003).
146. Groenen, R. *et al.* Surface textured ZnO films for thin film solar cell applications by expanding thermal plasma CVD. *Thin Solid Films* **392**, 226–230 (2001).
147. Von Keudell, A., Meier, M. & Hopf, C. Growth mechanism of amorphous hydrogenated carbon. *Diam. Relat. Mater.* **11**, 969–975 (2002).
148. Annemie, B., Neyts, E., Gijbels, R. & Mullen, J. Van der. Gas Discharge Plasmas and Their Applications, *Spectrochimica Acta Part B* **57**, 609–658 (2002).
149. Neyts, E. C., Ostrikov, K., Sunkara, M. K. & Bogaerts, A. Plasma Catalysis: Synergistic Effects at the Nanoscale. *Chem. Rev.* **115**, 13408–13446 (2015).
150. Bogaerts, A. & Neyts, E. C. Plasma Technology: An Emerging Technology for Energy Storage. *ACS Energy Lett.* **3**, 1013–1027 (2018).

151. Shiratani, M., Maeda, S., Koga, K. & Watanabe, Y. Effects of gas temperature gradient, pulse discharge modulation, and hydrogen dilution on particle growth in silane RF discharges. *Japanese J. Appl. Physics, Part 1 Regul. Pap. Short Notes Rev. Pap.* **39**, 287–293 (2000).
152. Coulombe, S., Léveillé, V., Yonson, S. & Leask, R. L. Miniature atmospheric pressure glow discharge torch (APGD-t) for local biomedical applications. *Pure Appl. Chem.* **78**, 1147–1156 (2006).
153. Chang, J. P. & Coburn, J. W. Plasma–surface interactions. *J. Vac. Sci. Technol. A Vacuum, Surfaces, Film.* **21**, S145–S151 (2003).
154. Von Keudell, A. *et al.* Inactivation of bacteria and biomolecules by low-pressure plasma discharges. *Plasma Process. Polym.* **7**, 327–352 (2010).
155. Halfmann, H., Bibinov, N., Wunderlich, J. & Awakowicz, P. A double inductively coupled plasma for sterilization of medical devices. *J. Phys. D. Appl. Phys.* **40**, 4145–4154 (2007).
156. Jurbergs, D., Rogojina, E., Mangolini, L. & Kortshagen, U. Silicon nanocrystals with ensemble quantum yields exceeding 60%. *Appl. Phys. Lett.* **88**, (2006).
157. Mangolini, L., Thimsen, E. & Kortshagen, U. HIGH-yield plasma synthesis of luminescent silicon quantum dots. *2005 Proc. 4th ASME Conf. Integr. Nanosyst. Des. Synth. Appl.* 73–74 (2005) doi:10.1115/nano2005-87067.
158. Kortshagen, U. R. *et al.* Nonthermal plasma synthesis of nanocrystals: Fundamental principles, materials, and applications. *Chem. Rev.* **116**, 11061–11127 (2016).
159. Shiratani, M. *et al.* Single step method to deposit Si quantum dot films using H₂ + SiH₄ VHF discharges and electron mobility in a Si quantum dot solar cell. *Surf. Coatings Technol.* **201**, 5468–5471 (2007).
160. Hordy, N., Rabilloud, D., Meunier, J. L. & Coulombe, S. High temperature and long-term stability of carbon nanotube nanofluids

- for direct absorption solar thermal collectors. *Sol. Energy* **105**, 82–90 (2014).
161. Meyyappan, M., Delzeit, L., Cassell, A. & Hash, D. Carbon nanotube growth by PECVD: A review. *Plasma Sources Sci. Technol.* **12**, 205–216 (2003).
 162. Meyyappan, M. Plasma nanotechnology: Past, present and future. *J. Phys. D. Appl. Phys.* **44**, (2011).
 163. Montoya, J. H. *et al.* Materials for solar fuels and chemicals. *Nat. Mater.* **16**, 70–81 (2016).
 164. Zhong, Y. *et al.* Transition metal carbides and nitrides in energy storage and conversion. *Adv. Sci.* **3**, (2015).
 165. Figuerola, A., Di Corato, R., Manna, L. & Pellegrino, T. From iron oxide nanoparticles towards advanced iron-based inorganic materials designed for biomedical applications. *Pharmacol. Res.* **62**, 126–143 (2010).
 166. Giménez-Marqués, M., Hidalgo, T., Serre, C. & Horcajada, P. Nanostructured metal-organic frameworks and their bio-related applications. *Coord. Chem. Rev.* **307**, 342–360 (2016).
 167. Zhang, J., Liu, X., Neri, G. & Pinna, N. Nanostructured Materials for Room-Temperature Gas Sensors. *Adv. Mater.* **28**, 795–831 (2016).
 168. Miller, D. R., Akbar, S. A. & Morris, P. A. Nanoscale metal oxide-based heterojunctions for gas sensing: A review. *Sensors Actuators, B Chem.* **204**, 250–272 (2014).
 169. Gupta, A., Sakthivel, T. & Seal, S. Recent development in 2D materials beyond graphene. *Prog. Mater. Sci.* **73**, 44–126 (2015).
 170. Krashennnikov, A. V. & Banhart, F. Engineering of nanostructured carbon materials with electron or ion beams. *Nat. Mater.* **6**, 723–733 (2007).
 171. Tian, J., Zhao, Z., Kumar, A., Boughton, R. I. & Liu, H. Recent progress in design, synthesis, and applications of one-dimensional TiO₂

- nanostructured surface heterostructures: A review. *Chem. Soc. Rev.* **43**, 6920–6937 (2014).
172. Dong, R., Zhang, T. & Feng, X. Interface-Assisted Synthesis of 2D Materials: Trend and Challenges. *Chem. Rev.* **118**, 6189–6325 (2018).
 173. Zhang, Q., Uchaker, E., Candelaria, S. L. & Cao, G. Nanomaterials for energy conversion and storage. *Chem. Soc. Rev.* **42**, 3127–3171 (2013).
 174. Aricò, A. S., Bruce, P., Scrosati, B., Tarascon, J. M. & Van Schalkwijk, W. Nanostructured materials for advanced energy conversion and storage devices. *Nat. Mater.* **4**, 366–377 (2005).
 175. Pikul, J. H., Gang Zhang, H., Cho, J., Braun, P. V. & King, W. P. High-power lithium ion microbatteries from interdigitated three-dimensional bicontinuous nanoporous electrodes. *Nat. Commun.* **4**, 1732–1735 (2013).
 176. Cheng, F., Liang, J., Tao, Z. & Chen, J. Functional materials for rechargeable batteries. *Adv. Mater.* **23**, 1695–1715 (2011).
 177. Stamate, E. & Ohe, K. On the surface condition of Langmuir probes in reactive plasmas. *Appl. Phys. Lett.* **78**, (2001).
 178. Stamate, E. & Ohe, K. Influence of surface condition in Langmuir probe measurements. *J. Vac. Sci. Technol. Part A Vacuum, Surfaces Film.* **20**, (2002).
 179. Fan, Z., Chu, P. K., Chan, C. & Cheung, N. W. Sample stage induced dose and energy nonuniformity in plasma immersion ion implantation of silicon. *Appl. Phys. Lett.* **73**, 202–204 (1998).
 180. Benedikt, J., Kersten, H. & Piel, A. Foundations of measurement of electrons, ions and species fluxes toward surfaces in low-temperature plasmas. *Plasma Sources Sci. Technol.* **30**, (2021).
 181. Demidov, V. I., Ratynskaia, S. V. & Rypdal, K. Electric probes for plasmas: The link between theory and instrument. *Rev. Sci. Instrum.* **73**, 3409 (2002).

182. Godyak, V. A., Piejak, R. B. & Alexandrovich, B. M. Probe diagnostics of non-Maxwellian plasmas. *J. Appl. Phys.* **73**, 3657–3663 (1993).
183. Stamate, E., Popa, G. & Ohe, K. Test function for the determination of plasma parameters by electric probes. *Rev. Sci. Instrum.* **70**, (1999).
184. Bacal, M. Photodetachment diagnostic techniques for measuring negative ion densities and temperatures in plasmas. *Rev. Sci. Instrum.* **71**, 3981–4006 (2000).
185. Fantz, U., Briefi, S., Heiler, A., Wimmer, C. & Wunderlich, D. Negative Hydrogen Ion Sources for Fusion: From Plasma Generation to Beam Properties. *Front. Phys.* **9**, 1–17 (2021).
186. Fantz, U. *et al.* Negative ion RF sources for ITER NBI: Status of the development and recent achievements. *Plasma Phys. Control. Fusion* **49**, (2007).
187. Niu, H. & Houk, R. S. Review Houk ion extraction in ICPMS. *Spectrochim. Acta B* **51**, 37 (2002).
188. Latrasse, L., Sadeghi, N., Lacoste, A., Bès, A. & Pelletier, J. Characterization of high density matrix microwave argon plasmas by laser absorption and electric probe diagnostics. *J. Phys. D. Appl. Phys.* **40**, 5177–5186 (2007).
189. Béchu, S. *et al.* Multi-dipolar plasmas for plasma-based ion implantation and plasma-based ion implantation and deposition. *Surf. Coatings Technol.* **186**, 170–176 (2004).
190. Lacoste, A., Lagarde, T., Béchu, S., Arnal, Y. & Pelletier, J. Multi-dipolar plasmas for uniform processing: Physics, design and performance. *Plasma Sources Sci. Technol.* **11**, 407–412 (2002).
191. E. Stamate, K. I. and K. O. Electron properties in a multipolar magnetic confinement plasma. in *Proceedings of 3rd International Conference on Reactive Plasmas (ICRP), Nara, Japan* 87–88 (1997).
192. Fanchini, G., Ray, S. C., Tagliaferro, A., Tiainen, V. & Sajavaara, T. Effect of isotopic substitution on IR and ESR properties of mass

- selected ion beam deposited ta-C films. **12**, 900–904 (2003).
193. Karahashi, K. & Hamaguchi, S. Ion beam experiments for the study of plasma – surface interactions. (2014) doi:10.1088/0022-3727/47/22/224008.
 194. Gillen, G. & Fahey, A. Secondary ion mass spectrometry using cluster primary ion beams. **204**, 209–213 (2003).
 195. Yoshimura, S., Sugimoto, S., Murai, K. & Kiuchi, M. Surface & Coatings Technology Low-energy mass-selected ion beam production of fragments produced from hexamethyldisiloxane for the formation of silicon oxide film. *Surf. Coat. Technol.* **313**, 402–406 (2017).
 196. Johnson, G. E., Gunaratne, D. & Laskin, J. SOFT- AND REACTIVE LANDING OF IONS ONTO SURFACES : CONCEPTS AND APPLICATIONS. 439–479 (2016) doi:10.1002/mas.
 197. You, A., Be, M. A. Y. & In, I. A new high transmission infinite range mass selector for cluster and nanoparticle beams. **4497**, (2005).
 198. Mensing, M., Schumacher, P., Gerlach, J. W., Herath, S. & Lotnyk, A. Applied Surface Science Influence of nitrogen ion species on mass-selected low energy ion-assisted growth of epitaxial GaN thin films. *Appl. Surf. Sci.* **498**, 143830 (2019).
 199. Alami, J. *et al.* High-power impulse magnetron sputtering of Ti-Si-C thin films from a Ti₃SiC₂ compound target. *Thin Solid Films* **515**, 1731–1736 (2006).
 200. Wang, Z., Nayak, P. K., Caraveo-Frescas, J. A. & Alshareef, H. N. Recent Developments in p-Type Oxide Semiconductor Materials and Devices. *Adv. Mater.* **28**, 3831–3892 (2016).
 201. Kamiya, T., Nomura, K. & Hosono, H. Present status of amorphous In-Ga-Zn-O thin-film transistors. *Sci. Technol. Adv. Mater.* **11**, (2010).
 202. Ha, S. D. *et al.* Transition metal oxides for organic electronics: Energetics, device physics and applications. *Adv. Mater.* **24**, 402–411 (2019).

203. Jenifer, K., Arulkumar, S., Parthiban, S. & Kwon, J. Y. A Review on the Recent Advancements in Tin Oxide-Based Thin-Film Transistors for Large-Area Electronics. *J. Electron. Mater.* **49**, 7098–7111 (2020).
204. Tsao, J. Y. *et al.* Ultrawide-Bandgap Semiconductors: Research Opportunities and Challenges. *Adv. Electron. Mater.* **4**, 1600501 (2018).
205. Troughton, J. & Atkinson, D. Amorphous InGaZnO and metal oxide semiconductor devices: An overview and current status. *J. Mater. Chem. C* **7**, 12388–12414 (2019).
206. Meyer, J. *et al.* Transition metal oxides for organic electronics: Energetics, device physics and applications. *Adv. Mater.* **24**, 5408–5427 (2012).
207. Yu, X., Marks, T. J. & Facchetti, A. Metal oxides for optoelectronic applications. *Nat. Mater.* **15**, 383–396 (2016).
208. Arafat, M. M., Dinan, B., Akbar, S. A. & Haseeb, A. S. M. A. Gas sensors based on one dimensional nanostructured metal-oxides: A review. *Sensors (Switzerland)* **12**, 7207–7258 (2012).
209. Ha, S. D. & Ramanathan, S. Adaptive oxide electronics: A review. *J. Appl. Phys.* **110**, (2011).
210. Ellmer, K. Past achievements and future challenges in the development of optically transparent electrodes. *Nat. Photonics* **6**, 809–817 (2012).
211. Ishijima, T., Goto, K., Ohshima, N., Kinoshita, K. & Toyoda, H. Spatial Variation of Negative Oxygen Ion Energy Distribution in RF Magnetron Plasma with Oxide Target. *Jpn. J. Appl. Phys.* **48**, 116004 (2009).
212. Pokorný, P. *et al.* Investigation of the negative ions in Ar/O₂ plasma of magnetron sputtering discharge with Al:Zn target by ion mass spectrometry. *Plasma Process. Polym.* **8**, 459–464 (2011).
213. Dodd, R., You, S. D., Bryant, P. M. & Bradley, J. W. Negative ion density measurements in a reactive dc magnetron using the eclipse

- photodetachment method. *Plasma Sources Sci. Technol.* **19**, (2010).
214. Ellmer, K. Resistivity of polycrystalline zinc oxide films: Current status and physical limit. *J. Phys. D. Appl. Phys.* **34**, 3097–3108 (2001).
 215. Minami, T. Transparent conducting oxide semiconductors for transparent electrodes. *Semicond. Sci. Technol.* **20**, (2005).
 216. Cebulla, R., Wendt, R. & Ellmer, K. Al-doped zinc oxide films deposited by simultaneous rf and dc excitation of a magnetron plasma: Relationships between plasma parameters and structural and electrical film properties. *J. Appl. Phys.* **83**, 1087–1095 (1998).
 217. Bikowski, A., Welzel, T. & Ellmer, K. The correlation between the radial distribution of high-energetic ions and the structural as well as electrical properties of magnetron sputtered ZnO:Al films. *J. Appl. Phys.* **114**, (2013).
 218. Bikowski, A., Welzel, T. & Ellmer, K. The impact of negative oxygen ion bombardment on electronic and structural properties of magnetron sputtered ZnO:Al films. *Appl. Phys. Lett.* **102**, 10–14 (2013).
 219. Bornholdt, S. *et al.* The method of conventional calorimetric probes - A short review and application for the characterization of nanocluster sources. *Surf. Coatings Technol.* **205**, S388–S392 (2011).
 220. Stamate, E., Sugai, H. & Ohe, K. Principle and application of a thermal probe to reactive plasmas. *Appl. Phys. Lett.* **80**, (2002).
 221. Wen, L., Sahu, B. B., Kim, H. R. & Han, J. G. Study on the electrical, optical, structural, and morphological properties of highly transparent and conductive AZO thin films prepared near room temperature. *Appl. Surf. Sci.* **473**, 649–656 (2019).
 222. Dondapati, H., Santiago, K. & Pradhan, A. K. Influence of growth temperature on electrical, optical, and plasmonic properties of aluminum:zinc oxide films grown by radio frequency magnetron sputtering. *J. Appl. Phys.* **114**, (2013).

223. Lung, C., Toma, M., Pop, M., Marconi, D. & Pop, A. Characterization of the structural and optical properties of ZnO thin films doped with Ga, Al and (Al+Ga). *J. Alloys Compd.* **725**, 1238–1243 (2017).
224. Miao, D., Jiang, S., Zhao, H., Shang, S. & Chen, Z. Characterization of AZO and Ag based films prepared by RF magnetron sputtering. *J. Alloys Compd.* **616**, 26–31 (2014).
225. Li, H. *et al.* Zinc oxide as a model transparent conducting oxide: A theoretical and experimental study of the impact of hydroxylation, vacancies, interstitials, and extrinsic doping on the electronic properties of the Polar ZnO (0002) surface. *Chem. Mater.* **24**, 3044–3055 (2012).
226. Charpentier, C., Prod'Homme, P. & Roca I Cabarrocas, P. Microstructural, optical and electrical properties of annealed ZnO:Al thin films. *Thin Solid Films* **531**, 424–429 (2013).
227. Kumar, M., Wen, L., Sahu, B. B. & Han, J. G. Simultaneous enhancement of carrier mobility and concentration via tailoring of Al-chemical states in Al-ZnO thin films. *Appl. Phys. Lett.* **106**, 1–6 (2015).
228. Matsunami, N. *et al.* Energy dependence of the ion-induced sputtering yields of monatomic solids. *At. Data Nucl. Data Tables* **31**, 1–80 (1984).

This dissertation is a synopsis of 19 research publications co-authored by Eugen Stamate on phenomenology and applications of 3D plasma-sheath-lenses. It is demonstrated that the sheath surrounding electrodes interfacing with insulators acts as an electrostatic lens, focusing positive or negative charges to distinct locations on the electrode surface depending on the entrance coordinates at the sheath edge. Two ion focusing effects have been discovered. The discrete focusing leads to the formation of a passive surface, while the modal focusing results in the formation of certain 'modal spots' and/or 'modal lines'. The very well-defined patterns revealed by the focusing effects open new possibilities in plasma and sheath diagnostics, directly correlating with ion-induced surface modifications. By customizing 3D plasma-sheath-lenses one can manipulate ion kinetics to induce desired ion optics, which, in combination with magnetic fields, provides significant flexibility for various applications, including focused ion beam extraction, mass spectrometry, plasma immersion ion implantation, and new sensors for negative ions. In the last chapter, the pioneering concept of 3D plasma-sheath-lenses is further extended to negative ion focusing during magnetron sputtering. New developments are anticipated to improve the correlation between simulations and experiments, encompassing time-dependent processes or other intricate details.

DTU Nanolab
National Centre for Nano Fabrication and Characterization

Ørsted's Plads
Building 347
DK-2800 Kongens Lyngby

www.nanolab.dtu.dk

ISBN 978-87-975214-0-3